Łukasiewicz
Poznański
Instytut
Technologiczny

RAIL VEHICLES
POJAZDY SZYNOWE

1–2/2022

e-ISSN: 2719-9630
ISSN: 0138-0370

Łukasiewicz
Poznań
Institute of
Technology

Rail Vehicles/Pojazdy Szynowe

www.railvehicles.eu

A Scientific Journal
No. 1-2, 2022

ISSN 0138-0370
eISSN 2719-9630

Publisher

Łukasiewicz Research Network
– Poznań Institute of Technology
ul. Ewerysta Estkowskiego 6
61-755 Poznań
e-mail: office@pit.lukasiewicz.gov.pl

Editorial

Rail Vehicles/Pojazdy Szynowe
Łukasiewicz Research Network
– Poznań Institute of Technology
ul. Ewerysta Estkowskiego 6
61-755 Poznań
phone +48 693 091 240
e-mail: redakcja.dbt@pit.lukasiewicz.gov.pl

Rail Vehicles/Pojazdy Szynowe

The scientific quarterly journal dedicated to problems of designing, construction and researches of rail stock

Contents

Declaration of the original version

The original version of the *Rail Vehicles/ Pojazdy Szynowe* journal is the printed version.

Rail Vehicles/Pojazdy Szynowe quarterly is covered by the patronage of the Transport Committee of the Polish Academy of Science

Subscriptions

Send subscription requests to the Publisher's address.

Cost a single issue PLN 34.78.

Typesetting: Marcin Tomkowiak

Circulation: 100 copies

Printing: Wieland Drukarnia Cyfrowa

ul. Ziębicka 17, 60-164 Poznań, Poland

Cover: Marcin Tomkowiak

The journal is registered and listed in the Polish and international database

Article citation info:
Słowiński M. The characteristics of the selected types of wheel wear and their effect on the rail vehicle – track interaction. *Rail Vehicles/Pojazdy Szynowe*. 2022, 1-2, 3-9. https://doi.org/10.53502/RAIL-147440

Rail Vehicles/Pojazdy Szynowe

www.railvehicles.eu

The characteristics of the selected types of wheel wear and their effect on the rail vehicle – track interaction

Marcin **Słowiński** [a, *]

[a] *Poznan University of Technology, Institute of Transport, Poznan, Poland*

ARTICLE INFO

Received: 23 January 2022
Revised: 14 March 2022
Accepted: 17 March 2022
Available online: 21 March 2022

KEYWORDS

wear
rail vehicle wheel
polygonisation
wheel flat
shelling

The aim of this paper is to present the selected types of rail wheel wear and their influence on vehicle-track interaction. The first part discusses the wheel-rail interface and presents the essential information about the wear of rail vehicle wheels. Differences in the nature of the wear of rail and tram wheels are pointed out. Then, characteristics of typical forms of wheel wear are presented, together with the description of the mechanisms of their occurrence and the existing technical measures leading to their reduction. In the last part of the text, the impact of the previously described forms of wheel wear on the vehicle-track interaction is discussed.

1. Introduction

Wear is a significant problem in the operation of rail vehicle wheels. While the wear process itself in friction pairs, of which the wheel-rail contact is an example, is inevitable, the attempts made to reduce it or to eliminate its serious forms are the key issues concerning the improvement of the rail transport system operation. Reducing the rate of wheel wear processes or preventing critical defects is possible by identifying the causes of their occurrence and at least minimizing them. This leads to an extension of the service life of the rolling stock and the infrastructure, providing a measurable improvement in the functioning of the rail transport system. For the operators of these systems, this results in benefits connected with improved driving comfort, traffic safety and finally, reduced financial costs. Because of the technical progress made in the construction of rail vehicles, higher dynamic loads are acting on the vehicles and the track. For this reason, limiting wheel wear is undoubtedly an important engineering challenge that determines the correct operation of the rolling stock and the infrastructure.

The process of wheel wear in rail vehicles is a function of many factors such as the dynamics of the rail vehicle or the mechanics of the wheel-rail contact, creating a research problem of many origins. Therefore, the division of types of wheel wear is not always unequivocal, whereas, in the present study, wheel wear types were divided into three basic groups: wheel wear occurring in the transverse direction of the wheel rolling surface, resulting in a change of wheel profile (its evolution), deviations of the rolling circle shape from the ideal wheel (out-of-roundness defects) and rolling contact fatigue wear by shelling and spalling. Wheel wear, which is the subject of this study, has a negative impact in the vast majority of cases, both on vehicle dynamics and on the technical condition of rolling stock and infrastructure. Due to its consequences, which affect the functioning of the rail transport system, it is important to distinguish between these types of wear, to understand the mechanisms of these defects, and to develop technical measures to prevent intensified wear of rolling stock and infrastructure.

* Corresponding author: marcin.slowinski@put.poznan.pl (M. Slowinski)

2. The wear of rail vehicle wheels

The wheel-rail interface is an important area because it affects the dynamic behavior of the vehicle, the emission of sound, vibrations, and finally the wear. This means that the level of wheel wear both influences and is influenced by the phenomena occurring at the wheel-rail interface. Assuming that the radius of the wheel and the curvature of the rail head are constant at the point of contact, the contact patch has an elliptical shape and has an area not exceeding 1 cm^2. For this reason, large values of the contact stresses occur at the wheel-rail interface, often as high as 1500 MPa.

Three main types of contact can occur between wheel and rail. Wheel-rail contact at a single point (area) provides relatively better vehicle dynamic characteristics than other types of contact, such as self-steering ability and reduction of rolling resistance between wheel and rail. Due to the small contact area, high values of the contact stresses occur and create conditions for escalate wheel and rail wear. Multipoint contact (usually in the form of a two-point contact) takes place when apart from the nominal contact point, there are additional contact areas, e.g. between the flange root and the rail gauge corner, for instance in case of curving. Multipoint contact is undesirable because the contact points are located on non-identical rolling radii of the wheel, which causes different rolling speeds. This results in creepages, which intensify wheel and rail wear and lead to increased noise emission [10]. Conformal contact appears when the wheel or rail is worn so that their contact patch is spread over a large area due to the similarity of their geometries. It limits the wear of the wheel and rail, however, it worsens the dynamic properties of the vehicle, such as lowering the critical speed or increasing the frequency of hunting motion.

The characteristic of wheel-rail interaction create the conditions for wear mechanisms, of which three basic ones can be listed [2]:

1. Rolling Contact Fatigue (RCF) – this type of wear mechanism can be characterized as fatigue wear caused by cyclic contact stresses of variable values at the wheel-rail interface. It can occur on or underneath the wheel running surface and has the character of spalling or shelling wear [7].
2. Adhesive wear – it is related to the roughness of the wheel and the rail. The roughness vertices of the wheel and rail surfaces stick together and, due to the relative velocity, they are plastically deformed or sheared.
3. Abrasive wear – it is caused by a third party between the wheel and the rail or by the wheel and rail surfaces rubbing against each other resulting in subsequent localized material loss. In the wheel-rail system, abrasive wear is very often created by grains of sand used to increase friction between the wheel and the rail (distributed by sandbox) and metallic wear products which are emitted from the brake system.

There are also fundamental differences between wheel wear of tram vehicles and wheel wear of rail vehicles. The most important of them are those which are the outcome of the differences in the construction of those vehicles. The narrower flange width of tram wheels causes more frequent contact with the side of the rail head, whereas the smaller diameter of the wheel results in a smaller contact area and thus higher stress in that area. It also affects in an increased number of rolling cycles. In addition, the presence of small radius curves in tram tracks (the minimum radius of a curve in the tram network is 18 m) gives a rise in a more intense and more frequent generation of creepages between the tram wheel and the rail.

3. The evolution of the wheel profile

As a result of wheel-rail contact accompanied by normal or tangential forces, abrasive and adhesive wear of the wheel profile and the rail occur. For this reason, the original (nominal) contour of the wheel rolling profile is lost. A comparison of the nominal and worn PST profiles is presented in Fig. 1.

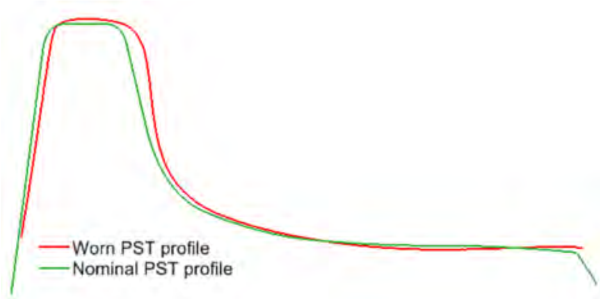

Fig. 1. The comparison of nominal and worn PST wheel profiles

The most important and the most frequent changes in the wheel profile are those related to the flange, namely reduction of its inclination, as well as changes in the width and geometry of the flange root. Additionally, the height of the flange increases as an outcome of the wear of the rolling surface [1]. In tram vehicles, a decrease in the flange width of leading wheelsets is observed, whereas in the case of trailing wheelsets its increase is a frequent phenomenon because of the smaller values of acting forces. Another important phenomenon that originated from the evolution of the wheel profile is hollow wear, which is caused by uneven material wear in the central area of the rolling surface [9]. This gives rise to the increase of the value of the equivalent conicity, which describes the ratio of the difference of the inner and outer wheel radii related to the lateral displacement of the wheelset. As the wheel wears (and thus its conformality increases), the value of this parameter rises due to non-uniform wheel wear, resulting in a difference in length of the rolling radii on the inner and outer wheels.

The change in the shape of the rolling profile is inevitable, but there are technical measures to minimize it. The most important is to ensure that the shape of the rolling profile is optimal with regard to the intensity of wear, so as to eliminate as far as possible creepages or to reduce impact loads and the values of the contact stresses at the wheel-rail interface. Another technical measure is the flange or rail lubrication, which is used for counteracting abrasive and adhesive wear. Rail or wheel lubrication is very often used on tight curves to reduce creepages intensity (and consequently squealing noise). A routine method of restoring the original rolling contour of a wheel is reprofiling, which is applied at specified intervals. The amount of reprofiling is limited by the material range allocated for it. For example, the nominal wheel diameter of the Tramino S105p tram is 610 mm and the minimum is 520 mm.

4. OOR defects

4.1. Polygonisation

Polygonisation of wheels is manifested by deviations of radius length occurring on the circumference of the wheel, which can be described as the loss of round shape by the wheel and its transformation into a polygon. This form of wear is seen in every segment of rail vehicles and, of all the OOR-type defects, it is considered to be the one that most adversely affects vehicle-track interaction [8, 12]. Figure 2 shows typical forms of polygonisation – eccentricity, ovality, and trigonality. Under operational conditions, several different forms of polygonisation may coexist [6].

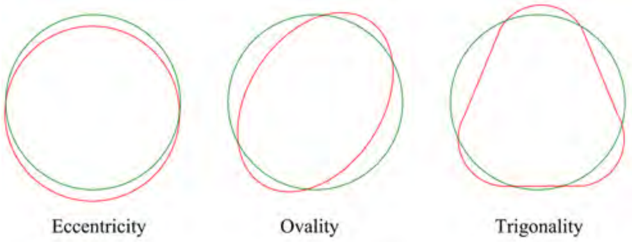

Fig. 2. The typical forms of polygonisation

The effect of wheel polygonisation is the induction of impact loads at the wheel-rail interface, which has a negative effect on the dynamics of the rail vehicle and increases the wear of vehicle and track components. Although the mechanisms of polygonisation are very complex and depend on many variables, based on the information presented in the literature, the following causes of polygonisation can be listed [8, 12]:

- impact loads on the wheelset (unsprung mass),
- resonant frequencies acting on the wheel, which may originate e.g. from track or vehicle excitations,
- stick-slip phenomena between wheel and rail,
- the elasticity of the wheelset and track,
- the action of pad brakes,
- wheel flats,
- dimensional and shape inaccuracies of the support rollers of the lathe,
- stress formation during reprofiling of a wheel by a rotary lathe,
- instability of the wheelset.

As a way of preventing polygonisation, more frequent wheel reprofiling is suggested, which would remove non-heterogenic microstructure from the surface and thus inhibit the initiation of this type of wear. Another method to reduce this type of wear is to minimise the unsprung mass of the wheelset. This is achieved by reducing the mass of the axle, e.g. by hollowing it out, while disc shapes optimised for this purpose are used to reduce the mass of the wheel. Another way to reduce polygonisation can be to check the dimensional and shape accuracy of the support rollers of sub-track lathes more frequently [11].

4.2. Wheel flat

According to [15], a wheel flat can be defined as a local abrasion occurring on the wheel rolling surface, causing the loss of its original contour (Fig. 3). Wheel flat occurs as a result of sliding between the wheel and the rail, which is most often generated by wheel locking during braking due to poor technical conditions of the brake or improperly selected braking force. Other factors that contribute to wheel-rail slip are third-party bodies between the wheel and the rail (e.g. leaves, snow) or contamination of the rail surface. Fig. 4 shows a wheel flat on the wheel running surface.

Fig. 3. Wheel flat [16]

The formation of the wheel flat is related to abrasive wear and a martensitic transformation of the wheel rolling surface material. In this case, the mechanism of the wheel flat formation can be described in the following points [6]:

1. The occurrence of full slip between the wheel and the rail which is caused by an inappropriate braking process.
2. Local temperature rise at the wheel-rail interface because of the frictional energy dissipation.
3. Rapid cooling of the wheel running surface due to rotation of the wheel and conduction of heat into the wheel.
4. Generation of residual stresses and the formation of brittle and hard martensite on the wheel running surface.
5. Development of a flat spot as a consequence of cyclic contact stresses leading to abrasion of the martensitic layer.

After the formation of the martensitic layer and the resulting wheel flat, stresses due to rolling loads build up deep into the material. It is reported that, in an extreme case, a wheel flat 40–60 mm long and 1 mm deep can evolve into an area up to 500 mm long and 5 mm deep [6].

Avoiding sudden braking, removing the martensitic layer from the rolling surface or regular detection of wheel impact loads are proposed as effective ways to prevent the initiation of wheel flat. It is worth noting that due to the specific nature of tram lines, frequent and often sudden braking takes place. On this account, tram vehicle wheels are strongly exposed to the formation of wheel flat [9]. Importantly, the contact of the brake pad with the wheel rolling surface, as in the case of a pad brake, reduces the formation of the wheel flat by cyclic abrasion of the surface layer of the rolling surface. As a result, the wheel regains its round shape.

4.3. Scaled wheels

The scaled wheels phenomenon can be defined as sticking of the fragments of material to the wheel rolling surface. The first mechanism of its formation mentioned in the literature is related to sliding between the wheel and the rail, due to the complete wheel blocking during sudden braking [4]. In such a case, by the increase in the wheel temperature, the material becomes more plastic and is detached from one region of the rolling surface. After that, it sticks to another fragment of this surface. The result is an area with adhered material (Fig. 4).

Usually, during the scaled wheels formation, the plasticised wheel material is mixed with contaminants from the track or the brake system. The mechanism involves both a wheel flat and a scaled wheel generation – respectively a wheel flat is formed on the wheel, which releases material to the rail, and a scaled wheel is formed on the wheel, to which the material adheres.

Fig. 4. Scaled wheels [17]

The second mechanism of scaled wheels creation is connected with wheels that interact with pad brakes [6]. The essence of this type of wear is the loss of the original wheel outline due to metal filings from the brake system pressing into the material of the rolling surface. During braking, when a brake pad contacts with the tread, hot spots occur. Their plasticity leads to the sticking of small particles coming out of brake pads.

Important ways to prevent this type of wear are to avoid sudden wheel-rail slippage by, among other things, suitable braking processes and to limit the formation of material particles which are emitted from the braking system. It can be achieved by replacing classic cast-iron brake pads with composite brake pads [6].

5. RCF wear

5.1. Shelling

Wheel wear by shelling is manifested by the loss of a piece of material of the wheel tread [3]. Two basic types of this form of wear can be distinguished, which differ in the formation mechanism – shelling caused by fatigue of the rolling surface material and shelling generated by a slip between the wheel and the rail [14]. This type of wear is illustrated in Fig. 5.

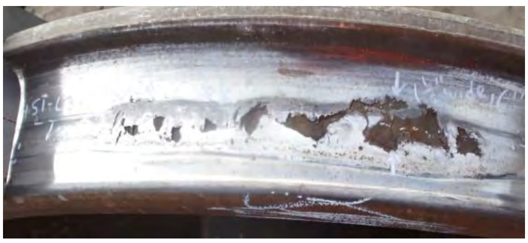

Fig. 5. Shelling wear [18]

Shelling, caused by material fatigue, occurs as an outcome of plastic deformation originated from the cyclic contact stresses at the wheel-rail contact. When the yield point of the material is exceeded, fatigue cracks appear. Because of the continuous contact stresses, the cracks grow and merge with each other, resulting in either a cumulative crack or shelling of the wheel rolling surface material [5, 14].

Shelling originated from wheel sliding, unlike spalling wear, is generated by heating the entire surface layer of the wheel rolling surface above 300°C for an extended period of time. Due to the prolonged thermal effect, the surface layer of the tread is weakened and more susceptible to thermal cracks. The presence of contaminants such as sand or water between the wheel and the rail can promote the propagation of cracks deep into the cross-section of the surface layer [7].

In order to limit shelling wear, it is proposed to exploit conformal wheel and rail profiles, more frequent reprofiling, or to use steel with fewer impurities as a wheel construction material [3].

5.2. Spalling

The essence of spalling wear is the loss of material particles from the component. Spalling wear on the wheel rolling surface is shown in Fig. 6. The specific feature of spalling wear and the main difference from shelling wear is the martensitic transformation, which occurs on the wheel rolling surface [13]. In the case of rail vehicle wheels, the mechanism of spalling wear formation can be presented in the following two stages:

1. A local temperature rise in the surface layer of the wheel rolling surface due to the dissipation of frictional energy and, as a consequence, the formation of martensite.
2. Spalling of shallow martensite scales as an outcome of cyclic contact of the rolling wheel with the rail.

Fig. 6. Spalling wear [19]

It is pointed out that the spalling phenomenon, especially in the case of tram vehicle wheels, does not lead to abrupt wear of wheel rolling surfaces due to its surface character, because as a result of the frequent wheelset reprofiling, it is possible to inhibit this type of wear [7]. Apart from reprofiling, a way to eliminate the spalling phenomenon is to control the technical condition of the brake in order to prevent wheel blocking during braking [3].

6. The influence of wheel wear on vehicle-track interaction

The wheel-rail interface is an area in which occur phenomena that determine the exploitation of the vehicle and the infrastructure. For this reason, any form of wheel or rail wear will cause a change in the nature of the interaction between those two elements. This change may not always be negative, for example, the wheel-rail conformation, because, unlike single point contact, the contact stresses between wheel and rail have lower values. However, in most cases, wheel wear has a negative effect on both the vehicle and the infrastructure. Table 1 summarises the types of wheel wear and their impact on the track and the vehicle.

Of the consequences of wheel wear listed in Table 1, three basic changes in the interaction between vehicle and track can be singled out:

1. Impact loads at the wheel-rail interface – a common feature of wheel defects concerning the loss of round shape is the generation of forced periodic vertical vibrations at the wheel-rail interface. In particular, polygonisation of the wheels results in an increased level of vibration emission, both negatively affecting the passengers or loads and also spreading to the environment, e.g. the ground.
2. Increased noise emission – wear and defects in the wheels increase the rolling noise. Rough surfaces and their contact cause oscillations in the vertical direction of the wheel and the resulting noise. Impact noise is a special case of rolling noise, which is not only emitted during normal operation, e.g. when running over rail joints, but also as an outcome of defects in the OOR wheels.
3. Change in vehicle dynamic behavior – the evolution of the wheel rolling profile, e.g. as a result of hollow wear or change in flange root geometry, causes a deterioration of the vehicle dynamic behavior and consequently in an increased level of loads acting on the rails, mainly in the direction transverse to the track axis. An increase in the hunting motion frequency, caused by wear on the wheel rolling surface, leads to longitudinal track irregularities. OOR defects also worsen the dynamic of the vehicle in the track due to the loss of wheel conicity and also increase the susceptibility to derailment through wheel underload. Positive changes in the dynamic behavior of the vehicle are contributed to by, for instance, a reduction in flange width, which reduces the susceptibility to the de-

Table 1. Types of wheel wear and their effect on the track and the vehicle

Wear type		**Impact on the track**	**Impact on the vehicle**
The evolution of wheel profile	Reduction of the inclination of the flange	Contact of the flange with the side of the rail head, increased impact loads	Increased susceptibility to derailment
	Reduction of the width of the flange	Increase in contact stresses values between flange tip and the groove of the crossing (tram vehicles)	Increase of the lateral displacement of the wheelset, reduced susceptibility to derailment
	Change of the geometry of the flange root	Increased impact loads, multipoint contact with the wheel	Increase of the displacement lateral displacement of the wheelset, reduced susceptibility to derailment
	The increase of equivalent conicity value	Increase in impact loads	Reducing the critical speed, increase in the frequency of the hunting motion
OOR defects	Polygonisation	Increased risk of rail and sleeper fracture, creation of vibrations in the track, increased rail roughness	Deterioration of dynamic vehicle behaviour, intensified loading of wheelset axles and bearings, fatigue wear of wheels, bending of wheelset axles, emission of rolling and impact noise, increased susceptibility to derailment
	Wheel flat		
	Scaled wheels		
RCF wear	Shelling	Dynamic overloading which can lead to fracture, increase in rail roughness	Vibration reducing driving comfort, the possibility of wheel breakage
	Spalling	Increase in rail roughness	Vibration reducing driving comfort

derailment, or an increase in wheel-rail conformation, which results in a reduction in the contact stress acting at the wheel-rail interface.

7. Summary

In the article, the characteristics of typical forms of wheel wear and their influence on the interaction between the vehicle and the track were presented. When analysing the origins of the forms of wear of railway vehicle wheels, one can notice a certain relation that the vast majority of defects are caused by the creepages between the wheel and the rail, both those resulting from the processes of braking and kinematic guidance in the track. It confirms the theoretical assumption that, in order to ensure the best possible interaction between the vehicle and the track, the contact between the wheel and the rail should be as rolling as possible. This implies the need for design solutions in the construction of rolling stock that minimize the occurrence of creepages, such as new, optimised rolling profiles or springing characteristics, which enable passing tight curves in positions as close to radial as possible. When considering the design challenges from the infrastructure side to minimise wheel wear, for instance, rail lubrication is suggested. Preventive measures for RCF wear could be more frequent wheel reprofiling, while OOR defects could be limited by reducing impact loads at the wheel-rail contact.

An important conclusion is that wheel and rail wear is strongly related to the nature of the wheel-rail interaction. The wear of this friction pair both determines the quality of wheel-rail contact and is strongly dependent on it. In addition, it should be noted that different forms of wear are dependent on each other – wheel flat may cause polygonisation, while the mechanism of wheel flat generation may be related to scaled wheels formation. An important observation is that not all forms of wheel wear have a negative impact on the vehicle and the track. For example, the evolution of the wheel profile, which manifests itself, among other things, in the reduction of the flange width, reduces the susceptibility to vehicle derailment, while the conformality of the wheel and the rail decreases the contact stresses values at the interface between these two elements.

Nomenclature

OOR out-of-roundeness

RCF rolling contact fatigue

Bibliography

[1] Andersson E., Berg M., Stichel S. Rail vehicle dynamics. *Railway Group KTH*. Stockholm 2014.

[2] Braghin F., Bruni S., Lewis R. Railway wheel wear. *Wheel-Rail Interface Handbook*. Woodhead Publishing 2009.

[3] Kwaśnikowski J., Małdziński L., Borowski J. et al. Analiza przyczyn przyspieszonego zużycia powierzchni tocznych kół autobusu szynowego SA 108 (215M). *Pojazdy Szynowe*. 2007, 2, 1-13. https://doi.org/10.53502/RAIL-139844

[4] Lesiak S. Symulacyjne badania oddziaływania nalepów kół wagonowych na tor. *Logistyka-Nauka*. 2015, 4, 4437-4444.

[5] Magel E., Kalousek J. Identifying and interpreting railway wheel defects. *IHHA Conference: International Heavy Haul Association Conference on Freight Car Trucks/Bogies*. June 1996.

[6] Nielsen J. Out-of-round railway wheels. *Wheel-Rail Interface Handbook*. Woodhead Publishing. 2009, 245-279.

[7] Paczkowska M., Wojciechowski Ł., Kinal G. Analiza efektów zużywania się wybranych obręczy kół tramwajowych w aglomeracji poznańskiej. *Inżynieria Materiałowa*. 2015, 1(6), 41-45. https://doi.org/10.15199/28.2015.6.8

[8] Peng B. Mechanisms of Railway Wheel Polygonisation. *University of Huddersfield*. 2020.

[9] Staśkiewicz T. Kształtowanie profilu koła tramwajowego w aspekcie oddziaływania dynamicznego z szyną/On tram wheel profile design in terms of dynamic interaction with rail (Dissertation). Politechnika Poznańska. Poznan 2020.

[10] Staśkiewicz T., Firlik B. Analysis of wheel/rail interaction for the development of a new tram wheel profile. *Computers in Railways XV: Railway Engineering Design and Operation*. 2016, 162, 431-440. https://doi.org/10.2495/cr160391

[11] Staśkiewicz T., Firlik B., Kominowski J. Out-of-round tram wheels – Multibody simulation study based on measured wheel rim geometry. *Proceedings of the Institution of Mechanical Engineers, Part F: Journal of Rail and Rapid Transit*. 2021, 236(1), 122-133. https://doi.org/10.1177/0954409721994036

[12] Tao G., Wen Z., Jin X. et al. Polygonisation of railway wheels: a critical review. *Railway Engineering Science*. 2020, 28(4), 317-345. https://doi.org/10.1007/s40534-020-00222-x

[13] Wojciechowski, Ł., Gapiński B., Firlik B. et al. Characteristics of tram wheel wear: Focus on mechanism identification and surface topography. *Tribology International*. 2020, 150, 106365. https://doi.org/10.1016/j.triboint.2020.106365

[14] Zhang G., Ren R. Study on typical failure forms and causes of high-speed railway wheels. *Engineering Failure Analysis*. 2019, 105, 1287-1295. https://doi.org/10.1016/j.engfailanal.2019.07.063

[15] Instrukcja pomiarów i oceny technicznej zestawów kołowych pojazdów trakcyjnych Bt-11. PKP Intercity, 2010.

[16] Wikimedia Commons. https://commons.wikimedia.org/wiki/File:Flachstelle.JPG (accessed on 01.22.2022)

[17] ESR 0330. Wheel defect manual. Transport RailCorp. 2010.

[18] Effects of Temperature on Wheel Shelling, FRA. https://railroads.dot.gov/rolling-stock/current-projects/effects-temperature-wheel-shelling (accessed on 01.22.2022).

[19] WCM, Wheel Condition Monitor. https://www.trackiq.net/WCM.html (accessed on 01. 22.2022).

Article citation info:
Pielecha I., Engelmann D., Czerwinski J. et al. Use of hydrogen fuel in drive systems of rail vehicles. *Rail Vehicles/Pojazdy Szynowe*. 2022, 1-2, 10-19. https://doi.org/10.53502/RAIL-147725

Rail Vehicles/Pojazdy Szynowe

www.railvehicles.eu

Use of hydrogen fuel in drive systems of rail vehicles

Ireneusz **Pielecha** [a, *], Danilo **Engelmann** [b], Jan **Czerwinski** [c], Jerzy **Merkisz** [a]

[a] *Faculty of Civil and Transport Engineering, Poznan University of Technology, Poznan, Poland*
[b] *Laboratory for IC-Engines and Exhaust Emission Control, University of Applied Sciences, Switzerland*
[c] *CJ Consulting (CJC), Switzerland*

ARTICLE INFO

Received: 21 February 2022
Revised: 21 March 2022
Accepted: 26 March 2022
Available online: 27 March 2022

KEYWORDS

Hydrogen
Hydrogen properties
Hydrogen storage
Hydrogen powered combustion engines

The search for substitutes for modern fossil fuels incentivises the use of new propulsion systems (hybrid or electric) and the use of new fuels (gaseous, mainly hydrogen). The article discusses the basic issues related to hydrogen fuel: from its extraction, through the discussion of its properties to its use and applications. Analyzes of the energy consumption involved in its extraction or production were presented, classifying hydrogen in those terms. Great emphasis was placed on design solutions for the use of hydrogen in internal combustion engines, together with discussing the concept of its combustion. The methods of storing hydrogen in a condensed and compressed form were also presented, indicating at the same time the most modern solutions available, such as mixed systems – storage in cryo-compressed form. It has been shown that the combustion of hydrogen in internal combustion engines increases their efficiency, and at the same time significantly reduces the exhaust emissions of toxic gases – including the emission of nitrogen oxides.

1. Introduction

The increasing need to reduce the consumption of fossil fuels drives the search for alternative energy sources for transport means. Currently alternative fuels can be divided into different types, one of which being gaseous fuels, which due to their properties can be used in new combustion systems (such as Turbulent Jet Ignition (TJI) [6, 25], homogeneous charge compression ignition (HCCI) [34] and reactivity controlled compression ignition (RCCI) [36]). Among these fuels, methane, which is a component of natural gas, is currently the most widely used. Its use in conventional combustion engines is quite common (in heavy-duty vehicles), especially due to its storage options. Storing natural gas in compressed form is a technology that is already widely developed and established. Despite the high compression pressure (up to 20 MPa) [11], such fuel is injected into the intake manifold at a pressure of up to 0.9 MPa. The storage of natural gas in liquefied form (LNG, temperature –162°C, pressure approx. 100 kPa) is much less popular [37]. Despite the fact that its energy potential is greater, the technology being too expensive has resulted in it not gaining the necessary interest in the market so far to reach widespread use.

Currently, a much more environmentally advantageous solution is to supply internal combustion engines with hydrogen, with the combustion products being mainly water vapor and nitrogen oxides as a result [31]. Trace amounts of other exhaust components, which are the products of combustion of engine oil, can also be observed in these solutions [27, 38]. Nevertheless, such engines can meet stringent exhaust emission norms.

Another future-proof solution for powering means of transport (including rail transport) is the use of electric drives. The rapid development of lithium-ion batteries (including for rail vehicles) [23, 32] and the announcements of the promises of solid-state batteries production [24, 26] resulted in continued interest in such energy sources.

A comparative analysis of the energy storage costs was shown in Fig. 1. The energy potential of hydro-

* Corresponding author: ireneusz.pielecha@put.poznan.pl (I. Pielecha)

gen, as well as conventional fuels, is still significantly greater than that offered by batteries. In 2020, these costs in the case of hydrogen were over 20 times lower (in €/kWh) than in the case of Li-Ion batteries. A further reduction in these costs is expected in the coming years (much faster in the case of hydrogen than batteries). This may result in these costs reaching about 30 times the share of the existing costs by 2025, with a much greater advantage for hydrogen than before. Along with the reduction of hydrogen storage costs, one can expect an increase in the energy density of hydrogen (in kWh/kg) at a pressure of 35 MPa (currently hydrogen is stored at a pressure of 70 MPa). This energy density is about 20 times lower for Li-Ion batteries. Hence it is possible that hydrogen may become more advantageous alternative as a fuel to electric drives in vehicles.

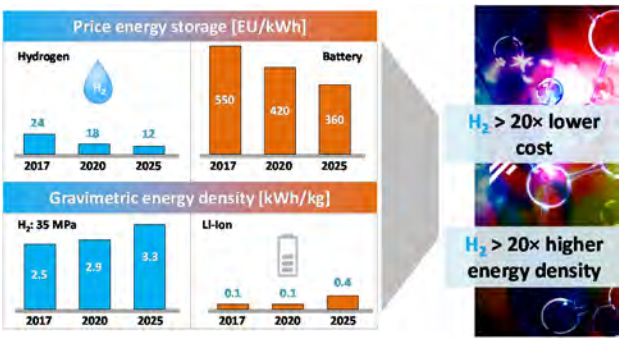

Fig. 1. Energy density of hydrogen and Li-Ion batteries [35]

The analysis of modern vehicle drives efficiency has shown, however, that the efficiency of the electric drive (over 90%) is more than twice as high as that of the combustion engine (over 40%). If the over 20 times greater value of the mass energy density is also taken into account, the result is an approximately 10-fold increase in the effective range for a hydrogen-powered vehicle (Fig. 2). Such considerations lead to the conclusion that hydrogen, being a clean and ecological fuel, can be a direct alternative as a viable choice in fuel supply for combustion engines as well as fuel cells in modern vehicles.

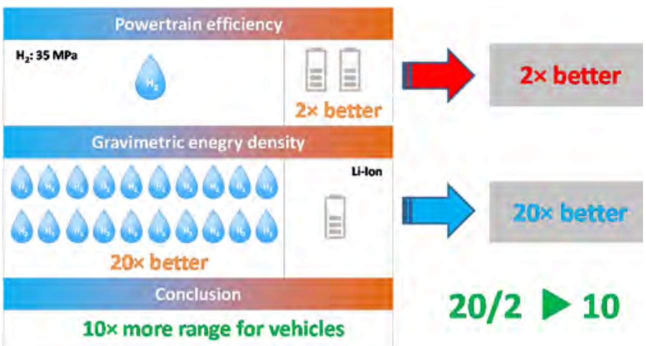

Fig. 2. Energy density of hydrogen at the pressure 35 MPa compared to Li-Ion batteries [35]

The production of hydrogen is still largely related to fossil fuels, and the cheapest method is still steam reforming of natural gas (the so-called grey hydrogen) – Fig. 3. Currently, 75% of the world's production of hydrogen comes from natural gas. Steam reforming with CO_2 capture is an interim production method. It is possible to use CCS (Carbon Capture Storage) or CCU (Carbon Capture Utilization) technology. Thanks to them, the produced hydrogen can be almost emission-free (referred to as blue hydrogen). The use of black coal for the process results in what is called black hydrogen to be produced while brown coal is used to make brown hydrogen (production of both these types of hydrogen results in CO_2 emissions). The production of hydrogen from methane in the pyrolysis process (often called turquoise hydrogen) results in the production of hydrogen and carbon in solid form.

Another, more modern method of hydrogen production is obtaining it through a nuclear reaction process. Such hydrogen is referred to as red hydrogen (or sometimes as pink or purple hydrogen).

The most desirable color of hydrogen is green – produced in the electrolysis process, the electricity of which comes exclusively from renewable sources.

If the energy comes from solar energy, the hydrogen produced is called yellow, and if the hydrogen production is powered from natural geological sources, it is referred to as white hydrogen.

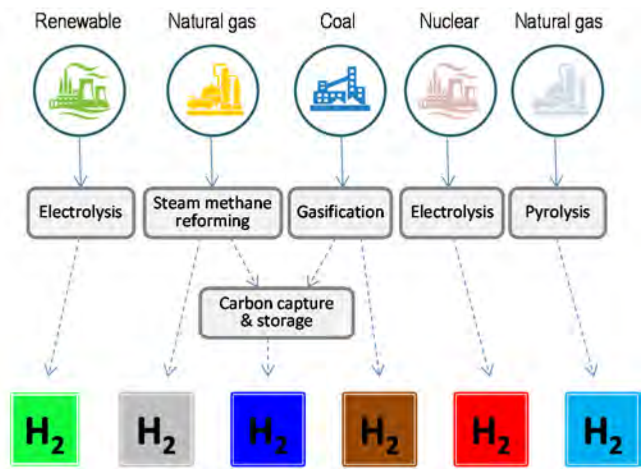

Fig. 3. Methods of hydrogen production and the associated "colors" of hydrogen made [15]

The characteristics of the types of hydrogen were presented in Table 1. Currently, 96% of hydrogen is produced from fossil fuels [13]. It is estimated that about 25% of net global warming in recent decades was caused by the release of methane. The production of 1 kg of hydrogen (grey) produces 13.3 kg of carbon dioxide. The efficiency of this process does not exceed 60%. The production of blue hydrogen produces

Table 1. Properties of different "colors" of hydrogen [3]

Characteristic	Green	Blue	Grey	Red	Turquoise	Brown
Energy source	Renewables	Natural gas or coal	Natural gas or coal	Nuclear	Natural gas	Brown coil
Feedstock	Water	Natural gas, coal, oil, biomass	Natural gas	Water	Natural gas	Brown coil, biomass
Technology	Electrolysis	Reforming + CCS, Gasification + CCS	Reforming, Gasification	Electrolysis	Pyrolysis	Gasification
By-products	Oxygen	CO_2	CO_2	Oxygen, nuclear waste	Carbon (as a solid)	CO_2
Motional environmental footprint	Minimal;	Low	Medium or high	Minimal GHG, nuclear waste products	Medium	High

only 1.7 kg of CO_2, with a process efficiency of 50%. Hydrogen from electrolysis accounts for only 4% of world production. The production of green hydrogen only causes 0.5 kg of CO_2.

The efficiency of the process is about 60–80%, however, its production (1 kg) requires about 9 dm^3 of water and an energy input of 50 kWh. The production of blue hydrogen causes CO_2 emissions of 1 kg (when produced from natural gas), and 2.4 kg (when produced from coal). Much higher values of carbon dioxide emissions are obtained in the production of grey (8.5 kg) or black (20 kg) hydrogen [39].

The consumption of hydrogen in the European Union in 2018 was 8.3 million tons [21]. The largest share of this was used by refineries (44%), ammonia production took about 34%, chemicals – 12% and other industries – about 10%. The largest producers of hydrogen in Europe are Germany (2.5 million tons per year) and the Netherlands (1.5 million tons). Annual hydrogen production in Europe in 2018 reached 11.5 million tons.

The Polish Hydrogen Strategy up to 2030 with a perspective of 2040 is a strategic document that defines the main goals of the development of the hydrogen economy in Poland and the directions and actions necessary to achieve those goals. Hydrogen has been classed by type into conventional, low-emission and renewable. Its detailed characteristics have been shown in Fig. 4.

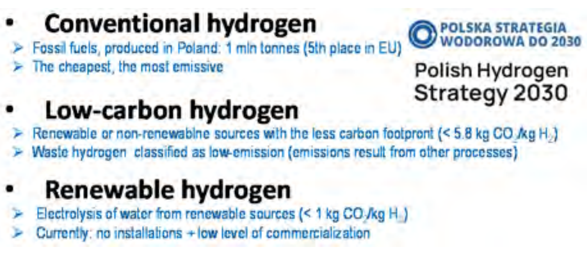

Fig. 4. Polish classification of hydrogen fuel [29]

2. Properties of hydrogen

Hydrogen is the lowest density gas (of all gases) being about 14 times lighter than air. In terms of energy density, it is the most efficient of all currently used fuels. Unlike other fuels, its combustion does not produce any other harmful by-products (however, it combines with atmospheric nitrogen to form nitrogen oxides). It can be stored in a liquefied or compressed form (Fig. 5). Hydrogen can be stored in compressed or liquefied form (at a temperature of –253°C). The curves relating to the change in volumetric energy density show much higher values for hydrogen stored in a liquefied form. The maximum storage values for compressed hydrogen are 70 MPa (composite tanks). Such tanks contain 71 kg/m^3 of liquefied hydrogen (at a temperature of 20 K, and pressure of 0.4 MPa), a value that is greater than when storing compressed hydrogen (39.1 kg/m^3 – at 70 MPa and room temperature).

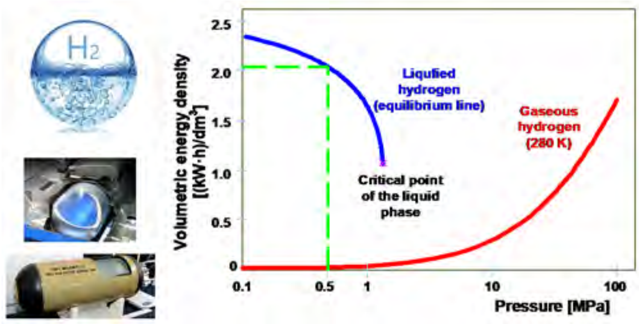

Fig. 5. Physical parameters of liquefied and compressed hydrogen [20]

Modern hydrogen storage solutions also use hybrid approaches in mixed systems, which use the features of cryogenic systems (LH_2 – liquefied hydrogen) and compressed hydrogen systems (CH_2 – compressed hydrogen) described in Fig. 6. In such conditions, hydrogen is kept at a temperature of about –233°C. Additionally, it is possible to use modern hydrogen-absorbing materials. Their applications increases the variety of hydrogen storage. At ambient pressure, the density of hydrogen is 0.3 g/dm^3, at 15 MPa it is 10 g/dm^3, at 35 MPa – 28 g/dm^3, and at 70 MPa – 40 g/dm^3. Liquefied hydrogen has a density of about 71 g/dm^3, however, hydrogen-absorbing materials may offer similar values or even exceed them: such as adsorbents (MOF-5 < 70 g/dm^3), metal hydrides – complex hydride (70–150 g/dm^3), chemically bound – chemical storage (70–150 g/dm^3) and water (111 g/dm^3) [30].

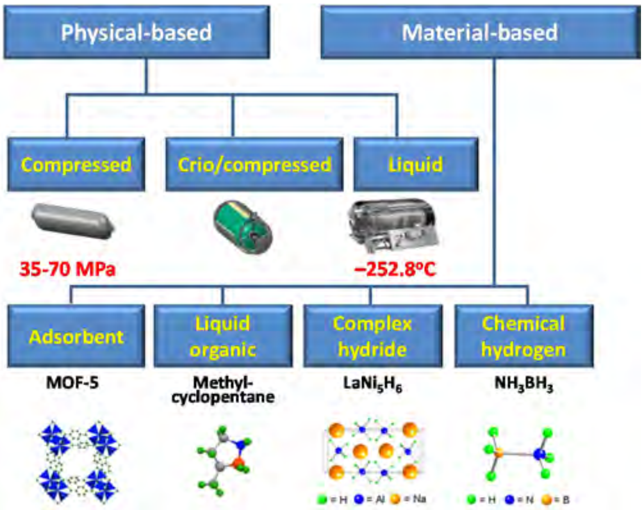

Fig. 6. Characteristics of hydrogen storage [14]

A comparative analysis of specific energies of various motor fuels shows high values of the volume density of liquid fuels (diesel oil, gasoline) – Fig. 7.

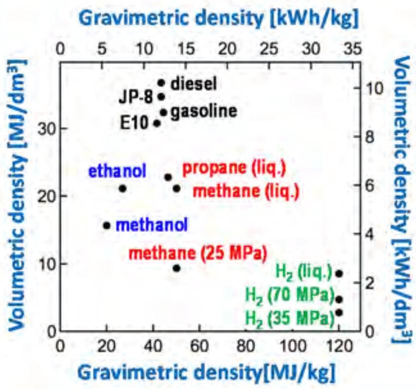

Fig. 7. Energy specifications for liquid and gaseous fuels (including hydrogen) [14]

Methanol and ethanol containing oxygen in their molecule have significantly lower values. Liquefied fuels (propane, methane) have similar values of volumetric density. Gaseous compressed fuels, such as hydrogen, exhibit the lowest volumetric density values. However, their mass indicators are completely different: the maximum values can be obtained using liquefied and compressed hydrogen. This is partly due to the nearly three times higher calorific value of hydrogen than other fuels. Gaseous fuels (even when compressed or liquefied) require a storage tank with a greater volume than needed for an equal mass of liquid fuels.

3. Hydrogen storage in vehicles

The outlined storage of hydrogen in liquefied or compressed form can be supplemented by intermediate conditions. These make it possible to limit the pressure of hydrogen (when compressed) with a simultaneous increase in its temperature (when liquefied). This is known as cryo-compressed hydrogen. Hydrogen in the liquefied form can reach a density of 63 g/dm^3 (Fig. 8). During its compression to 70 MPa and at t = 15°C, its density reaches the level of 40 g/dm^3. By limiting the pressure to 30 MPa while maintaining a temperature of 38 K (–235°C), it is possible to obtain a hydrogen density of 80 g/dm^3. This value is twice as high as during its compression (70 MPa). It is also a value greater than the previously indicated values for storage density in metal hydrides.

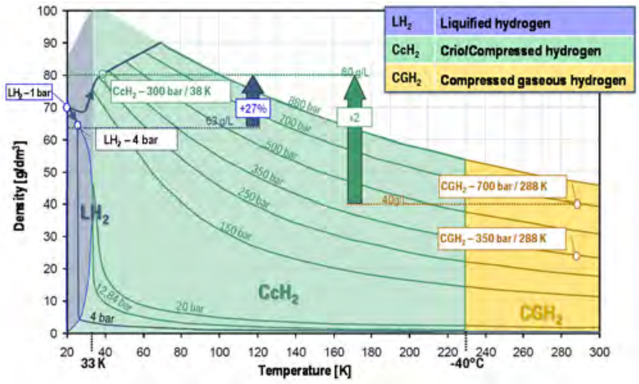

Fig. 8. Hydrogen storage conditions [5]

Steel tanks can be used for storing hydrogen compressed up to 35 MPa while also making it possible to use the cryo-compressed form of hydrogen storage (Fig. 9). The time it takes to refill hydrogen tanks is about 5 minutes, at the supply pressure: compressed gas (CH_2: 320 bar), or cryo-compressed gas (32 MPa). For example, in the considered vehicle tanks (Fig. 9), 260 kWh of energy (7.8 kg of hydrogen) can be stored in the cryo-compressed form, while in the compressed form this is only 83 kWh (2.5 kg H_2). Tank leakage losses are below 3 g/day (which is less than 1%/year).

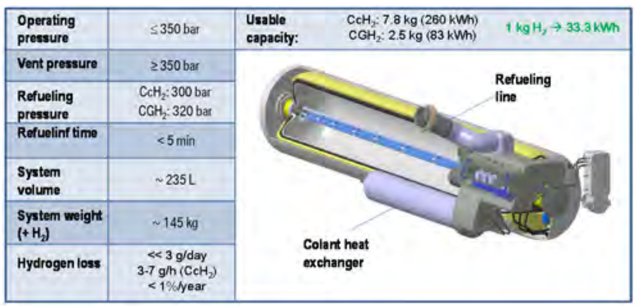

Fig. 9. Hydrogen fuel tanks [22]

Hydrogen is the fuel with the highest calorific value among all fuels for the transport sector, amounting to 120 MJ/kg (Fig. 10) and that value is independent of how it is stored. The volumetric energy of liquefied and cryo-compressed hydrogen are similar (the latter is 4% lower). Cryo-liquefied hydrogen densities are the highest (80 kg/m^3), about 15% greater than that of liquefied hydrogen, and about 50% greater than that of compressed hydrogen. The calorific value of methane is more than 2 times lower than that of hydrogen, and its storage may take a compressed or liquefied form. The energy differences of typical transport fuels were shown in Fig. 10.

Fuel	Composition	E [MJ/kg]	E [MJ/dm^3]	ρ [kg/m^3]	P [bar]	T [°C]
Diesel	C_9-C_{22}	41	34	820-845	ambient	ambient
Gasoline	C_4-C_{12}	43	32	710-770	ambient	ambient
GTL	C_9-C_{22}	43	34	775	ambient	ambient
LPG	Propane, buthane	46	25	540	2-8	ambient
CNG	Methane	50	9	160-190	200-250	ambient
LNG	Methane	50	21	400-500	8	–170/–130
CGH_2	Hydrogen	120	4,2	28-40	250-700	ambient
CcH_2	Hydrogen	120	9,6	80	280	–220
LH_2	Hydrogen	120	10	68	4	–240

Fig. 10. Fuels as energy sources for transport means [2, 7]

The transport performance indicators of the analyzed fuels were visualized in Fig. 11. The specific energy of hydrogen in liquefied and compressed form is similar, however, it is 7 times greater than the specific energy of Li-Ion batteries.

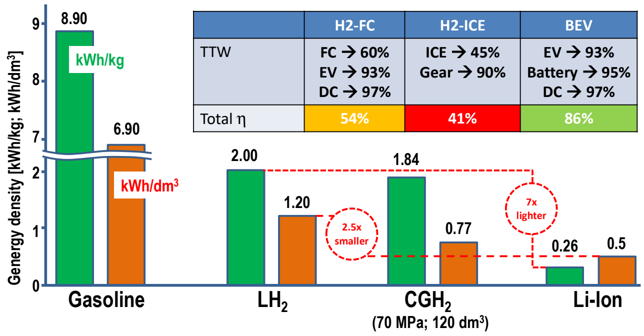

Fig. 11. Hydrogen vs. batteries in vehicle propulsion systems [18]

However, the scale of the technological progress to date has been determined by the energy density of gasoline, amounting to 8.9 kWh/kg. It should be noted that liquid fuels have an over four times greater energy density value. The comparison of the volumetric energy density leads to similar results. The benefit of using hydrogen comes from the analysis of its use in fuel cells and internal combustion engines. As a fuel it allows for zero-emission propulsion for means of transport along with high efficiency of drive system components.

4. Uses of hydrogen in combustion engines

Hydrogen supply for combustion engines has been a well-known topic since the 1950s. Currently, with the level of combustion systems development, hydrogen can be supplied in the form of direct or indirect injection (Fig. 12). Modern designs of hydrogen-powered engines exceed conventional units in terms of power, while achieving a similar level of torque. This is because direct hydrogen injection makes it possible to increase the density of the dose supplied to the cylinder. Indirect hydrogen injection displaced a part of the supplied air with fuel (even in a liquefied form) – Fig. 13. Direct injection enables full air intake with additional injection of the liquefied fuel. As a result over 20% more energy can be supplied, compared to conventional petrol injection in the standard PFI (Port Fuel Injection) system.

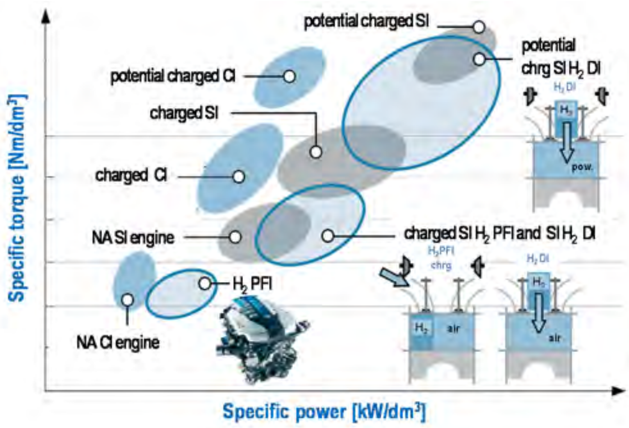

Fig. 12. Combustion engines concepts [17, 19]

Concepts of high-pressure and cryogenic injection of hydrogen into the cylinder are currently in development (Fig. 14). High-pressure hydrogen injection is to be performed at a pressure of 15–30 MPa and a temperature of –40–120°C. Such conditions make it possible to increase the energy density of the fuel. Cryogenic injection is considered as an indirect injection into the intake manifold.

In such conditions, injection is performed at a pressure of 3–6 bar (similar to typical PFI systems) and a temperature of –220–60°C. This eliminates the fuel dose losses due to hydrogen expansion (previously described for indirect gas injection).

Modern fuel injection in spark ignition engines is performed with the injector on the side or in the central location of the chamber (Fig. 15). Side injection (air-guided) allows lean loads to be burned to a limited extent. Spray-guided injection allows the complete combustion of lean liquid mixtures and is considered a future-proof solution in internal combustion engines.

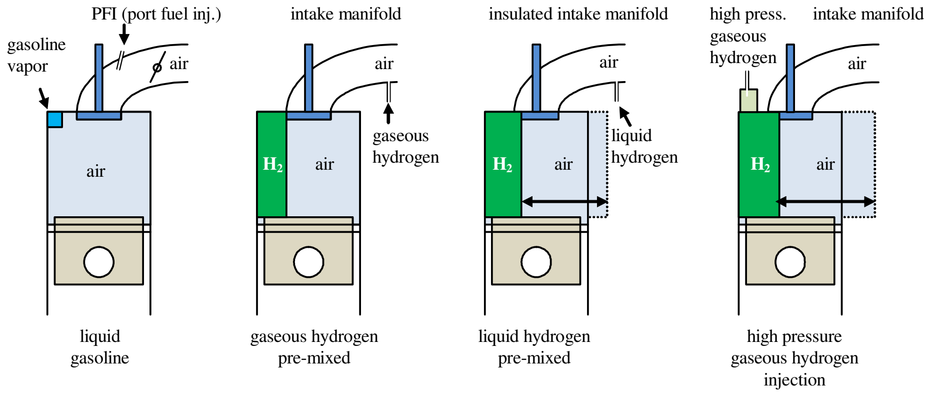

Fuel	17 cm³	300 cm³	405 cm³	420 cm³
Air	983 cm³	700 cm³	965 cm³	1000 cm³
Energy	3.5 kJ	3.0 kJ	4.0 kJ	4.2 kJ
% of energy	100 %	85 %	115 %	120 %

Fig. 13. Hydrogen injection systems for combustion engines [2, 4, 17]

Figure 15 shows a view of the combustion system that can be supplied using gas and cryogenic (indirect) injection. The presented mean indicated pressure characteristics point to a much greater potential of cryogenic fuel doses. 30% higher maximum p_e values (mean effective pressure, IMEP) were obtained with cryogenic fuel supply.

Modern hydrogen-powered combustion engines operate using lean mixture combustion (Fig. 16). This means that the characteristic peak in nitrogen oxide formation is skipped over. The air excess ratio ($\lambda = 2$) is achieved when burning hydrogen with a large excess of air (34 kg of air and 1 kg of fuel are needed for stoichiometric combustion). The hydrogen combustion conditions at $\lambda = 1.8$–2.0 require the use of an exhaust gas recirculation system to reduce the production of nitrogen oxides. For higher values of the air excess ratio, no additional exhaust aftertreatment system is required. Characteristic areas of engine load (intermediate and maximum) were also shown in Fig. 16. Hydrogen supply to the engine results in high overall efficiency values of the internal combustion engine – about 44% in terms of the engine torque and power curve. By comparing the nitrogen oxide concentration in a compression ignition engine and an engine fueled by hydrogen, significantly lower NO values have been observed when supplying the engine with hydrogen. With increasing engine rotational va-

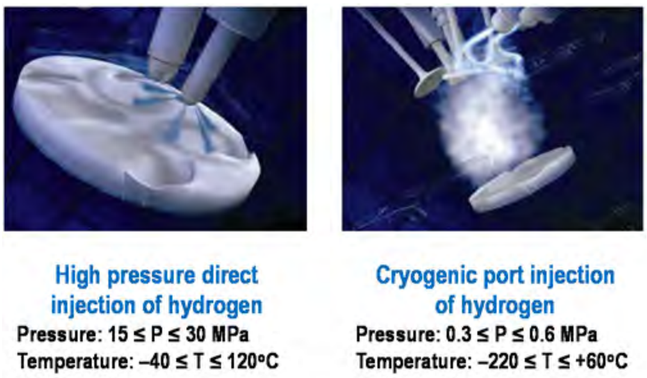

Fig. 14. Hydrogen supply systems in combustion engines [10]

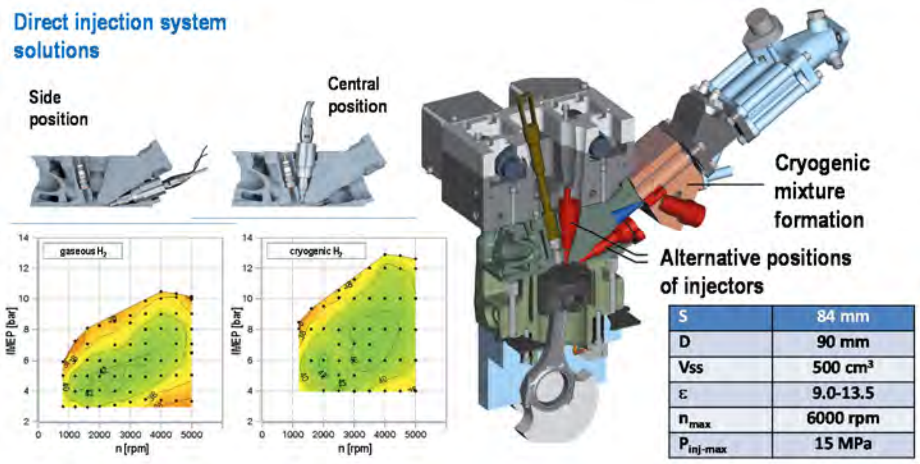

Fig. 15. Solutions for direct and indirect injection of hydrogen in an internal combustion engine [16]

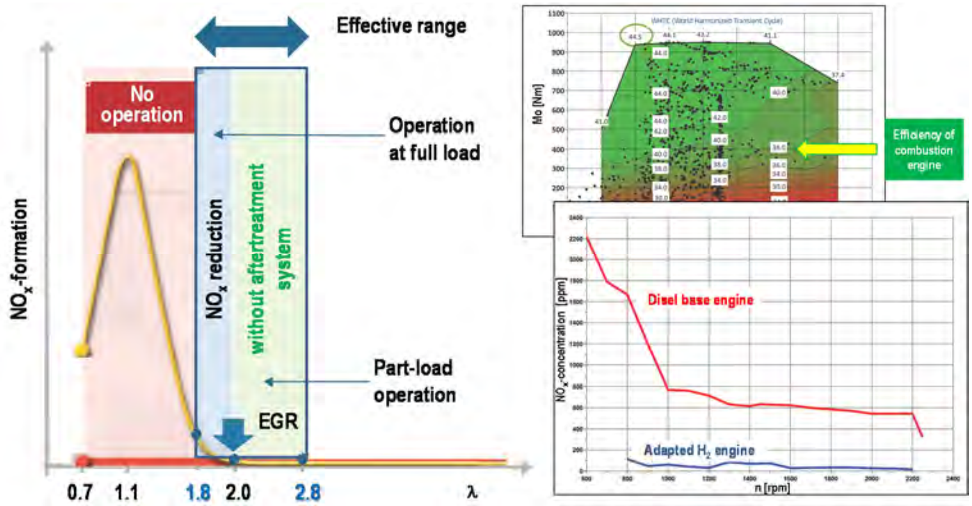

Fig. 16. Hydrogen injection and combustion in an internal combustion engine [33]

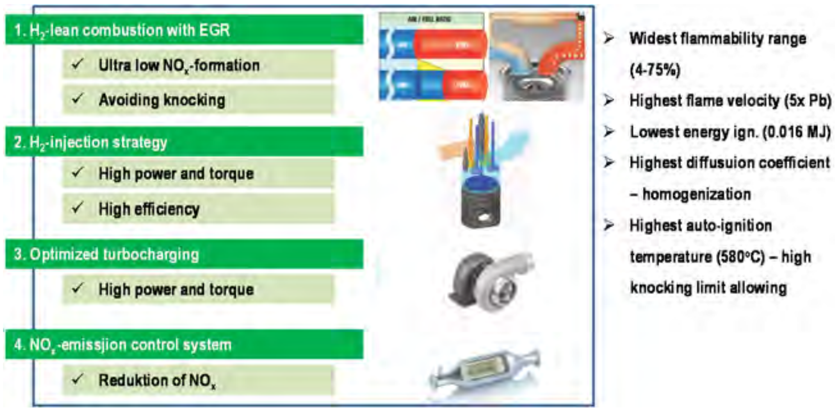

Fig. 17. Hydrogen combustion process in a combustion engine [33]

lues have been observed when supplying the engine with hydrogen. With increasing engine rotational speed, the NO concentration in the diesel exhaust gases decreases, while it remains almost constant in the hydrogen-powered engine, at about 6 times lower concentration level.

Combustion systems in piston engines have been adapted for the combustion of hydrogen. This solution results in a wide range of hydrogen flammability and a high combustion rate, about 5 times greater than the combustion of gasoline. Ignition requires very small amounts energy, and at the same time a high diffusion coefficient is achieved, which favors the formation of homogeneous mixtures. Low emission of nitrogen oxides and high resistance to engine knock was achieved by using a relatively large share of recirculated exhaust gases in the engine. This made it possible to lower the maximum combustion temperature as a result of limiting flame propagation in the cylinder. Other systems allowing for optimal hydrogen combustion have been shown in Fig. 17.

Combustion of hydrogen in an internal combustion engine requires a direct or indirect injection system to supply the hydrogen fuel (Fig. 18). Direct injection improves combustion quality resulting in better torque characteristics. The mean value of the rated power was found to increase by about 20% with the concentration of nitrogen oxides remaining at a constant value. The specific exhaust emission of nitrogen oxides related to the engine power will be lower as the engine power increases in such a scenario.

Increasing the engine power with direct hydrogen injection typically increases the concentration of nitrogen oxides. A significant reduction in their emission at the cost of a slight reduction in engine power can be achieved by using an exhaust gas recirculation system. Adequate fuel injection and ignition control (usually ignition delay) further reduces NO creation in the combustion chamber. Another step in NO exhaust emission reduction can be achieved by using exhaust aftertreatment systems. As a consequence, adoption of direct hydrogen injection can be expected to contribute to increasing engine power while reducing the exhaust emissions of nitrogen oxide.

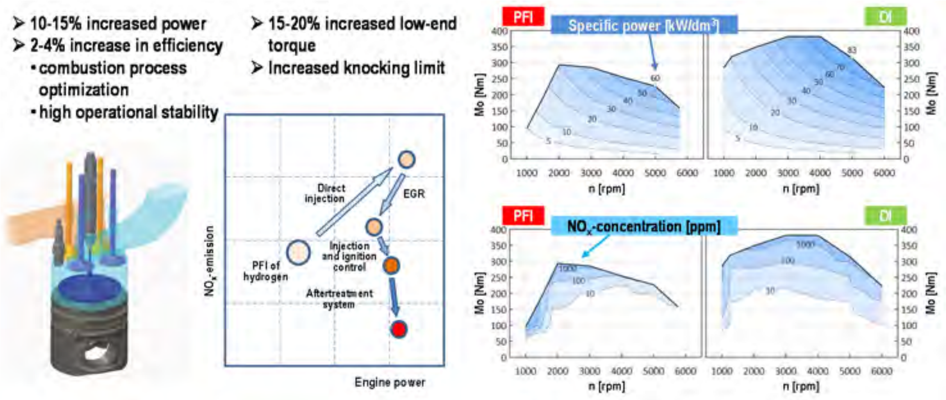

Fig. 18. Solutions for direct and indirect injection of hydrogen in a combustion engine [8, 28]

Combustion engines supplied with hydrogen fuel are used by Keyou. Modernized Deutz engines were chosen for this modification. Zero-emission heavy-duty combustion engines are defined as engines whose exhaust emissions are below 1 g CO_2/kWh (proposed in the EC Regulation No 595/2009). The vehicles shown in Fig. 19 are equipped with internal combustion engines with a stroke volume of 7.8 or 13.5 dm^3 (for those equipped with PFI systems) or 15 dm^3 (for those equipped with the DI – 40 t truck system).

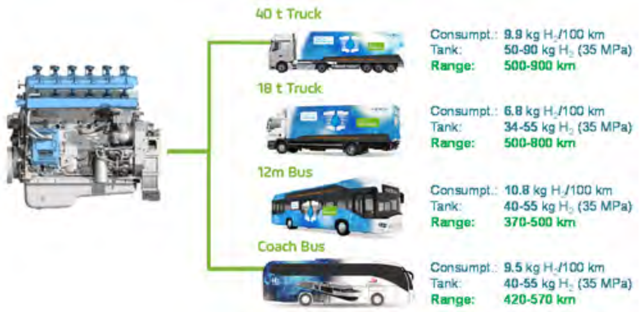

Fig. 19. Hydrogen for transport applications [33]

These vehicles consume approximately 10 kg of H_2 per 100 km. The minimum range of the vehicles is over 350 km while running on 35 MPa hydrogen tanks. Improving the design of hydrogen-powered engines increases their operational indicators. Changing the fuel injection method (indirect injection replaced with direct injection) not only increases the engine power, but also increases the torque. Changing the fuel delivery method not only increases the operational indicators of the engine, but also reduces the fuel consumption, which ultimately results in an increased efficiency of the entire drive unit (Fig. 20). A direct injection engine can mostly run at an air excess ratio of $\lambda > 2$. The exhaust emissions are, therefore, very low. A comparison with a compression ignition engine (the first value with diesel fuel, the second with hydrogen) shows significantly lower exhaust emission values (in g/kWh) for: CO_2 – 1.0:0.08; NO_x – 0.46:0.04; PM: 0.01:0.002; HC: 0.16:0.01 and CO: 4:0.01. Such low emission values indicate an exhaust emission reduction at a factor of 10 from a hydrogen-powered engine as compared to a diesel-powered engine.

Engine	MAN H2676 UH01 (2006)	DEUTZ TCG7.8 PFI	DEUTZ TCG7.8 DI
No. of cyl.	6	6	6
Vss	12.8 dm^3	7.8 dm^3	7.8 dm^3
Charging	Natural aspirated	Turbocharged	Turbocharged
Ne	150 kW	180 kW	210 kW +130% power
Mo	760 Nm	950 Nm	1100 Nm
Combustion	Stoichiometric	Lean	Lean
NO_x-reduction	Tree-way catalyst	EGR + H_2 SCR	EGR + H_2 SCR −60%
H_2-consumption	21.6 kg H_2/100 km	10.7 kg H_2/100 km	9.7 kg H_2/100 km

Fig. 20. Development of hydrogen powered engines [33]

5. Conclusions

The use of hydrogen in internal combustion engines is an alternative to the combustion of fossil fuels (gasoline, diesel oil). The use of hydrogen makes it possible to significantly reduce the exhaust emissions of not only carbon dioxide, but also other components of the exhaust gas.

Hydrogen as a fuel for the internal combustion engines (ICE):

a) is used in demonstration vehicles such as passenger cars, trucks and buses (engines displacement about 1.5–15 dm^3),

b) is used in ICE with small displacement and power, does not make it suitable for railway applications at present.

The use of hydrogen as a fuel for vehicles to be converted into power in fuel cells also enables further propagation of hydrogen in vehicle propulsion systems and the transport sector. It should be noted that 1 kg of hydrogen produces 33 kWh of energy, while that value from fossil fuels is 2.4 times lower. This difference in energy potential indicates the desirability of using hydrogen-based propulsion systems and of hydrogen as fuel in means of transport. Contemporary alternative fuel supply projects indicate an increased interest in propulsion systems using fuel cells as well as hydrogen-powered internal combustion engines.

Nomenclature

CcH_2	crio/compressed hydrogen
CCS	carbon capture storage
CCU	carbon capture utilization
CH_2	compressed hydrogen (CGH_2)
CI	compression ignition
CNG	compressed natural gas
DI	direct injection
EGR	exhaust gas recirculation
GHG	greenhouse gas
GLT	gas-to-liquid
HC	hydrocarbons
HCCI	homogeneous charge compression ignition
IMEP	indicated mean effective pressure
LH_2	liquefied hydrogen
Li-Ion	lithium-ion battery
LNG	liquefied natural gas
LPG	liquefied petroleum gas
Mo	engine torque
Ne	engine power
NO	nitrogen oxide
PFI	port fuel injection
PM	particulate matter
RCCI	reactivity controlled compression ignition
SCR	selective catalysts reduction
SI	spark ignition
TJI	turbulent jet ignition
Vss	displacement
λ	air excess ratio

Bibliography

[1] Ahluwalia R.K., Hua T.Q., Peng J.-K. et al. Technical assessment of cryocompressed hydrogen storage tank systems for automotive applications. *International Journal of Hydrogen Energy*. 2010, **35**(9), 4171-4184. https://doi.org/10.1016/j.ijhydene.2010.02.074

[2] Akal D., Öztuna S., Büyükakın M.K. A review of hydrogen usage in internal combustion engines (gasoline-LPG-diesel) from combustion performance aspect. *International Journal of Hydrogen Energy*. 2020, **45**(60), 35257-35268. https://doi.org/10.1016/j.ijhydene.2020.02.001

[3] Broadleaf Capital International Pty Ltd. The colour of hydrogen. https://broadleaf.com.au/resource-material/the-colour-of-hydrogen/

[4] Bureika G., Matijošius J., Rimkus A. Alternative carbonless fuels for internal combustion engines of vehicles. Ecology in transport: Problems and solutions. *Lecture Notes in Networks and Systems*. 2020, **124**. Springer, Cham. https://doi.org/10.1007/978-3-030-42323-0_1

[5] Burke A., Zhao H. Fuel cells and hydrogen in long-haul trucks. *Sustainable Transportation Energy Pathways*. University of California, Davis, California, May 2017.

[6] Distaso E., Amirante R., Cassone E. et al. Analysis of the combustion process in a lean-burning turbulent jet ignition engine fueled with methane. *Energy Conversion and Management*. 2020, **223**, 113257. https://doi.org/10.1016/j.enconman.2020.113257

[7] Durzyński Z. Hydrogen-powered drives of the rail vehicles (part 1). *Rail Vehicles/Pojazdy Szynowe*. 2021, **2**, 29-40. https://doi.org/10.53502/RAIL-139980

[8] Eichlseder H., Grabner P., Schaffer K. Internal combustion engine – an alternative energy converter for hydrogen. *Graz University of Technology*, 06/16/2020. https://www.tugraz.at/tu-graz/services/news-stories/planet-research/einzelansicht/article/internal-combustion-engine-an-alternative-energy-converter-for-hydrogen/

[9] Electrolyser market outlook. Decarbonate Co-Innovation project. https://www.decarbonate.fi/wp-content/uploads/2020/09/Decarbonate_hydrogen_webinar_10062020.pdf

[10] Ellgas S. Simulation of a hydrogen internal combustion engine with cryogenic mixture formation. *Cuvillier Verlag*, Goettingen 2008. https://cuvillier.de/uploads/preview/public_file/3228/9783867275293.pdf

[11] Farzaneh-Gord M., Saadat-Targhi M., Khadem J. Selecting optimal volume ratio of reservoir tanks in CNG refueling station with multi-line storage system. *International Journal of Hydrogen Energy*. 2016, **41**(48), 23109-23119. https://doi.org/10.1016/j.ijhydene.2016.10.050

[12] Hirscher M. (Ed.). Handbook of Hydrogen Storage: New Materials for Future Energy Storage. *John Wiley & Sons*, Weinheim, March 2010. https://onlinelibrary.wiley.com/doi/book/10.1002/9783527629800

[13] Howarth R.W., Jacobson M.Z. How green is blue hydrogen? *Energy Science & Engineering*. 2021, **9**, 1676-1687. https://doi.org/10.1002/ese3.956

[14] Hydrogen and Fuel Cell Technologies Office. https://www.energy.gov/eere/fuelcells/hydrogen-storage (27.01.2022).

[15] Hydrogen as an Energy Carrier. Clean, safe solution for global decarbonisation. 2022 Schlumberger. https://newenergy.slb.com/new-energy-sectors/hydrogen-as-an-energy-carrier (27.01.2022).

[16] HyICE – Optimization of the hydrogen internal combustion engine. Summary of an integrated project in the 6th Framework Programme of the European Commission. February 2007.

[17] Kiesgen G., Berger E., Rottengruber H. Hydrogen internal combustion engines for vehicle generations of the future. *AutoTechnology*, 2006, **6**, 40-43. https://doi.org/10.1007/BF03246951

[18] Kircher O., Greim G., Burtscher J. et al. Validation of cryo-compressed hydrogen storage (CcH2) – a probabilistic approach. *International Conference on Hydrogen Safety*. San Francisco, September 12-14, 2011. http://conference.ing.unipi.it/ichs2011/papers/258.pdf

[19] Korn T. The new highly efficient hydrogen internal combustion engine as ideal powertrain for the heavy-duty sector. *Internationaler Motorenkongress 2019*. Proceedings. Springer Vieweg, Wiesbaden. https://doi.org/10.1007/978-3-658-26528-1_23

[20] Krainz G., Bartlok G., Bodner P. et al. Development of automotive liquid hydrogen storage systems. *AIP Conference Proceedings*. 2004, **710**(35). https://doi.org/10.1063/1.1774664

[21] Kto zarobi na polskim wodorze? 4.11.2020. https://wysokienapiecie.pl/32899-kto-zarobi-na-polskim-wodorze/

[22] Kunze K., Kircher O. Cryo-compressed hydrogen storage cryogenic cluster day, *BMW EfficientDynamics*. Oxford, September 28, 2012.

[23] Lee P.-Y., Park S., Cho I. et al. Vibration-based degradation effect in rechargeable lithium ion batteries having different cathode materials for railway vehicle application. *Engineering Failure Analysis*. 2021, **124**, 105334. https://doi.org/10.1016/j.engfailanal.2021.105334

[24] Li C., Wang Z., He Z. et al. An advance review of solid-state battery: challenges, progress and prospects. *Sustainable Materials and Technologies*. 2021, **29**, e00297. https://doi.org/10.1016/j.susmat.2021.e00297

[25] Liu P., Zhong L., Zhou L. et al. The ignition characteristics of the pre-chamber turbulent jet ignition of the hydrogen and methane based on different orifices, *International Journal of Hydrogen Energy*. 2021, **74** (46), 37083-37097. https://doi.org/10.1016/j.ijhydene.2021.08.201

[26] Murali A., Sakar M., Priya S. Insights into the emerging alternative polymer-based electrolytes for all solid-state lithium-ion batteries: a review. *Materials Letters*. 2022, **313**, 131764. https://doi.org/10.1016/j.matlet.2022.131764

[27] Oikawa M., Kojiya Y., Sato R. et al. Effect of supercharging on improving thermal efficiency and modifying combustion characteristics in lean-burn direct-injection near-zero-emission hydrogen engines. *International Journal of Hydrogen Energy*. 2022, **47**(2), 1319-1327. https://doi.org/10.1016/j.ijhydene.2021.10.061

[28] Pauer T., Weller H., Schünemann E. et al. H_2 ICE for future passenger cars and light commercial vehicles. *41th International Vienna Motor Symposium, Fortschrittberichte VDI*. Vienna 2020, 12.

[29] Polska Strategia Wodorowa do roku 2030 z perspektywą do roku 2040. Ministerstwo Klimatu i Środowiska. Warszawa 2021. https://www.gov.pl/web/klimat/polska-strategia-wodorowa-do-roku-2030

[30] Ren J., North B.C. Shaping porous materials for hydrogen storage applications: a review. *Journal of Technology Innovations in Renewable Energy*. 2014, **3**, 12-20. https://doi.org/10.6000/1929-6002.2014.03.01.3

[31] Shinde B.J., Karunamurthy K. Recent progress in hydrogen fuelled internal combustion engine (H2ICE) – a comprehensive outlook. *Materials Today: Proceedings*. 2021. https://doi.org/10.1016/j.matpr.2021.10.378

[32] Slattery M., Dunn J., Kendall A. Transportation of electric vehicle lithium-ion batteries at end-of-life: a literature review. *Resources, Conservation and Recycling*. 2021, **174**, 105755. https://doi.org/10.1016/j.resconrec.2021.105755

[33] Sousa A. The hydrogen combustion engine as the most effective CO_2-reduction technology today. Keyou. TU-Berlin, 21.11.2019.

[34] Srinivasan J., Swamy A.K., Madanagopalan P. et al. Performance and emission characteristics of a methane fuelled HCCI engine at various injection location and operating speed. *Materials Today: Proceedings*. 2021, **46**(2), 1022-1027. https://doi.org/10.1016/j.matpr.2021.01.216

[35] The most effective technology to comply with CO_2-legislation: the new generation of hydrogen internal combustion engines. Keyou, September 2020.

[36] Wang L., Liu J., Ji Q. et al. Experimental study on the high load extension of PODE/methanol RCCI combustion mode with optimized injection strategy. *Fuel*. 2021, **122726**. https://doi.org/10.1016/j.fuel.2021.122726

[37] Xu J., Lin W. Research on systems for producing liquid hydrogen and LNG from hydrogen-methane mixtures with hydrogen expansion refrigeration. *International Journal of Hydrogen Energy*. 2021, **46**(57), 29243-29260. https://doi.org/10.1016/j.ijhydene.2020.10.251

[38] Yilmaz I.T. The effect of hydrogen on the thermal efficiency and combustion process of the low compression ratio CI engine. *Applied Thermal Engineering*. 2021, **197**, 117381. https://doi.org/10.1016/j.applthermaleng.2021.117381

[39] Yu M., Wang K., Vredenburg H. Insights into low-carbon hydrogen production methods: green, blue and aqua hydrogen. *International Journal of Hydrogen Energy*. 2021, **46**(41), 21261-21273, https://doi.org/10.1016/j.ijhydene.2021.04.016

Article citation info:
Kuczyk M., Jędrzejewski P., Załuski P. Stress analysis of suspended rail vehicle bogie. *Rail Vehicles/Pojazdy Szynowe*. 2022, 1-2, 20-29.
https://doi.org/10.53502/RAIL-149199

Rail Vehicles/Pojazdy Szynowe

www.railvehicles.eu

Stress analysis of suspended rail vehicle bogie

Mateusz **Kuczyk** [a, *], Piotr **Jędrzejewski** [a], Paweł **Załuski** [a]

[a] *Faculty of Mechanical Engineering and Ship Technology, Gdansk University of Technology, Poland*

ARTICLE INFO

Received: 9 January 2022
Revised: 3 April 2022
Accepted: 13 April 2022
Available online: 17 April 2022

KEYWORDS

bogie frame
wheelset
stress analysis
monorail
fine element method (FEM)

The main topic of this article is the strength analysis of selected bogie components – the wheelset axle and the frame. Axle calculations were based on the analytical method and were conducted with different types of materials. The finite element method was used for verification of bogie frame construction and loads applied on the frame were calculated according to the PN-EN 13749 norm. The bogie is a part of suspended electric multiple unit which was main matter of authors' master thesis: „The concept of suspended railway engine wagon", conducted on Mechanical Engineering Faculty of Gdansk University of Technology.

1. Vehicle description

Suspended railway is an unusual means of transport used in urban areas. Characteristic feature of such vehicles is that car body hangs several meters above the ground level, so it's completely independent from traffic system. Currently, there can be highlighted two distinctive suspended monorail systems in the world that function as an urban means of transportation: SAFEGE system that originated in France but is used in Japan (the vehicle uses bogies with rubber wheels which move in a closed guidebeam) and Eugen Langen system from German city of Wuppertal (the vehicle is asymmetrically suspended under bogies equipped with a pair of double-flanged wheels cooperating with a single rail). In general, the suspended monorail can be treated as a cheaper alternative to underground railways with a slightly smaller capacity [12, 14].

Considering the above, it seems that vehicles of this type have a greater potential than their marginal use in public transportation. That is why the authors decided to propose their own solution – bidirectional, three-section electric multiple unit (Fig. 1).

Proposed vehicle is suspended symmetrically under the guideway beam which accommodates two steel rails, so the rolling stock uses wheel-rail guidance system (Fig. 2).

Fig. 1. View of proposed suspended railway vehicle [6]

In such a case rail surface is protected from weather conditions that ensures relatively high and stable value of adhesion coefficient. A current collector device is used to supply the rolling stock in electrical power from a third rail. However electrical circuit must be closed and that function is done by wheel-rail contact (a detailed description of proposed solution

* Corresponding author: mateusz.kuczyk@gmail.com (M. Kuczyk)

can be found in other authors' publications [7–9]). Authors' vehicle, in comparison with existing solutions, is characterised by high: capacity, velocity and dynamics. Chosen properties of the rolling stock are presented in Table 1 [6].

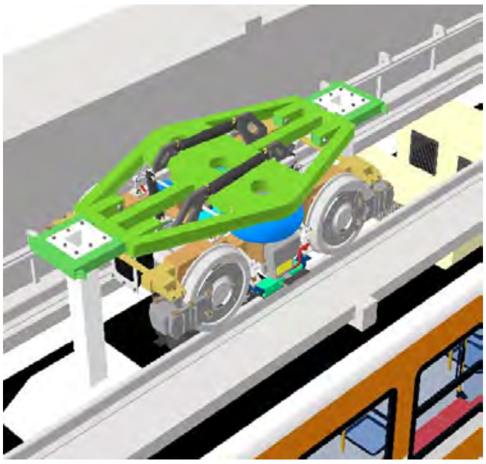

Fig. 2. Rail vehicle bogie in guideway beam [6]

Table 1. Technical specification of suspended EMU

Feature	Unit	Value	Feature	Unit	Value
Overall length	mm	32 580	Maximal acceleration	m/s^2	1.30
Width of the car body	mm	2 500	Maximum braking deceleration	m/s^2	3.60
Height of the car body	mm	3 025	Axle arrangement	–	1A'+1A'+1A'
Empty carriage mass	kg	43 611	Wheel diameter	mm	700/750
Maximum vehicle mass	kg	71 811	Bogie centre distance	mm	10 680
Total capacity	–	376	Wheelbase	mm	1 600
Seating capacity	–	80	Track gauge	mm	1 435
Total vehicle power	kW	840	Total mass of the bogie	kg	5 475
Maximum speed	km/h	70	Pressure of the wheelset on a track	t	11,97

For the authors the most important and interesting part of the rolling stock is the bogie (Fig. 3), which could be characterized by:

- low weight, which was achieved by the use of inboard bearings and short wheelbase;
- good running characteristics in a curved track, thanks to: a short wheelbase, elastic wheelset guidance in the bogie frame (quasi-radial adjustment of wheelset in curved track) and wheel flange lubrication system;
- low unsprung mass, which results from the fully sprung gear unit and traction motor, moreover an axle length reduction (inboard bearing);
- high passenger comfort, through two staged suspension system (especially air springs in the secondary suspension);
- good dynamic properties in consequence of using high power motor which also helps the vehicle to move on a steep gradient track.

The rolling stock car body is suspended under three identic two-axle, motor bogies with only one powered axle. Such unusual axle arrangement of the rolling stock is a consequence of using simultaneously double-stage gear and high power motor in bogie with inboard bearings and short wheelbase. Moreover, the lack of space in the bogie frame results in low and longitudinal arrangement of the motor, so its shaft axis lies on the plane passing through both railheads. As key components in terms of safety, bogie frame and wheelset axle was chosen by the authors for the strength analysis. The following chapters present method of load and stress calculation with a short description of the results. At this point it should be noted that the literature devoted directly to suspended monorail vehicles is sparse and largely focuses on issues related to vehicle dynamics (e.g. [3] or [5]) and safety (e.g. [1]).

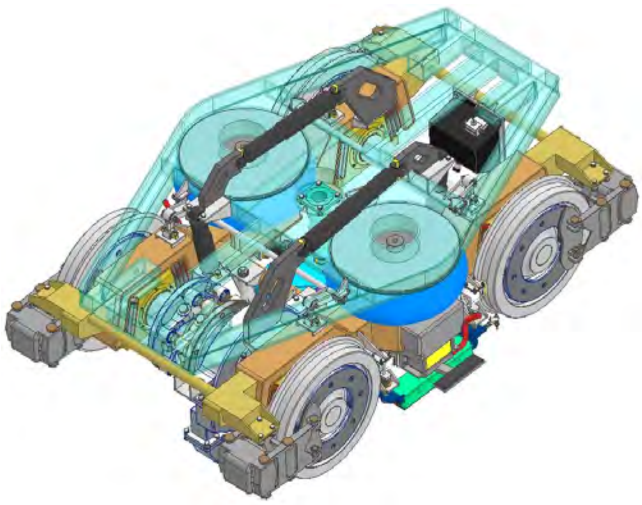

Fig. 3. Bogie construction [6]

2. Axle strength analysis

Inboard bearings, beside mentioned advantages, allow a reduction in bending moment acting on the axle that permitted diameter reduction. However, axleboxes must be fitted onto the axle before the wheels, so access to them is limited. To reduce maintenance activities on the bearings, in the axlebox was used a compact tapered bearing unit with integrated seals and sensors. Only on the wheelset axle strength analysis was conducted and it was based on the analytical method. Wheelset load was defined by calculation methodology according to [11] and [15]. The unusual construction of the presented vehicle (the centre of gravity significantly below the upper surface of the rail head and the location of the bearings – support points, between the wheels) forced the authors to adapt the formulas to the obtained computational model Fig. 4 – by transforming the moment equation taking into account the opposite turns of moments generated by individual forces.

2.1. Determination of wheelset load

In the calculation was considered stress in five cross-sections (Fig. 4):

- I and V – wheel-mounted area of the axle, diameter 0.12 m;
- II and IV – axlebox-mounted area of the axle, diameter 0.13 m;
- III – centre of the axle, diameter 0.15 m.

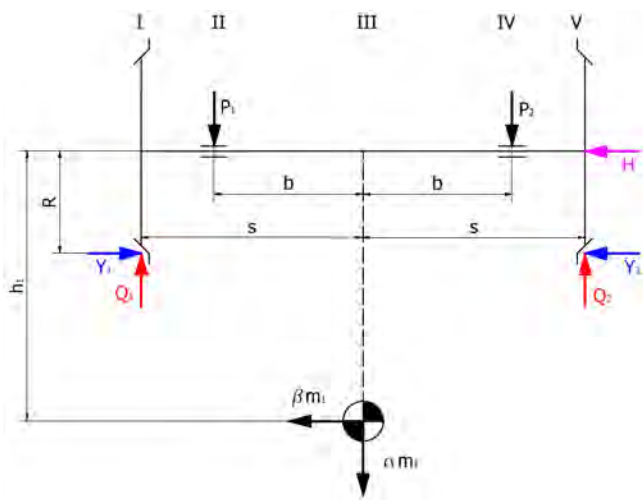

Fig. 4. Calculation model of wheelset [6]

Furthermore, the calculation considered only the worst-case scenario where vehicle is fully loaded. Necessary for load determination were following values (determined on basis of the 3D CAD model of the vehicle prepared by the authors, presented in [6–9]):

- mass of the vehicle per wheelset axle – m_1 = 11,969 kg (in static case and with assumption that vehicle weight is equally distributed between axles);
- distance between axlebox centre plane and the centre of gravity – b = 0.497 m;
- distance between wheelset axle and the centre of gravity – h_1 = 2.750 m;
- wheel rolling radius – R = 0.375 m;
- distance between wheel centre plane and the centre of gravity – s = 0.748 m;
- vertical acceleration – α = 2.423 m/s^2;
- horizontal acceleration – β = 1.472 m/s^2.

The forces from the Fig. 5 were defined and calculated in the following manner:

- P_1 – vertical force acting on the axlebox, represents empty vehicle:

$$P_1 = \frac{\beta \cdot m_1 \cdot h_1 - m_1 \cdot b \cdot (g+\alpha)}{2 \cdot b} = 24\,608\ \text{N} \tag{1}$$

- P_2 – vertical force acting on the axlebox, represents fully loaded vehicle:

$$P_2 = \frac{\beta \cdot m_1 \cdot h_1 + m_1 \cdot b \cdot (g+\alpha)}{2 \cdot b} = 122\,155\ \text{N} \tag{2}$$

- Y_1 – transverse guiding force acting between wheel flange and rail on the side of less loaded axlebox, during motion along a curved track:

$$Y_1 = 0.15 \cdot m_1 \cdot g = 17\,612\ \text{N} \tag{3}$$

- Y_2 – transverse guiding force acting between wheel flange and rail on the side of more loaded axlebox, during motion along a curved track:

$$Y_2 = 0.30 \cdot m_1 \cdot g = 35\,223\ \text{N} \tag{4}$$

- H – horizontal force balancing transverse guiding forces:

$$H = Y_2 - Y_1 = 17\,612\ \text{N} \tag{5}$$

- Q_1 – reaction force acting on the less loaded axlebox:

$$Q_1 = \frac{P_1 \cdot (s+b) + P_2 \cdot (s-b) + R \cdot (Y_1 - Y_2)}{2 \cdot s} = 45\,403\ \text{N} \tag{6}$$

- Q_2 – reaction force acting on the more loaded axlebox:

$$Q_2 = \frac{P_2 \cdot (s+b) + P_1 \cdot (s-b) + R \cdot (Y_2 - Y_1)}{2 \cdot s} = 101\,360\ \text{N} \tag{7}$$

The addition of a vertical reaction forces and forces acting on the axleboxes is equal, so obtained results are correct.

2.2. Determination of axle load

The calculation model (Fig. 5) considers all forces acting on the wheelset, but it assumes that transverse guiding forces are represented by bending moments. Moreover, whole length of the axle was loaded by a torque, which value was equal to tractive torque (it's higher than braking torque even when the highest value of adhesion coefficient has been assumed).The calculations considered three different types of materials of the axle: EA1N, EA4T and 30NiCrMoV12.

The first one is normalized carbon steel and it's the most commonly used material. The second one is quenched and tempered low alloyed steel and it's used for more loaded axles. The last one is high strength alloyed steel which is used in hollow axles of a high-speed railway rolling stocks. High properties of such material permit reducing axle diameter, so unsprung mass of a vehicle is lower. The most important properties, for the strength analysis, of mentioned materials are presented in Table 2 (this and the following tables are at the end of the article), based on [11].

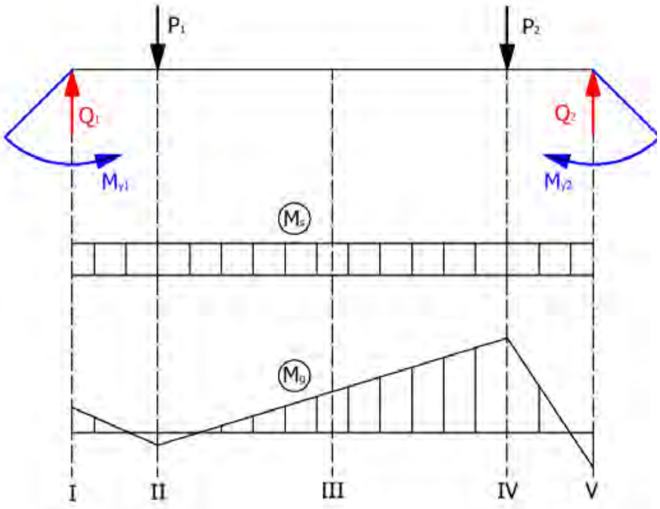

Fig. 5. Calculation model of the wheelset axle [6]

Values of an allowable stress and safety factors was determined by fatigue tests. Additionally, there were considered hollow axles (bore diameter 60 mm) which lower the weight of the wheelset, so it is also a decrease of unsprung mass of a whole bogie. Obtained results were presented in Table 3 [6] and on their basis there could be made only one conclusion – that, with such specified dimensions, it must be solid axle made of EA4T steel or hollow axle made of 30NiCrMoV12. Application of second, more expensive material, allows only for relatively low mass reduction, that it is more reasonable to use a solid axle made of EA4T steel. Additionally in the context of the presented results, it should be noted that the placement of the bearing nodes on the inside of the wheels (troublesome in the context of the operation and maintenance of the vehicle) reduces the value of the maximum torque acting on the axle, and thus also reduces the stresses occurring in it.

3. Frame strength analysis

The bogie frame (Fig. 6) is an internal, closed three-section, welded construction which consists of:

- two closed box-shaped construction side-sills (Fig. 6, No 1) made of 10 mm thick plate of the S355 steel (yield point – 355 MPa, tensile strength – 520 MPa);
- two central cross-bar pipes (Fig. 6, No 2) which are characterized by an outside diameter of 100 mm and inside diameter of 70 mm;
- two pipe headstocks (Fig. 6, No 3) which are characterized by an outside diameter of 60 mm and inside diameter of 30 mm;

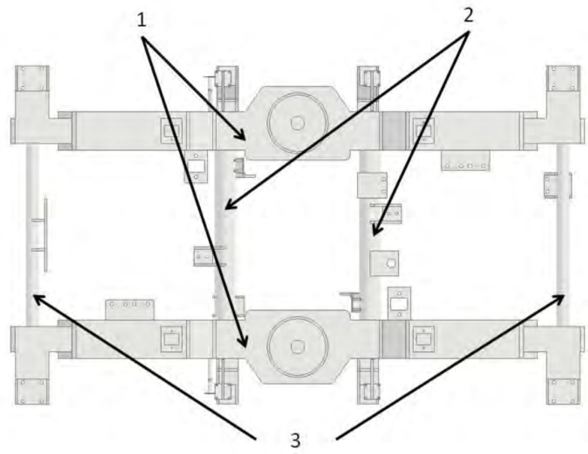

Fig. 6. Bogie frame [6]

The frame weighs only 604 kg. Shape of the side-sills permits chevron springs to wheelset guidance.

Bogie frame strength analysis was based on the standard PN-EN 13749 [10], so there were done static calculations with exceptional and service loads. Additionally, in the calculations were considered cases with frame attachments loads.

3.1. Static analysis

In order to determine the loads acting on the frame following values were used (on the basis of the 3D CAD model of the vehicle prepared by the authors, presented in [6–9]):

- total mass of empty vehicle – $M_v = 43\ 611$ kg;
- mass of maximal load – $m_p = 28\ 200$ kg;
- mass of real service load – $m_{pe} = 21\ 075$ kg;
- mass of the bogie – $m^+ = 4\ 800$ kg;
- number of axles in the bogie – $n_a = 2$;
- number of bogies in the rolling stock – $n_b = 3$;
- roll coefficient – $\alpha = 0.1$;
- bounce coefficient – $\beta = 0.2$.

In carried out calculations on the bogie frame acted:

- vertical forces caused by suspended mass acceleration, with:
  - exceptional load:

$$F_{z1max} = \frac{1.4 \cdot g \cdot (M_v + m_p - n_b \cdot m^+)}{n_a \cdot n_b} \tag{8}$$

  - service load:

$$F_{z1} = \frac{g \cdot (M_v + 1.2 \cdot m_{pe} - n_b \cdot m^+)}{n_a \cdot n_b} \tag{9}$$

  - transverse forces resulting from:
  - exceptional load:

$$F_{ymax} = 2 \cdot \left(10^4 + \frac{(M_v + m_p) \cdot g}{3 \cdot n_a \cdot n_b}\right) \tag{10}$$

  - service load:

$$F_y = 2 \cdot \left(\frac{(M_v + 1.2 \cdot m_{pe}) \cdot g}{3 \cdot n_a \cdot n_b}\right) \tag{11}$$

- longitudinal forces resulting from:
  – exceptional load:

$$F_{xmax} = 0.1 \cdot (2 \cdot F_{z1max} + m^{+} \cdot g) \qquad (12)$$

  – service load:

$$F_{x} = 0.05 \cdot (2 \cdot F_{z1} + n_{b} \cdot m^{+} \cdot g) \qquad (13)$$

  – forces resulting from a track twist.

Previous formulas were based on calculation methodology presented in the [2] and [16]. Considering that the above calculations relate to the case of a static frame load, the location of the center of gravity of the vehicle below the rail head (with the use of a special suspension of the car body – forces resulting from the weight of the vehicle are applied to the upper surfaces of the side-sills), does not affect the calculation method, which directly allows on the adaptation of formulas from the cited sources. All load cases, with number values of applied forces, were compared in the Table 4 [6]. Different values of the vertical forces in service cases are caused by α and β coefficients, so value of:

- 62 376 N refer to $F_{z1/2} \cdot (1 - \alpha - \beta)$;
- 80 198 N refer to $F_{z1/2} \cdot (1 + \alpha - \beta)$;
- 98 020 N refer to $F_{z1/2} \cdot (1 - \alpha + \beta)$;
- 115 842 N refer to: $F_{z1/2} \cdot (1 + \alpha + \beta)$.

In the calculation model (Fig. 7) were imposed boundary conditions, so all planes supported on the chevron springs in primary suspension were fixed. In cases which considered a track twist, half of the supported planes were left free and they were loaded with rail reaction forces.

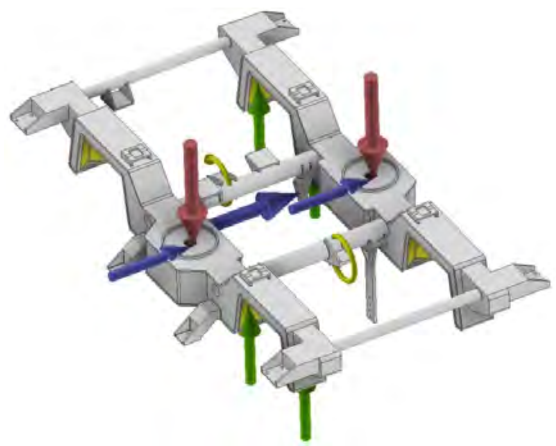

Fig. 7. Load of the bogie frame in exceptional and service cases [6]

Vertical and a part of the transverse forces were applied on the interfaces between bogie frame and secondary suspension. Rest of the transverse load was applied on the car body movements limiter. Longitudinal load was applied on the place of traction rods fastened (Fig. 8).

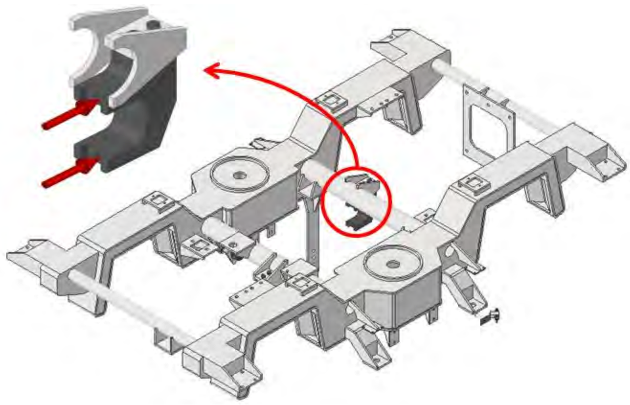

Fig. 8. Assembly of traction rod in the bogie frame [6]

Those rods are attached to the frame central crossbars by additionally screwed parts, so in strength analysis of the frame every longitudinal force was replaced by equivalent bending moment. Bogie frame model mesh consists of tetrahedral solid elements in parabolic order and it's characterized by: number of fine elements 452 077 and number of nodes 872 906. This settings was not changed for all considered load cases also for two additional cases with frame attachments loads. In addition, the calculations did not take into account the strength of the welds in the welded joints in the frame, assuming therefore, that if properly made, these areas will not have worse strength parameters than the original material. Table 6 [6] consists of chosen results of the static analysis. On their base we could observe that stress values slightly exceed safety limit of 200 MPa only in individual calculation nodes (as already mentioned, the yield point of used steel is 355 MPa, which translates into a minimum safety factor of 1.8), and the area of their concentration is the central part of the side-sills. Also bogie frame displacements values are fully acceptable. The biggest displacement was concentrated around attachment points of the secondary suspension, where forces were attached. The exception from this principle were cases, which additionally considered loads resulting from twisted track, where the greatest values of the displacement where concentrated at the ends of side-sills (in which fixed boundary were replaced by rail reaction forces). In the same time stress is concentrated around primary suspension seats, therefore there is need to change calculation model or side-sills construction.

3.2. Attachments loads

Two additional cases in the bogie frame static analysis were considered with forces and moments, which resulted from attachment units work. Case M1 refers to breaking fully loaded vehicle with maximal deceleration by disc brake and track brake systems.

Case M2 refers to hypothetical situation of a speed increase with maximum acceleration in a curved track.

The calculations considered loads (Fig. 9) coming from:

- magnetic track brake – vertical force generated by electromagnet Q_{DHS} and bending moment resulting from friction force between drag shoe and rail M_{HHS1};
- disc brake – bending moment M_{dbu} resulting from multiplication between friction force F_T and distance from that force to reference point R_H;
- gear unit and motor – in case M1 it's gravity force and in case M2 it's gravity force enlarged by dynamic reactions, which result from drive system work;
- anti-roll bar.

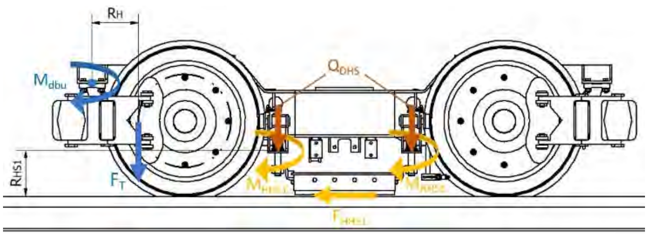

Fig. 9. Frame load from the operation of the braking system [6]

The last load was calculated as follows [4]:

$$F_{anti} = \frac{k_s \cdot \arcsin\frac{L_{anti} \cdot \sin\alpha}{2L}}{L_{anti}\sqrt{1-\left(\frac{L_{anti} \cdot \sin\alpha}{2L}\right)^2}} \text{ [N]} \qquad (14)$$

where: k_s – torsional rigidity of the anti-roll bar [Nm/rad], L_{anti} – length of the torsion bar [m], L – length of the torsion arm [m], α – permissible tilt angle of the car body [°].

The calculation model with applied additional loads is presented in the Fig. 10 (Table 4 and 5 [6]). Obtained results, in a graphic form, are listed in Table 7 [6]. In case M1 stresses are concentrated on a brakes equipment attachments points, especially in the elements of track brake mount that results from relatively large distance between them and frame sidesills. Case M2 shows asymmetrical load of the bogie frame which is a result of only one powered wheelset in the bogie.

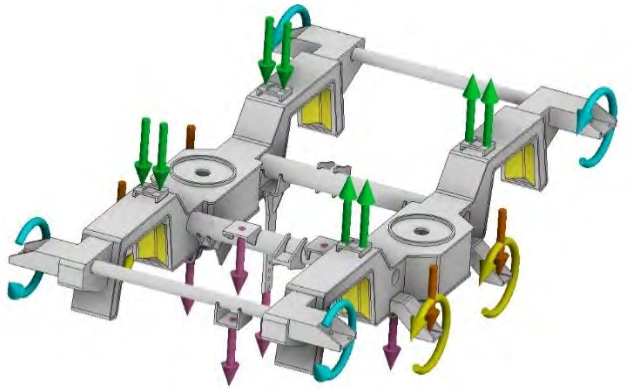

Fig. 10. Loads on the bogie frame attachments [6]

4. Recapitulation

In this article authors focused on the bogie frame and wheelset axle strength analysis, so in the same time description of the whole vehicle was strictly limited, and it can be find in another authors' publications: [7–9]. Aforementioned bogie elements were chosen, because they are crucial for vehicle safety. Generally, obtained stress and displacement values are acceptable, which confirms appropriate construction of inspected parts. Moreover, use of internal frame resulted in bending moments reduction. It is important to state that the authors restrained strength analysis only to static cases. In the further development of the bogie construction dynamic loads and fatigue strength should be taken into account which probably would impose some changes in original structure. Fatigue calculations are especially important when we consider that bogies which use chevron springs in wheelsets guidance, sometimes has problems with fatigue cracking of bogie frame in the area of aforementioned springs. Good example of such situation is 37 AN bogie [13]. In such cases there is a necessity to use additional element which would fasten bogie frame parts from both sides of axlebox. Moreover, the authors didn't exclude the possibility of using one bogie between each section of the vehicle (in such case it would be suspended under four bogies), that would reduce the force value distributed on both elements.

Table 2. Characteristics of steels for wheelset axle

Feature	EA1N	EA4T	30NiCrMoV12
Yield strength [MPa]	320	420	834
Tensile strength [MPa]	550	650	932
Allowable stress on the solid axle body surface [MPa]	200	240	300
Allowable stress on the bore surface of hollow axle [MPa]	80	96	120
Allowable stress on the fitted areas of solid axle [MPa]	120	144	b/d
Allowable stress on the fitted areas of hollow axle [MPa]	110	132	175
Allowable stress on the bearings mounting places of hollow axle [MPa]	94	113	120
Permissible safety factor [–]	1.20	1.33	1.22

Table 3. Results of the strength calculations of the railway axle

No.	Feature	EA1N	EA4T	EA4T (d)	30Ni...(d)
–	Permissible safety factor [–]	1.20	1.33	1.33	1.22
I	Torsional stress [MPa]	38.81	38.81	41.40	41.40
	Bending stress [MPa]	38.93	38.93	41.53	41.53
	Equivalent stress [MPa]	77.68	77.68	82.86	82.86
	Allowable stress [MPa]	120.00	144.00	132.00	175.00
	Actual safety factor [–]	1.54	1.85	1.59	2.11
II	Torsional stress [MPa]	30.53	30.53	31.98	31.98
	Bending stress [MPa]	11.93	11.93	12.50	12.50
	Equivalent stress [MPa]	54.20	54.20	56.78	56.78
	Allowable stress [MPa]	120.00	144.00	113.00	120.00
	Actual safety factor [–]	2.21	2.66	1.99	2.11
III	Torsional stress [MPa]	19.87	19.87	20.39	20.39
	Bending stress [MPa]	25.69	25.69	26.37	26.37
	Equivalent stress [MPa]	42.95	42.95	44.08	44.08
	Allowable stress [MPa]	200.00	240.00	96.00	120.00
	Actual safety factor [–]	4.66	5.59	2.18	2.72
IV	Torsional stress [MPa]	30.53	30.53	31.98	31.98
	Bending stress [MPa]	67.00	67.00	70.18	70.18
	Equivalent stress [MPa]	85.35	85.35	89.40	89.40
	Allowable stress [MPa]	120.00	144.00	113.00	120.00
	Actual safety factor [–]	1.41	1.69	1.26	1.34
V	Torsional stress [MPa]	38.81	38.81	41.40	41.40
	Bending stress [MPa]	77.86	77.86	83.05	83.05
	Equivalent stress [MPa]	102.86	102.86	109.72	109.72
	Allowable stress [MPa]	120.00	144.00	132.00	175.00
	Actual safety factor [–]	1.17	1.40	1.20	1.59

Table 4. Load cases in static analysis

	Case	F_{z1} [N]	F_{z2} [N]	F_y [N]	F_x [N]	T_w [N]
Exceptional loads	N1	131 414	131 414	98 274		
	N2	131 414	131 414	98 274		55 005
	N3	131 414	131 414		30 992	55 005
	N4	131 414	131 414	98 274	30 992	
Service loads	E1	89 109	89 109	75 102		
	E2	89 109	89 109	75 102		55 005
	E3	89 109	89 109		15 974	55 005
	E4	89 109	89 109	75 102	15 974	
	E5	115 842	62 376	75 102		
	E6	115 842	62 376	–75 102		
	E7	80 198	98 020		15 974	
	E8	115 842	80 198			
	E9	62 376	98 020	–75 102		55 005
	E10	80 198	115 842		15 974	55 005
Attachments loads	M1	131 414	131 414			
	M2	89 109	89 109	75 102	15 974	

Table 5. Attachments load cases

	Case	M_{dbu} [Nm]	F_{HS} [N]	M_{HHS1} [Nm]	F_{anti} [N]	F_{p+s} [N]
Attachments loads	M1	5 696	36 000	1 452	97 397	11 978
	M2				97 397	310 000

Table 6. Results of the strength analysis of the bogie frame

<table>
<tr><th></th><th>Von Misses stresses [MPa]</th><th>Displacement [mm]</th></tr>
<tr><td>N1</td><td>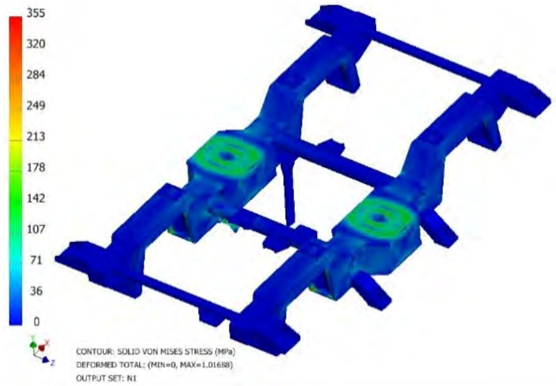
</td><td>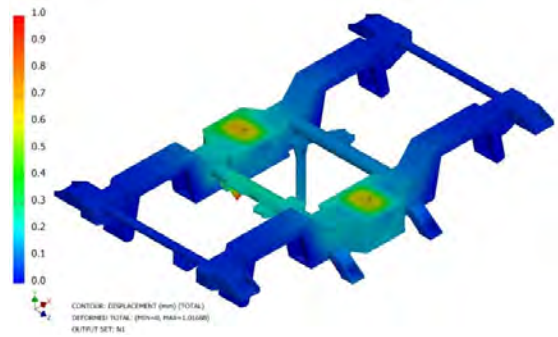
</td></tr>
<tr><td>N2</td><td>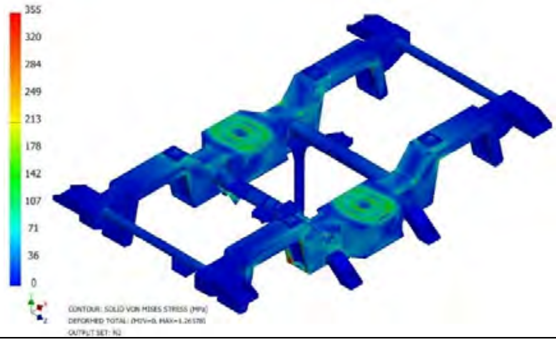
</td><td>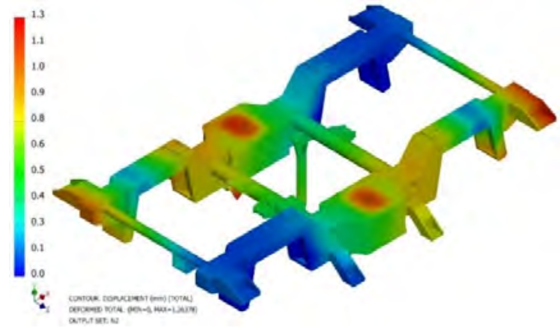
</td></tr>
<tr><td>N3</td><td>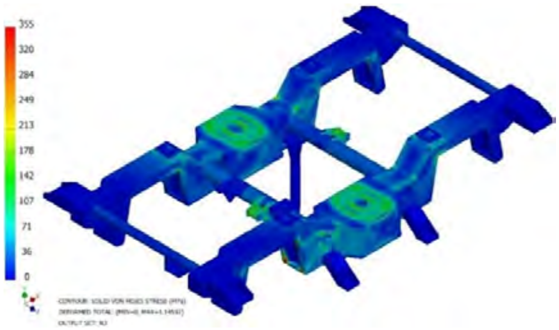
</td><td>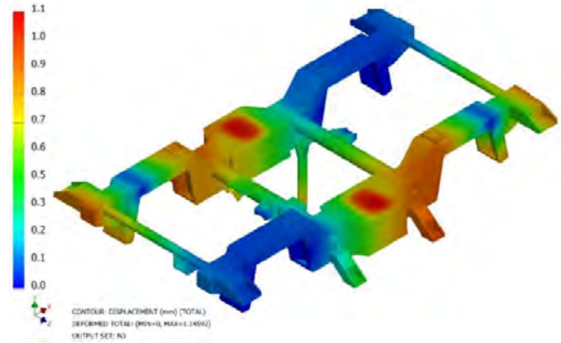
</td></tr>
<tr><td>N4</td><td>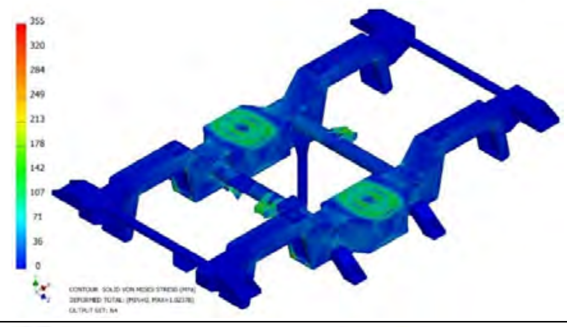
</td><td>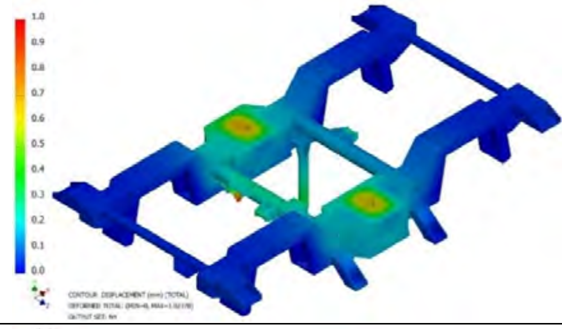
</td></tr>
<tr><td>E5</td><td>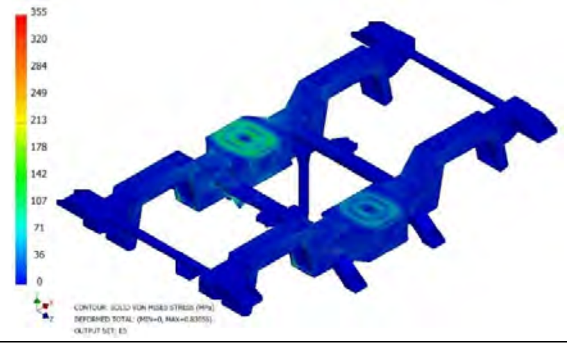
</td><td>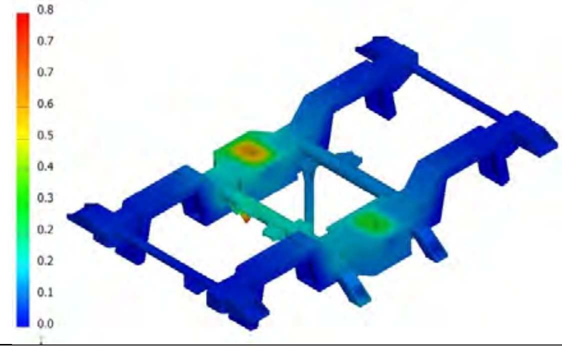
</td></tr>
</table>

Table 7. Results of the strength analysis – cases M1 and M2

	Von Misses stresses [MPa]	Displacement [mm]
M1	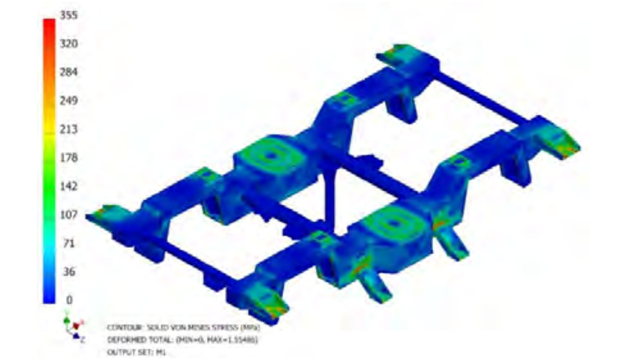	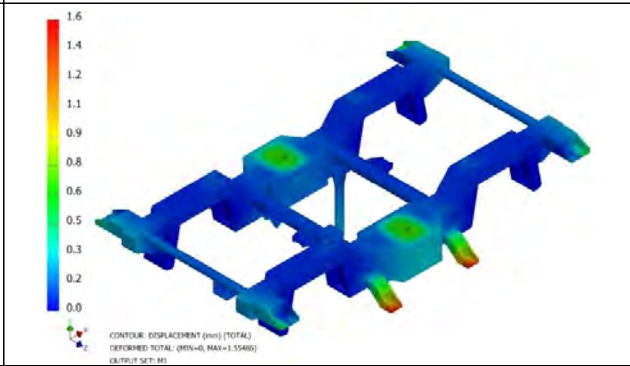
M2	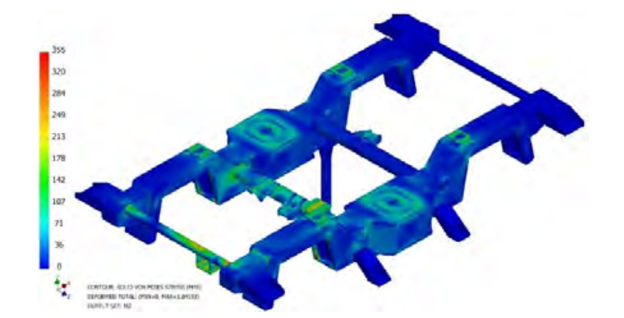	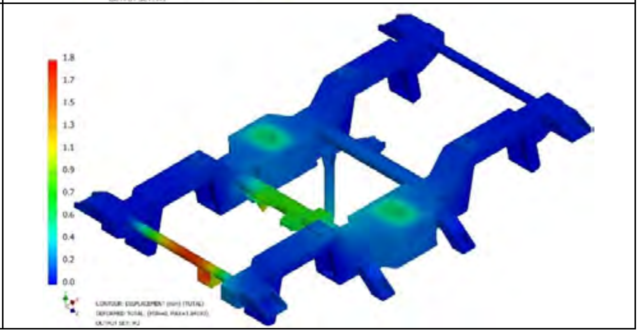

Nomenclature

b distance between axlebox centre plane and the centre of gravity
F_{p+s} load caused by work of population system
F_{anti} force resulting from anti-roll bar
F_x longitudinal forces resulting from service load
F_{xmax} longitudinal forces resulting from exceptional load
F_y transverse forces resulting from service load
F_{ymax} transverse forces resulting from exceptional load
F_{z1} vertical forces caused by suspended mass acceleration, with service load
F_{z1max} vertical forces caused by suspended mass acceleration, with exceptional load
g gravitational acceleration
H horizontal force balancing transverse guiding forces
h_1 distance between wheelset axle and the centre of gravity
k_s torsional rigidity of the anti-roll bar
L length of the torsion arm
L_{anti} length of the torsion bar
M_{dbu} bending moment caused by work of disc brake
M_{HHS1} moment resulting from friction force between drag shoe of magnetic track brake and rail
M_v total mass of empty vehicle
m_p mass of maximal load
m_{pe} mass of real service load
m_1 mass of the vehicle per wheelset axle
m^+ mass of the bogie
n_a number of axles in the bogie
n_b number of bogies in the rolling stock
P_1 vertical force acting on the axlebox, represents empty vehicle
P_2 vertical force acting on the axlebox, represents fully loaded vehicle
Q_1 reaction force acting on the less loaded axlebox
Q_2 reaction force acting on the more loaded axlebox
R wheel rolling radius
s distance between wheel centre plane and the centre of gravity
T_w force resulting from track twist
Y_1 transverse guiding force acting between wheel flange and rail on the side of less loaded axlebox, during motion along a curved track
Y_2 transverse guiding force acting between wheel flange and rail on the side of more loaded axlebox, during motion along a curved track

Bibliography

[1] Bao Y., Li Y., Ding J. A case study of dynamic response analysis and safety assessment for a suspended monorail system. *International Journal of Environmental Research and Public Health*. 2016, 13, 1121. https://doi.org/10.3390/ijerph13111121

[2] Bharadwaj C. Stress analysis of bogie frame structure. *Master thesis. Blekinge Institute of Technology*, Karlskrona 2017. https://www.diva-portal.org/smash/get/diva2:1194122/FULLTEXT03.pdf (accessed on 20.09.2020).

[3] Cai C., He Q., Zhu S. et al. Dynamic interaction of suspension-type monorail vehicle and bridge: numerical simulation and experiment. *Mechanical Systems and Signal Processing*. 2019, 118, 388-407. https://doi.org/10.1016/j.ymssp.2018.08.062

[4] Chen D., Sun S., Li Q. Strength evaluation of a bogie frame by different methods. *Mechanical Engineering Science*. 2019, 1(1), 54-64. https://doi.org/10.33142/me.v1i1.662.

[5] Guo Q., Wang P., Chen J. et al. Dynamic analysis on suspended monorail vehicle passing through turnouts. *IOP Conference Series: Materials Science and Engineering*. 2018, 439, 042078. https://doi.org/10.1088/1757-899X/439/4/042078

[6] Jędrzejewski P., Kuczyk M. Koncepcja wagonu silnikowego kolei podwieszanej. *Master thesis*. Gdańsk 2020.

[7] Kuczyk M., Jędrzejewski P., Załuski P. Evaluation of suspended rail vehicle movement parameters. *Rail Vehicles/Pojazdy Szynowe*. 2021, 3, 20-29. https://doi.org/10.53502/RAIL-143045

[8] Kuczyk M., Jędrzejewski P., Załuski P. The construction of suspended rail vehicle bogie. *Rail Vehicles/Pojazdy Szynowe*. 2021, 4, 1-13. https://doi.org/10.53502/RAIL-144534

[9] Kuczyk M., Jędrzejewski P., Załuski P. The concept of suspended urban rail vehicle. *Rail Vehicles/Pojazdy Szynowe*. 2021, 2, 52-66. https://doi.org/10.53502/RAIL-139982

[10] Mancini G., Cera A. Design of railway bogies in compliance with new EN 13749 European standard. http://www.railway-research.org/IMG/pdf/609.pdf (accessed on 18.09.2020)

[11] Mancni G., Corbizi A., Lombardo F. et al.. Design of railway axle In compliance with the European Norms: high strength alloyed steel compared to standard steel. http://www.railway-research.org/IMG/pdf/617.pdf (accessed on 25.08.2020)

[12] SAFEGE monorail: https://kamakura-enoshima-monorail.jp/fun/index.html (accessed on 05.04.2022)

[13] Safety alerts from 19.02.2016 and 10.06.2016. https://www.utk.gov.pl/pl/monitorowanie/alerty-bezpieczenstwa/alerty-bezpieczenstwa-o-1/6988,Alerty-bezpieczenstwa-opublikowane-w-2016-roku.html (accessed on: 20.10.2020)

[14] Schwebebahn: https://schwebebahn.de/en/ (accessed on 05.04.2022)

[15] Sobaś M. Analytical determination of load capacity of the freight wagon wheelset axle with axle journal dimensions ϕ120×179 mm. *Rail Vehicles/Pojazdy Szynowe*. 2019, 3, 48-59. https://doi.org/10.53502/RAIL-138539

[16] Sobaś M. Badania wytrzymałościowe wózka 11 ANC. *Rail Vehicles/Pojazdy Szynowe*. 2010, 2, 31-41. https://doi.org/10.53502/RAIL-139720

Article citation info:
Urbański P., Gallas D., Stachowicz A. et al. Analysis of the selection of the auxiliary drive system for a special purpose hybrid rail vehicle. *Rail Vehicles/Pojazdy Szynowe*. 2022, 1-2, 30-39. https://doi.org/10.53502/RAIL-149405

Rail Vehicles/Pojazdy Szynowe

www.railvehicles.eu

Analysis of the selection of the auxiliary drive system for a special purpose hybrid rail vehicle

Patryk **Urbański** [a, *], Dawid **Gallas** [a], Arkadiusz **Stachowicz** [b], Wojciech **Jakuszko** [a], Paweł **Stobnicki** [a]

[a] *Łukasiewicz Research Network – Poznan Institute of Technology, Poland*
[b] *Zakład Pojazdów Szynowych Sp. z o.o., Poland*

ARTICLE INFO

Received: 7 March 2022
Revised: 7 April 2022
Accepted: 23 April 2022
Available online: 3 May 2022

KEYWORDS

special purpose vehicle
alternative propulsion systems
hybrid rail vehicle
auxiliary drive system

Strict emission standards mean that the internal combustion engines used in means of transport must meet the standards for the emission of harmful compounds. For this reason, there is an increase in the use of alternative sources of propulsion, including rail transport. The article presents unconventional solutions of drive systems in rail vehicles using hybrid systems and fuel cells. The concept of the realizing project of a special-purpose rail vehicle, which is to be able to be driven from three different sources, was presented. Considerations concerning the selection of the internal combustion propulsion system, which is to be used as an auxiliary in the vehicle, are described. The possibilities of installing the power unit on the vehicle were also presented.

1. Introduction

The rolling stock comes in many forms and is designed for numerous tasks, which are often highly specific and different from those of other vehicles. These differences result in a significant divergence in the operating characteristics and parameters of these vehicles. This significantly complicates the selection of key components and assemblies, which are limited by their specific range of work and parameters. The main aspect that determines a new vehicle design is the drive system and its components. Thus, the criteria for selecting drive units and their parameters depend on the type of work expected to be carried out by the designed vehicle. For example, a passenger rail vehicle will typically be significantly different from a freight or shunting locomotive. Special-purpose vehicles often require all the more specific and unique characteristics and parameters. Depending on the operating conditions, the use of rail vehicles with electric drives may not be possible, mainly due to the limited level of electrification of railway lines in Poland, estimated at over 60% [10]. As a result of these limitations, along with the need to reduce exhaust emissions and the demand for hydrocarbon fuels on the market of rail vehicles, new alternative or mixed solutions are emerging, based on electric supply from electrified lines, with the possibility of driving and operating the vehicle outside the reach of catenary for a limited period of time or without such limitations. Such solutions allow to reduce the need for rail vehicles to operate powered by the combustion engine. This means that it is possible to use the internal combustion engine only when it is necessary or in an emergency. Another solution is to incorporate vehicles with alternative drives into a larger consist in order to reduce its environmental impact. Such an effect can be obtained by using the alternative propulsion actively when the internal combustion engine reaches operating points with low efficiency or high emissivity. Another approach is to use batteries or other energy storage systems that allow the vehicle to temporarily operate on the non-electrified lines. However, this solution does not allow the vehicles to be fully independent from electrified railway lines. All the discussed solutions are intended to replace the

* Corresponding author: patryk.urbanski@pit.lukasiewicz.gov.pl (P. Urbański)

existing technologies of rail vehicles propulsion, which usually require electric traction or pose a health risk to people in their vicinity through the emission of toxic compounds in the exhaust gases.

The negative impact on the environment and the growing awareness of the problems related to the emission of carbon dioxide and other toxic compounds influencing global warming results in the development of new, more ecological technologies in all branches of transport. The results of this development can mainly be observed in road vehicles, but it is possible to use similar solutions in rail vehicles as well, provided appropriate adaptations are made. As the estimated age of the rolling stock is high, especially in Poland, where it is around 33 years for locomotives [1] changes in the drive system technology of these vehicles will be reflected by a gradual reduction of exhaust emissions. This means that in order to achieve notable reduction in exhaust emissions from rail vehicles, changes to the rolling stock available on the market have to be introduced well in advance. While the environmental performance of the vehicles purchased over the last two decades were characterized by better environmental indicators (in line with the tightened legal requirements for exhaust emissions), they will still have a negative impact on the environment, which will continue until they are withdrawn from service and decommissioned. The necessity to replace the vehicles in use currently with modern rolling stock leads to the development of new, less environmentally harmful solutions for vehicle drive technology, including special-purpose vehicle propulsion systems, which are discussed in this article.

2. Examples of alternative drive systems in modern rail vehicles

2.1. Hybrid drive systems

Hybrid drive systems are more commonly associated with road vehicles. Popularity of the electrification [21] of transport means is increasing due to its ability to limit the negative impact on the natural environment by reducing the operation time share of the internal combustion engine. This trend can also be found, to a lesser extent, in the non-road vehicle sector [14], as well as in rail transport [25].

About 62% of Polish Railway Lines are electrified, and in five voivodeships this share does not exceed 40% [20]. In the case of the EU-27 countries, this average is 56% [11]. As a result it is not possible to use rail vehicles that depend only on the overhead contact line in all sections for power. In this case, it is reasonable to use vehicles with their own propulsion source, such as an internal combustion engine. However, the use of this solution is associated with the inevitable local emission of harmful exhaust compounds. A rail vehicle with a hybrid drive system is a solution that combines the advantages of using the overhead contact line, where available, and the independence of the diesel powered drive system.

Rail vehicles designs with hybrid drive systems have already been developed in Poland. One of them is a passenger railcar designed by Łukasiewicz Research Network – Rail Vehicles Institute “TABOR” and produced by H. Cegielski-FPS. The 227M vehicle is a design consisting of two segments: combustion and electric (Fig. 1 and Fig. 2). Each segment is specially designed for the use of a specific drive system type, i.e. in the combustion segment there are two power generators that enable driving in the combustion mode (Fig. 3) [8], and in the electric segment devices necessary for the collection and processing of electric energy from overhead electric traction. Table 1 shows the 227M vehicle technical parameters.

Table 1. The technical parameters of the 227M vehicle

Parameter	Value
Length of the entire multiple unit	53 100 mm
Total empty vehicle mass	110 t
Total mass of the vehicle at full passenger capacity (4 persons/m^2)	127 t
Number of seats: fixed/foldable	80/3
Number of standing places (4 persons/m^2)	145
Vehicle speed when powered from the overhead catenary	160 km/h
Vehicle speed when powered by on-board power generators	120 km/h
Combustion engines power	2 × 400 kW@1900 rpm
Combustion engines max. torque	2 × 2500 Nm@1200 rpm
Power of electric motors	4 × 300 kW

Fig. 1. Type 227M rail vehicle consisting of two segments: diesel and electric [28]

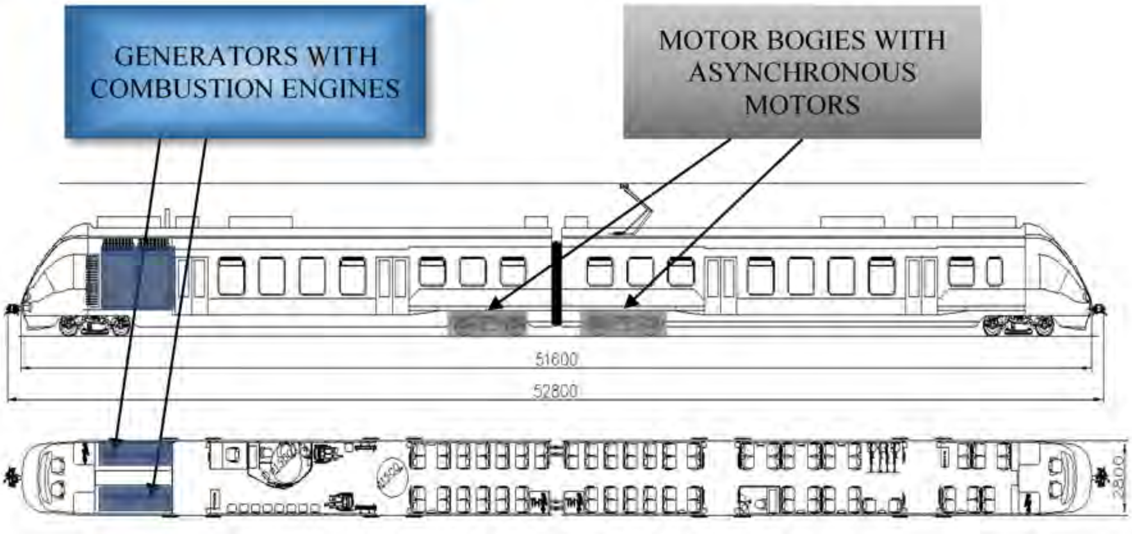

Fig. 2. Location of generating sets and motor bogies [8]

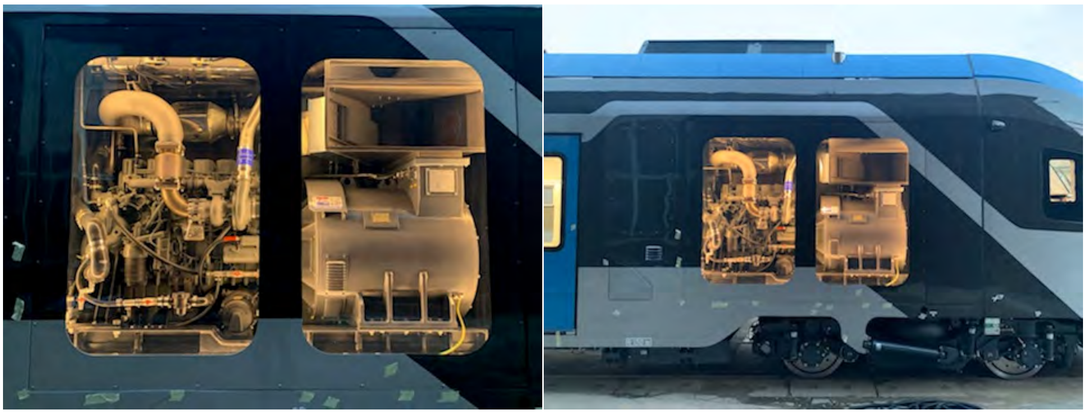

Fig. 3. Built-in powerpack generator in the type 227M rail vehicle [8]

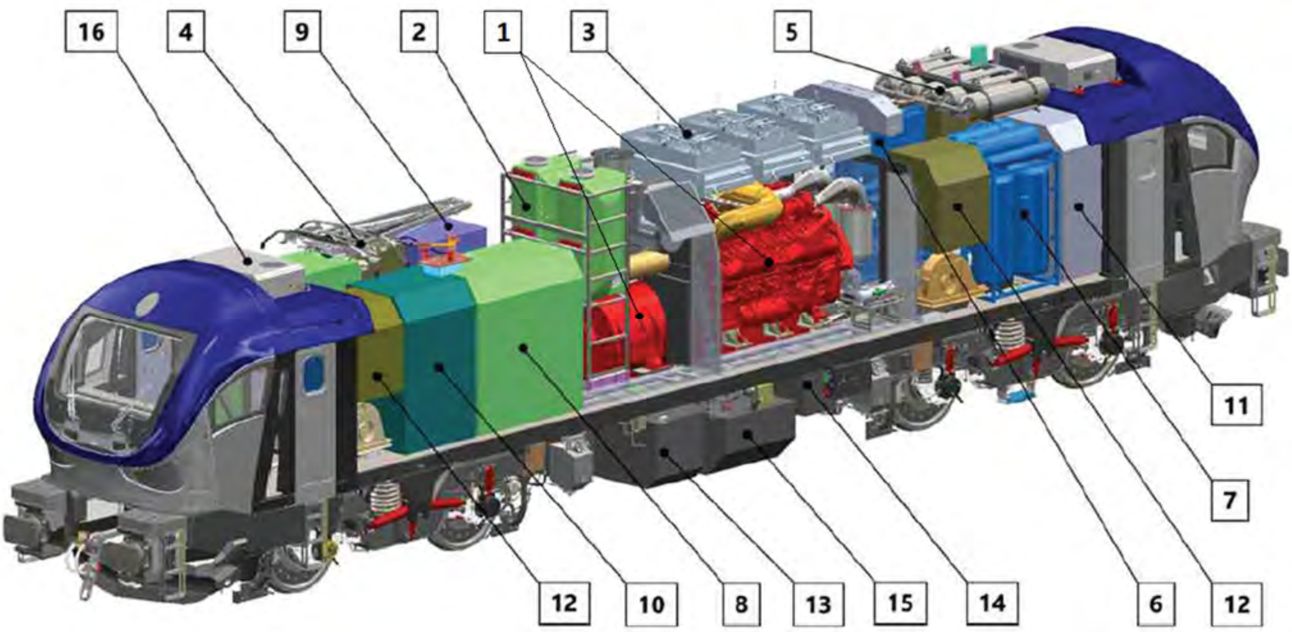

Fig. 4. Layout of equipment on the 111DE locomotive, 1 – power generator, 2 – a set of SCR catalytic systems, 3 – combustion engine cooling unit, 4 – pantograph, 5 – main air tanks, 6 – compressor module, 7 – board module, 8 – power inverters cabinet, 9 – cooling column with braking resistor, 10 – HV cabinet, 11 – ETCS cabinet, 12 – LV cabinet with electric motors ventilator, 13 – line choke, 14 – battery box, 15 – fuel tank, 16 – air conditioning unit [19]

Another example of rail vehicles that can use two power sources for propulsion are the double-drive locomotives type 111DE (Fig. 4) and 111Ed (Fig. 5), designed by Łukasiewicz Research Network – Rail Vehicles Institute "TABOR" , and manufactured by Rail Vehicles PESA Bydgoszcz S.A. [3]. Depending on their type, these vehicles can use two drive systems: one powered from the overhead catenary and one powered by a power generator. This solution makes the four-axle locomotive universal. The vehicle can be used on any section of the railway line, whether it is electrified or not. In addition, such a vehicle is highly versatile as it can perform various transport tasks in freight and passenger traffic as well as shunting work where the lines are not electrified. Vehicles of this type are dedicated especially to Undertakings involved in intermodal transport and dispersed goods transport [19].

Fig. 5. Type 111Ed locomotive [12]

2.2. Fuel cells

Hydrogen is one of the most promising forms of energy storage and production. It is an environmentally friendly solution due to its usage having close to zero emissivity. Contrary to the combustion of hydrocarbon fuels, where the combustion products, in addition to steam and heat of combustion, include such harmful compounds as: CO_2, CO, HC, NO_x as well as particulate matter (PM) [4, 17], the combustion of hydrogen result in the production of water vapor [26, 27] and when the temperature is high enough also the formation of NO_x compounds. Hydrogen can also be used in fuel cells, the so-called Fuel Cell Hydrogen (FCH) [5, 24]. In this case, the products of the chemical reaction are just water vapor, heat and electricity, which is then used to drive electric motors [9]. Ultimately, hydrogen is considered the future application for these types of solutions. According to estimates, replacing trains equipped with CI engines operating on the Gdynia-Hel-Gdynia section with trains powered by hydrogen fuel cells, where the hydrogen is produced from renewable energy sources, could reduce the annual CO_2 emissions from this service by 2505 tons [23].

Fuel cells are already used in rail transport [16, 22]. One of the most recognizable implementations of hydrogen cells in rail vehicles is the Alstom Coradia iLint vehicle (Fig. 6). The train was used commercially for the first time in September 2018. At the same time, these vehicles replaced the combustion vehicles used so far on the 100 km route running through Cuxhaven, Bremerhaven, Bremervörde and Buxtehude in Lower Saxony, Germany [6]. Coradia iLint vehicle data and parameters is shown in Table 2.

Fig. 6. Coradia iLint [6]

Table 2. Main parameters of the Coradia iLint [9]

Parameter	Value
Max travel speed	140 km/h
Range at full tank	1000 km
Service mass of a single segment	49 t
Hydrogen tanks volume	94 kg

In Poland, the project concerning hydrogen drive for rail vehicles was undertaken by the Bydgoszcz manufacturer of rail vehicles PESA [7]. Work is currently underway on a hydrogen-powered shunting locomotive, and more precisely, the modernization and adaptation of the SM42 locomotive to a hydrogen powered drive system. After the works are completed, the locomotive is to receive the designation SM42 6Dn (Fig. 7). Basic vehicle data was presented in Table 3.

Table 3. Operating parameters of the SM42 6Dn hydrogen shunting locomotive [9]

Parameter	Value
Max. speed	90 km/h
Service mass	< 70 t
Fuel cell power	85 kW × 2
Expected fuel consumption	< 0.08 kg/kWh
DC voltage supply	< 800 V
Battery capacity	> 160 kWh
Hydrogen tanks capacity	175 kg
Operating temperature range of the fuel cell	–40°C to +85°C

Fig. 7. The hydrogen locomotive SM42 6Dn and hydrogen fuel cells powering it produced by PESA Bydgoszcz presented at the International Railway Fair TRAKO 2021 [9]

Projects concerning the use of fuel cells in shunting locomotives have also been appearing abroad. An example is the conceptual project of the MaK G1206 diesel shunting locomotive conversion into an FCH locomotive (Fig. 8). The project team calculated the necessary parameters for the vehicle drive and energy storage systems, which included components such as a battery energy storage, a fuel cell system, a cooling system for both batteries and fuel cells, and a hydrogen tank. The paper also presents the calculations of energy demand and data on components for the discussed drive system ensuring that at least three heavy shunting tasks can be performed (Table 4). The weight of the entire new drive system was 9900 kg and its total volume was 16.5 dm^3 [15].

Table 4. Component layout for the most demanding profile combination (3× heavy shunting) [15]

Component	Designation	Quantity	Installation size
Fuel cell	Hydrogenics HD 30	18	540 kW
Fuel cell cooler	AKG W40	18	780 kW
Battery	Akasol 18 AKM 46	10	368 kWh
Battery cooler	Technotrans zeta.line 450	1	45 kW
Hydrogen tank	Luxfer W320H	13	100 kg

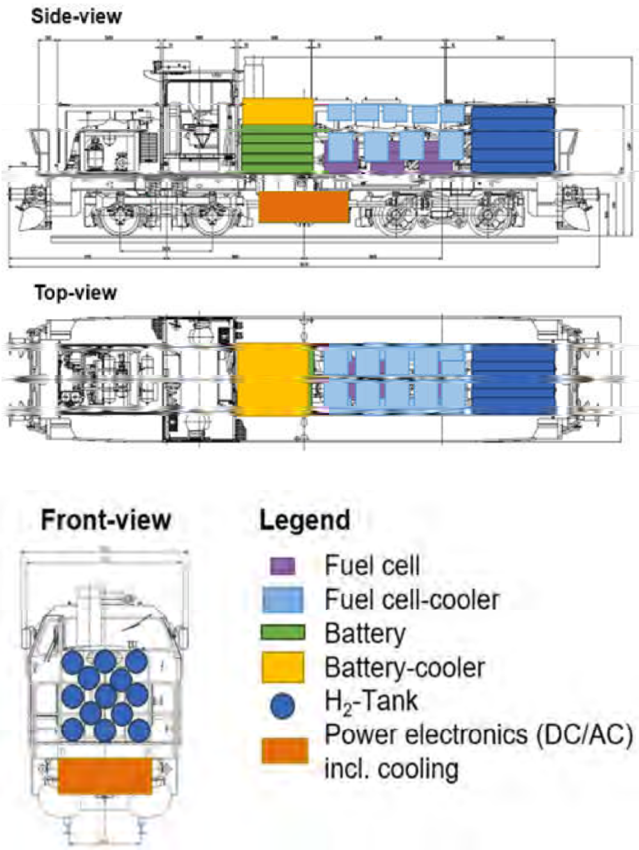

Fig. 8. Arrangement of the components on a MaK G1206 locomotive [15]

3. Special purpose rail vehicle

The development of sustainable transport in Poland plays an major role in the steps taken towards improved environmental protection. Therefore, ZPS LLC (Railway Vehicle Plant), together with Łukasiewicz Research Network – Rail Vehicles Institute "TABOR" (now Łukasiewicz – Poznań Institute of Technology, Center of Rail Vehicles) are implementing a project as a part of the Fast Track competition entitled "An innovative, special railway vehicle with a hybrid drive, equipped with energy storage systems, as vehicle base for the assembly of devices intended for the construction, diagnostics and measurements of railway infrastructure", project no. POIR.01.01.01-00-1601/20 concerning the construction of a new, innovative special railway vehicle with a type 501EH hybrid drive system. The vehicle will be equipped with elements such as a crane with workman basket and basket platform, a workshop compartment and a social compartment (Fig. 9). The most important challenges for an environmentally friendly special purpose vehicle include:

– designing the vehicle's powered bogies adapted to the travel speed of 160 km/h,
– hybrid drive system,

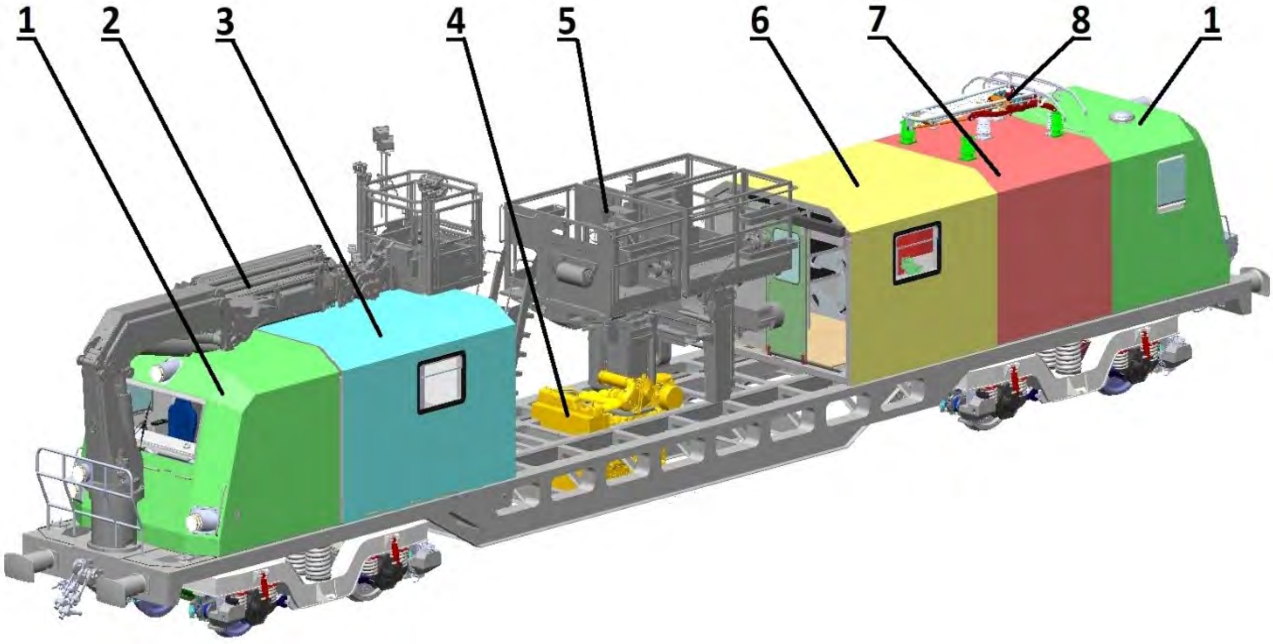

Fig. 9. The initial concept schematic of a 501EH special purpose vehicle; 1 – driver's cabin, 2 – cherry picker basket and arm, 3 – crew rest compartment, 4 – combustion engine, 5 – cherry picker platform, 6 – workshop compartment, 7 – electrical module, 8 – pantograph

- implementation of new, environmentally friendly systems for processing and storage of electricity, such as battery energy storage,
- reduction of harmful exhaust compounds emissions,
- modern and intuitive driver's interface.

One of the more interesting design developments is the new hybrid powertrain. Ultimately, in conventional travel conditions, i.e. driving on electrified sections, the vehicle will draw electric power from the traction network through a pantograph. Upon arrival at the place of work, the vehicle shall be capable of operating using energy from its energy storage devices. The selection of the energy storage system with the required operational parameters will take place at further stages of the project, however, the use of modern battery stacks or supercapacitors would be considered. These solutions would also allow the use of a braking energy recovery system. This would increase the overall energy efficiency of the vehicle in operation. During braking, the generated electricity would go to the energy storage system, and should the system capacity be full, the energy would be sent back to the traction network.

The rolling stock vehicles that serve technical support and maintenance roles are typically powered exclusively by compression-ignition (CI) combustion engines. The use of such a vehicle to carry out stationary works leads to the emission of toxic compounds such as HC, CO, NO_x as well as particulate matter (PM) from the combustion of hydrocarbon fuels in the area where it is located, which in turn increases the health risk of employees working in that area and has a negative impact on the local environment. For this reason, the vehicle described in the article will be equipped with an internal combustion engine, the main task of which will be to power the vehicle in emergency situations, i.e. failure of the primary power supply (electric traction and energy storage). During the failure, the engine will work together with the generator as a power generator.

The selection of an appropriate combustion engine was one of the key stages of the vehicle design process. This article presents only preliminary considerations for the engine selection, based on the engine units used in previous projects. The actual engine units will be selected at a later stage through tendering. The article gives consideration to drive units used in vehicles designed by the ZPS company in the past based on the previously obtained experience in engine selection. Due to the nature of the vehicle's operation, its weight, available space for equipment and the vehicle's demand for power during combustion mode – based on the experience of the rolling stock manufacturer, among other things, which was gained during the implementation of previous projects – two internal combustion engines of an American engine manufacturer Caterpillar were taken into account. More precisely, they were the C9.3B and C13B engines. The design of the two engines is similar, both are four-stroke inline six-cylinder units. The difference results mainly from the displacement volume, and thus the performance (Table 5). The most important differences are the engine nominal power and torque values. The C9.3B engine reaches 340 kW of maximum power and a torque of 2,088 Nm, while the C13B, which is larger by 3.2 dm^3, achieves a power output of 430 kW and a torque of 2,640 Nm.

Table 5. Technical parameters for CAT C9.3B and CAT C13B engines [2]

Parameter	C9.3B	C13B	Unit
Engine configuration	6 In-line, 4-stroke engine	6 In-line, 4-stroke engine	[-]
Bore	115	130	[mm]
Stroke	149	157	[mm]
Displacement	9.3	12.5	[dm^3]
Aspiration	Turbocharged-Aftercooled (TA)	Turbocharged-Aftercooled (TA)	[-]
Engine power	340@2000	430@1800–2100	[kW@rpm]
Peak torque	2088@1400	2640@1400	[Nm@rpm]
Compression ratio	17:1	15.8:1	[-]
Fuel type	Diesel	Diesel	[-]
Ignition type	Compression Ignition	Compression Ignition	[-]
Max operating altitude	2240	2037	[m]
Combustion system	Direct Injection	Direct Injection	[-]
Turbo configuration	Single	Single	[-]
Turbo quantity	1	1	[-]
Exhaust emission standard	Stage V/Tier 4	Stage V/Tier 4	[-]

The difference in the swept volume between the engines also affects their dimensions and mass. The C13B engine is notably bigger and 260 kg heavier than the C9.3B (Table 6). It should be remembered that an internal combustion engine also requires a cooling, lubrication and exhaust aftertreatment systems. The larger the engine, the more efficient and bulky the supporting systems need to be.

Table 6. Dimensions of CAT C9.3B and CAT C13B engines [2]

Parameter	C9.3B	C13B	Unit
Height	1068	1134	[mm]
Length	1125	1274	[mm]
Width	791	994	[mm]
Weight – Net Dry – Basic Operating Engine Without Optional Attachments	865	1125	[kg]

For Non-Road Mobile Machinery (NRMM) vehicles, which also include rail vehicles, the latest emissions standard in Europe is Stage V [13]. The considered engines belong in the non-road engines (NRE) group, which are dedicated to be mounted into NRMM vehicles. In the certification process, these units are required to pass the Non-Road Stationary Cycle (NRSC) and Non-Road Transient Cycle (NRTC) exhaust emissions tests, and the specific emission for the relevant harmful compound must not exceed the legal limit. These engines can provide a maximum power of 340 kW and 430 kW respectively, which places them in the NRE-v/c-6 category. The emission limits for Stage V engines were shown in Table 7.

Meeting the increasingly demanding exhaust emission limits often necessitates the use of exhaust aftertreatment systems (ATS). In order to meet the latest exhaust emission norm for proposed engines – Stage V – it was necessary to use a complex exhaust aftertreatment system consisting of a set of catalytic converters and particulate filters. The following elements were used for both engines:

- an diesel oxidation catalytic reactor (DOC), which helps reduce the exhaust emission of selected toxic compounds through their oxidation. This reactor can oxidize the following exhaust compounds: $HC \rightarrow CO_2 + H_2O$, $CO \rightarrow CO_2$ and $NO \rightarrow NO_2$,
- a diesel particulate filter (DPF), which helps reduce the exhaust emission of particulate matter (PM) by oxidizing the particles,

Table 7. Stage V emission norms for non-road engines (NRE) [13]

Category	Ign.	Net Power	Date	CO	HC	NOx	PM	PN
		kW		g/kWh				1/kWh
NRE-v/c-1	CI	P < 8	2019	8.00	7.50[a,c]		0.40[b]	-
NRE-v/c-2	CI	8 ≤ P < 19	2019	6.60	7.50[a,c]		0.40	-
NRE-v/c-3	CI	19 ≤ P < 37	2019	5.00	4.70[a,c]		0.015	1×10^{12}
NRE-v/c-4	CI	37 ≤ P < 56	2019	5.00	4.70[a,c]		0.015	1×10^{12}
NRE-v/c-5	All	56 ≤ P < 130	2020	5.00	0.19[c]	0.40	0.015	1×10^{12}
NRE-v/c-6	All	130 ≤ P ≤ 560	2019	3.50	0.19[c]	0.40	0.015	1×10^{12}
NRE-v/c-7	All	P > 560	2019	3.50	0.19[d]	3.50	0.045	-

[a] HC+NOx
[b] 0.60 for hand-startable, air-cooled direct injection engines
[c] A = 1.10 for gas engines
[d] A = 6.00 for gas engines

– selective catalytic reduction (SCR) reactor, which reduces NO_x emissions by injecting 32.5% urea solution into the exhaust gas [18].

In order to effectively use a well designed and developed exhaust aftertreatment system a significant amount of free space is needed in the vehicle for its installation and mounting. Table 8 presents the size dimensions of the whole sets of exhaust aftertreatment systems designed for the CAT C9.3B and C13B engines, in order to allow them to meet the current exhaust emission norms.

Table 8. Exhaust aftertreatment systems for CAT C9.3B and CAT C13B engines [2]

Parameter	C9.3B	C13B	Unit
Aftertreatment systems in a set	DOC + DPF + SCR	DOC + DPF + SCR	[-]
Height	432	460	[mm]
Length	925	896	[mm]
Width	694	807	[mm]
Mass	96	100	[kg]

The engine unit, along with the supporting systems mentioned above, requires adequate space on the vehicle for its placement. Therefore, making the right choice when selecting the engine unit to use for the vehicle is a key part of the vehicle design phase, especially when noting the extra space needed on the rail vehicle to install other systems needed by the engine assembly. On the other hand, the engine should have enough power to enable smooth operation along with having some power reserve. Figure 10 is a comparison of the CAT C9.3B and C13B engines, and Fig. 11 shows their dimensions including all the attached systems.

A special-purpose vehicle is ultimately to be equipped with devices intended for repair and maintenance operations. For this reason, the space that can be used for compartments on the vehicle's undercarriage frame is very limited. This also applies for the selection of a combustion engine and all its support systems as well as a generator. One of the solutions for placing the generator set, which has already been used in other vehicle designs, was the use of space in the structure of the undercarriage. These types of structures make it possible to utilize the unused space, to lower the center of gravity of the vehicle, and to allow for more ergonomic placement of parts, devices and compartments on the undercarriage. Such a solution also significantly increases the available space for the placement and mounting of the main engine and generator systems, i.e. the systems related to electric traction and energy storage, including electrical cabinets, e.g. a high-voltage cabinet, where it was more accessible. It should also be noted that the described vehicle will only use the internal combustion engine in emergencies, by which it is meant that its use will be occasional. An example of the aforementioned design solution on another vehicle was provided in Fig. 12.

4. Conclusions

The presented theoretical analysis of the engine unit selection in a special-purpose vehicle with a 501EH hybrid drive system was determined on the basis of multiple parameters. Among the most significant of those were the engine operating parameters, i.e. its characteristics, power and torque, as well as the

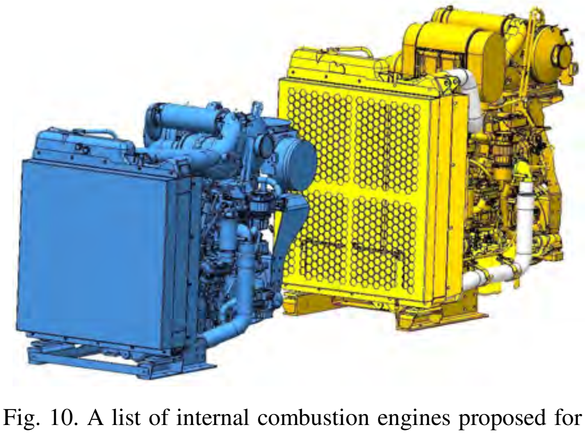

Fig. 10. A list of internal combustion engines proposed for installation on the 501EH vehicle. Blue color CAT C9.3B engine, yellow color CAT C13B

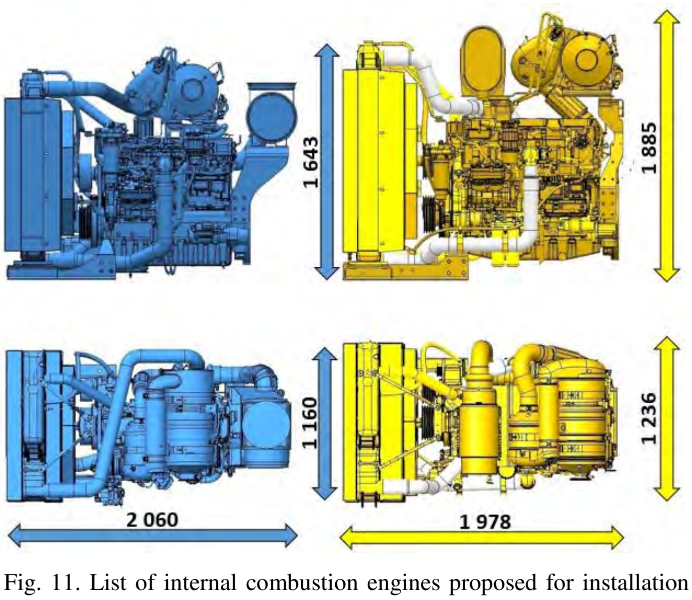

Fig. 11. List of internal combustion engines proposed for installation on the 501EH vehicle with dimensions provided. Top image shows the side view, bottom image shows the top view. Blue color CAT C9.3B engine, yellow color CAT C13B

Fig. 12. An example of a CAT engine mounted in the free undercarriage space of a different type special purpose rail vehicle

parameters and operating conditions of the vehicle itself based on its expected operations, including vehicle ergonomics, reliability and stability. Due to the space limitations associated with using a larger, more powerful engine, which required larger and more efficient supporting systems and components, including the exhaust aftertreatment system, it was necessary to use modern design and production methods, as well as modern materials and technologies in the presented analysis.

It should be noted that the internal combustion engine in the discussed vehicle concept was assigned the role of a backup or emergency power supply, which is why its frequent use was not considered. Hence, aspects such as the reliability and efficiency of the engine unit were taken into account to a limited extent. Changes to the hybrid drive design were expected to achieve measurable environmental gains, such as lower exhaust emissions and lower environmental impact. As a result, it was possible to avoid more invasive changes and overcomplicating the drive system, which can further improve the servicing and maintenance of the vehicle. Depending on the customer requirements regarding such vehicles, the solutions used may be subject to change.

Acknowledgements

The article was written in connection with the project entitled "An innovative special hybrid drive rail vehicle improved with independent power storage designed to transport equipment for building, diagnosing and measuring of rail infrastructure". The project is implemented under Sub-measure 1.1.1 Industrial research and development works carried out by enterprises, co-financed by the European Regional Development Fund.

European Funds Smart Growth
Republic of Poland
The National Centre for Research and Development
European Union European Regional Development Fund

Nomenclature

ATS	aftertreatment systems
CO	carbon monoxide
CO_2	carbon dioxide
DOC	diesel oxidation catalyst
DPF	diesel particulate filter
FCH	fuel cell hydrogen
H_2	hydrogen
H_2O	water
HC	hydrocarbons
NO_x	nitrogen oxides
NRE	non-road engine
NRMM	non-road mobile machinery
NRSC	non-road stationary cycle
NRTC	non-road transient cycle
PM	particulate matters
SCR	selective catalytic reduction
TA	turbocharged-aftercooled

Bibliography

[1] Bartczak K. Analiza taboru kolejowego w Polsce. *TTS Technika Transportu Szynowego*. 2015, **22**.

[2] Caterpillar materials.

[3] Czerwiński J., Marciniak Z. Modułowe konstrukcje jedno- i dwukabinowych lokomotyw elektrycznych i spalinowych. *Rail Vehicles/Pojazdy Szynowe*. 2014, **1**, 1-10. https://doi.org/10.53502/RAIL-138806

[4] Daszkiewicz P., Rymaniak Ł., Medwid M. et al. Assessment of toxic compounds emission of rail-road tractor during works on tracks. *Rail Vehicles/Pojazdy Szynowe*. 2018, **4**, 1-8. https://doi.org/10.53502/RAIL-138518

[5] Doyle D., Harris A., Chege S. et al. Hydrogen fuel cell buses: modelling and analysing suitability from an operational and environmental perspective. *SAE Technical Paper* 2020-01-1172. https://doi.org/10.4271/2020-01-1172

[6] Durzyński Z. Hydrogen-powered drives of the rail vehicles (part 1). *Rail Vehicles/Pojazdy Szynowe*. 2021, **2**, 29-40. https://doi.org/10.53502/RAIL-139980

[7] Durzyński Z. Hydrogen-powered drives of the rail vehicles (part 2). *Rail Vehicles/Pojazdy Szynowe*. 2021, **3**, 1-11. https://doi.org/10.53502/RAIL-142694

[8] Far M., Gallas D., Urbański P. et al. Modern combustion-electric PowerPack drive system design solutions for a hybrid two-unit rail vehicle. *Combustion Engines*. 2021. https://doi.org/10.19206/CE-144724

[9] Gallas D., Stobnicki P. Adoption of modern hydrogen technologies in rail transport. *Journal of Ecological Engineering*. 2022, **23**(3) 84-91. https://doi.org/10.12911/22998993/145291

[10] Internet website: European Commission: „Mobility and Transport", 2016. https://ec.europa.eu (accessed on 14.02.2022).

[11] Internet website: Electrified rail network in Europe, by country. https://www.statista.com (accessed on 11.02. 2022).

[12] Internet website: Pesa walczy o kontrakt na lokomotywy. https://bydgoszcz.wyborcza.pl (accessed on 15. 02.2022).

[13] Internet website: Emission standards, EU: Nonroad Engines. https://dieselnet.com (accessed on 18.02. 2022).

[14] Kalociński T. Modern trends in development of alternative powertrain systems for non-road machinery. *Combustion Engines*. 2022, **188**(1), 42-54. https://doi.org/10.19206/CE-141358

[15] Konrad M., Jäger V., Pagenkopf J. et al. Concept and design of a shunting locomotive equipped with a hybridized fuel cell hydrogen powertrain. *2021 Sixteenth International Conference on Ecological Vehicles and Renewable Energies* (EVER). 2021, 1-5. https://doi.org/10.1109/EVER52347.2021.9456623

[16] Madovi O., Hoffrichter A., Little N. et al. Feasibility of hydrogen fuel cell technology for railway intercity services: a case study for the Piedmont in North Carolina. *Railway Engineering Science*. 2021, **29**(3), 258-270. https://doi.org/10.1007/s40534-021-00249-8

[17] Merkisz J., Rymaniak Ł., Lijewski P. et al. Tests of ecological indicators of two-way vehicles meeting Stage IIIB and Stage IV standards in real operating conditions. *Rail Vehicles/Pojazdy Szynowe*. 2020, **1**, 1-9. https://doi.org/10.53502/RAIL-138495

[18] Merkisz J., Siedlecki M., Ziółkowski A. et al. Methods of reducing emission from HDV Euro VI engines. *Combustion Engines*. 2015, **162**(3), 480-486.

[19] Michalak P., Jakuszko W. Innowacyjna uniwersalna lokomotywa dwunapędowa. *Zeszyty Naukowo-Techniczne Stowarzyszenia Inżynierów i Techników Komunikacji w Krakowie. Seria: Materiały Konferencyjne*. 2019, **2**(119), 149-158.

[20] Michalak P., Merkisz J., Stawecki W. et al. The selection of the engine unit – main engine generator during the modernization of the 19D/TEM2 locomotive. *Combustion Engines*. 2020, **182**(3), 38-46. https://doi.org/10.19206/CE-2020-307

[21] Muelaner J.E. Unsettled issues in electrical demand for automotive electrification pathways. *SAE Research Report* EPR2021004, 2021. https://doi.org/10.4271/EPR2021004

[22] Oldknow K., Mulligan K., McTaggart-Cowan G. The trajectory of hybrid and hydrogen technologies in North American heavy haul operations. *Railway Engineering Science*. 2021, **29**(3), 233-247. https://doi.org/10.1007/s40534-021-00242-1

[23] Orczyk M., Gis W., Tomaszewski F. Circumstances of railway transport hydrogenization in Poland. *SAE Technical Paper* 2020-01-2131, 2020. https://doi.org/10.4271/2020-01-2131

[24] Pertl P., Aggarwal M., Trattner A. et al. Development of hydrogen powered fuel cell e-snowmobiles. *SAE Technical Paper* 2019-32-0555, 2019.

[25] Rasiński T., Michnej M. Application of hybrid drives in diesel locomotives. *Rail Vehicles/Pojazdy Szynowe*. 2019, **1**, 18-25. https://doi.org/10.53502/RAIL-138503

[26] Shadidi B., Najafi G., Yusaf T. A review of hydrogen as a fuel in internal combustion engines. *Energies*. 2021, **14**(19), 6209. https://doi.org/10.3390/en14196209

[27] Sun Y., Anwar M., Hassan N.M.S. et al. A review of hydrogen technologies and engineering solutions for railway vehicle design and operations. *Railway Engineering Science*. 2021, **29**(3), 212-232. https://doi.org/10.1007/s40534-021-00257-8

[28] Urbański P., Gallas D., Kołodziejek D. et al. Passive safety features of a type 227M rail vehicle. *Rail Vehicles/Pojazdy Szynowe*. 2021, **4**, 25-36. https://doi.org/10.53502/RAIL-144978

Article citation info:
Miklasz R., Dawid S., Wojtukiewicz P. et al. Bogie design of 227M type rail vehicle. *Rail Vehicles/Pojazdy Szynowe*. 2022, 1-2, 40-48.
https://doi.org/10.53502/RAIL-150309

Rail Vehicles/Pojazdy Szynowe

www.railvehicles.eu

Bogie design of 227M type rail vehicle

Radosław **Miklasz** [a, *], Szymon **Dawid** [a], Paweł **Wojtukiewicz** [a], Marek **Grzegórski** [a]

[a] *Łukasiewicz Research Network – Poznań Institute of Technology, Center of Rail Vehicles, Poland*

ARTICLE INFO

Received: 9 March 2022
Revised: 15 April 2022
Accepted: 21 May 2022
Available online: 23 May 2022

KEYWORDS

interoperability
bogie
dual drive rail vehicle
link arm
running gear system

The article presents the running parameters and construction of the 41MN and 46MN hybrid traction units (HZT). Design solutions were presented and described, attention was paid to the functions fulfilled by individual systems of rolling and driving bogies.The article was created as part of an ongoing project as part of Program Badań Stosowanych 3 Umowa Nr PBS3/B6/26/2015 „Lekki autobus szynowy do ruchu regionalnego".

1. Introduction

One of the design goals assigned to the 227M vehicle is to meet the TSI (Technical Specifications for Interoperability) specifications for the vehicle. The designed 41MN and 46AN running gear systems, in order to comply with the TSI, have to meet specific requirements, which include:

1. environmental requirements
   – working temperature zone, humidity acc. to EN 50125-1
   – pollution resistance
2. interaction of the vehicle on the track
   – track gauge (EN-15273-2)
   – axle load (determined by the category of the railway line)
   – running gear parameters affecting trackside equipment (EN-15437-2)
   – dynamic behavior of the vehicle on the track [6]
     • safety against derailment EN 14363[10]
     • running dynamics EN 14363
     • vehicle running safety EN 14363
     • track load EN 14363
     • equivalent conicity
     • wheel profile parameters [8, 9]
     • the service life of the wheelset [7]
3. running gears systems
   – bogie frame (EN-13749)
   – parameters of wheelsets EN 13103, EN 13104
   – wheel profile geometry EN 13979:1
   – minimum curve radius of the track
   – positioning the rail scrapers above the rail head
4. brakes
   – braking performance – emergency and service braking, heat loads, parking brake EN 15431-1, EN 15431-6
   – adhesion index – adhesion coefficient depending on the type of vehicle, anti-skid systems – EN 15595
   – brakes independent of adhesion force UIC 541-06
   – requirements for brakes in the event of an emergency.

Two types of bogies have been designed for the needs of the 227M (FPS PLUS) vehicle:

– 41MN – motor bogie, with subtypes 41MNa and 41MNb differing in the arrangement of sensors on the bearing housings and, consequently, in the arrangement of electric wires (Fig. 1)
– 46AN – rolling bogie, with the subtypes 46ANa and 46ANb, differing in the arrangement of sensors on the bearing housings and, consequently, in the arrangement of electric wires. They are located on the edge of the vehicle (Fig. 2).

* Corresponding author: szymon.dawid@pit.lukasiewicz.gov.pl (S. Dawid)

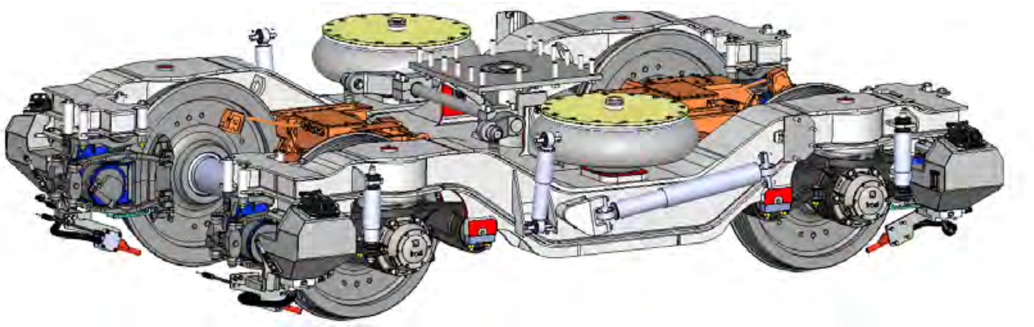

Fig. 1. Driving bogie type 41MN

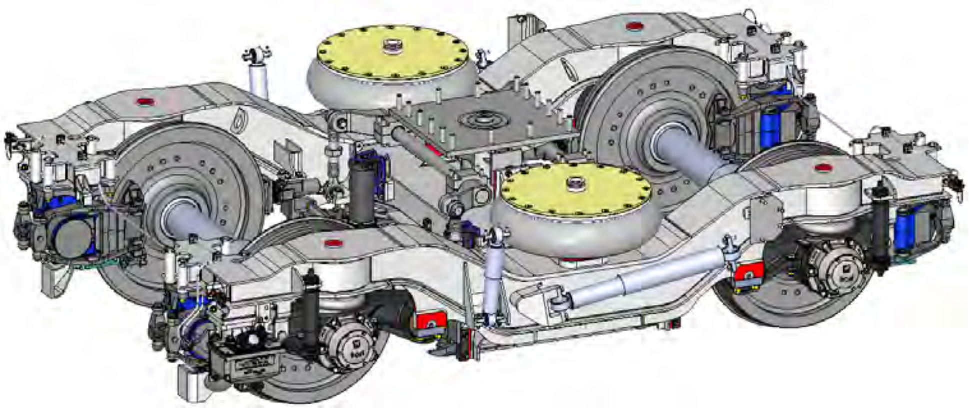

Fig. 2. Rolling bogie type 46AN

Table 1. Basic parameters of 44MN/46AN bogies

Parameter	46AN rolling bogie	41MN motor bogie
Design speed of the vehicle	176 km/h	
Track gauge	1435 mm	
Wheelbase of wheelsets (bogie base)	2500 mm	
Wheel diameter (new/ worn)	ϕ850/ϕ780 mm	
Vehicle weight (empty)	~100 000 kg	
Bogie weight	7.05 t ±3%	9.2 t ±3%
Engine power	–	2 × 300 kW
Gear ratio	–	5.98
Maximum load of a wheelset on the track	18 t	
Wheel rim width	135 ±1 mm	
Maximum permissible wear of the brake block	30 mm	
Maximum permitted wear of the brake disc	7 mm	
Permissible radial wheel wear	35 mm	
Center distance of wheelset axial bearings	2100 mm	
Axial bearing	TBU130 × 230 × 160	
Primary suspension bumper clearance (vertical)	40 mm (+Z) 30 mm (–Z)	
Secondary suspension bumper clearance (vertical)	64 mm	
Lateral movement of the bogie in relation to the body of the vehicle	50 mm	
Minimum permitted radius of track curve	150 m	
The maximum steering angle of the bogie in new condition	4º40’	
Largest lateral movement of a wheelset relative to the bogie frame (per side)	3 mm	
Axle journal dimensions:	ϕ130 × 217mm	
Brake:	disc brake mounted on a wheel (pneumatic-mechanical); rail brake; parking brake	disc brake mounted on a wheel (pneumatic-mechanical); parking brake
Additional equipment	lubrication of the wheel flanges together with the reservoir cleaning brake block	heated sandblasting nozzles and sand tanks cleaning brake block
Bogie gauge	according to the UIC-505-1 (p. 5.2) card	

The bogies are characterized by good running properties in terms of safety and driving comfort, minimized wear of the running surface of the wheels, maintenance-free nature of the operation of individual components and simple design. The basic parameters of the bogies are presented in Table 1.

2. Bogie design

2.1. Bogie frame

The frame of the bogies is a spatial, open-type welded structure that has been unified as much as possible so that the differences between the rolling bogie and the motor bogie are insignificant. The frame consists of two longitudinal side beams connected by a crossbar and four small end beams. All its elements are made of S355J2 + N low-alloy structural steel with increased strength, which chemical composition is presented in Table 2.

Table 1. Chemical composition of S355J2 + N steel

C	0,2
Mn	1.5
Si	0.2–0.5
P	≤ 0.04
S	≤ 0.04
Cr	≤ 0.3
Ni	≤ 0.3
Mo	–
W	–
V	–
Al	≤ 0.02
Cu	≤0.03

All beams form a closed box structure. In the central part of each side beam, an air spring support is welded on its upper flange. On each of the side beams there are vertical shock absorbers and link-arm mounts. End beams located at the ends of each side beams act as a brackets for the installation of sandblast nozzles or supports for the scraper and the wheel flange lubrication system. The brackets for the brake caliper mechanisms are located on the end beams as well. On the crossbar there are supports for the drive system, bumpers, horizontal shock absorber and the tractive force transmission system. The differences between the types relate to the presence of the drive system and the rail brake. Figure 3 shows:

- gray – common frame structure elements for both types
- red – frame structure elements present only on the motor bogie (propulsion suspension brackets)
- green – frame structure elements present only on the rolling bogie (rail brake suspension brackets and its longitudinal buffers).

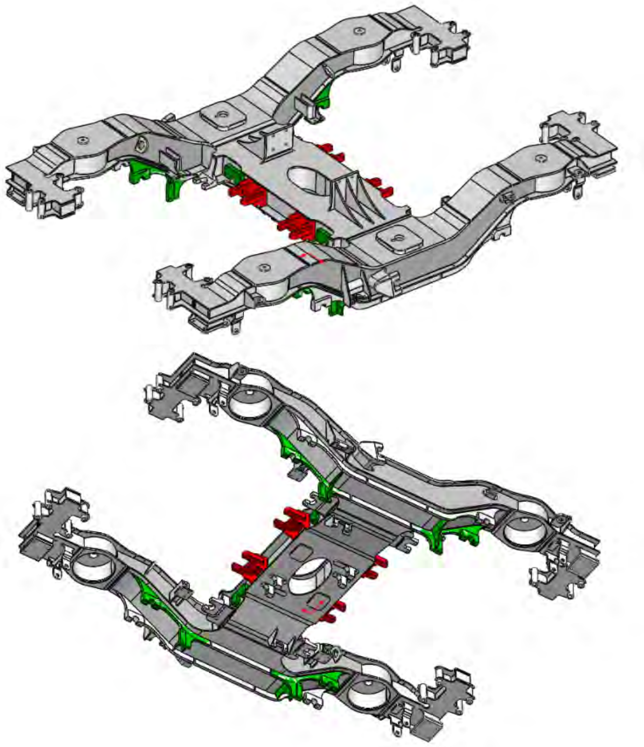

Fig. 3. Complete bogie frame with brackets

2.2. Wheelset

Each bogie is equipped with two forged and rolled wheelsets with rimless wheels with a rolling circle diameter of ϕ850 mm in new condition and the wheel outline S1002/h28/e32.5/6.7% in accordance with PN-EN 13715:2008. The permissible diameter of the wheel when worn is ø780 mm. The rimless wheel is adapted to the installation of brake discs. The wheelsets of the motor bogies have been adapted to the installation of axle gears (Fig. 4).

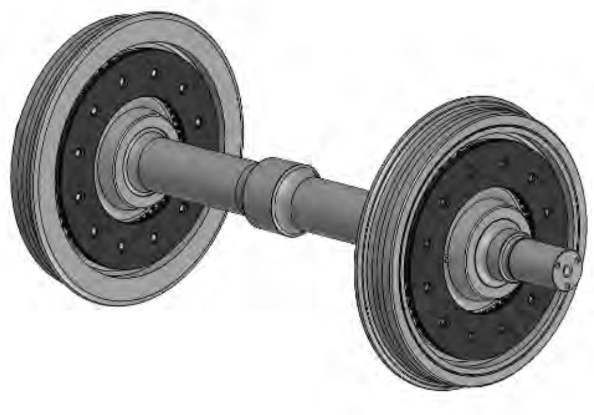

Fig. 4. Isometric view of the wheelset of the motor bogie

2.3. Wheelset steering and primary suspension

The wheelset is guided in the bogie frame by means of two casted link-arms consisting of three parts (three-piece design), i.e. the upper part, lower clamp and bearing housing. Castings are common to both types of bogies (rolling and motor). The link-arm is connected to the bogie frame through a rubber-metal joint (Fig. 5) manufactured by Contitech, the stiffness of which is shown in Table 3.

Table 2. The stiffness of the rubber-metal joint

Stiffness	Stiffness value
radial in the X axis	21.2 kN/mm ±14%
axial in the Y axis	25.2 kN/mm ±14%
radial in the Z axis	3.7 kN/mm ±20%
cardanic about the X axis	660 Nm/grad ±13%
torsion about the Y axis	250 Nm/grad ±15%
cardanic about the Z axis	2770 Nm/grad ±15%

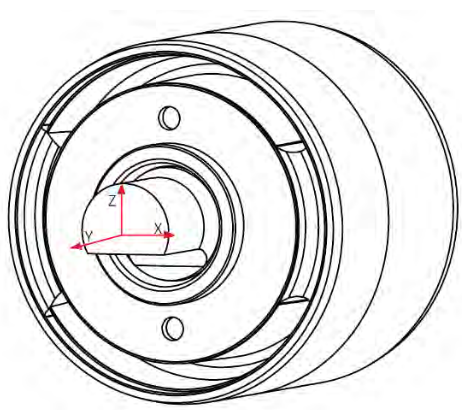

Fig. 5. Isometric view of a rubber-metal joint

The transfer of vertical forces is performed by a set of three coil springs (Fig. 6). The use of as many as three springs results from the necessity to ensure safety against derailment for a wide range of vehicle loads and a small amount of space available for the installation of the springs. The springs are made of 52CrMoV4 + HH spring steel in accordance with the PN-EN 10089 standard.

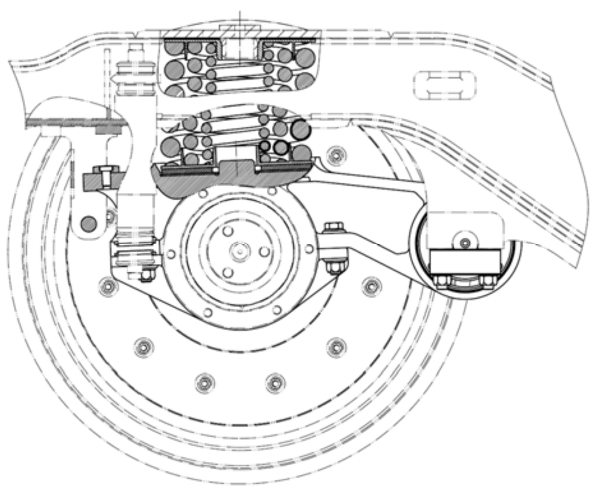
Fig. 6. Primary suspension of 41MN and 46AN bogies

The required distance between the bogie frame and the rail head is achieved by the use of adjustment washers, which are placed on the upper guiding spacer. The springs stand on the lower metal-rubber spacer, which not only serves as a spring guiding element, but also compensates for the non-parallelism of the bases resulting from the work of the link-arm (reduces the buckling tendency of springs) and act as a counter-current insulation. The properties of the primary suspension and the wheelset steering of 41MN/46AN bogies are presented in Table 4.

Table 3. Properties of the primary suspension and the wheelset driving on bogies type 41MN and 46AN

Parameter	Unit	Value	
		41MN	46AN
Diameter of outer/middle/ inner spring bar	mm	38/28/19.5	38.5/29/20
Pitch diameter of outer/ middle/inner spring	mm	255/176/ 112.5	255.5/175/ 113
Total number of turns of outer/middle/inner spring	–	4.9/6.5/9.3	5/6.5/9.2
Number of active turns for outer/middle/inner spring	–	3.4/5/7.8	3.5/5/7.7
Length of outer/middle/inner spring unloaded	mm	309/309/309	318/310/ 314
The length of the springs under receiving load P_0	mm	236	236
Height of the springs loaded to the maximum	mm	196	200
Deflection of outer/middle/ inner spring loaded at maximum	mm	113/113/ 113	118/110/ 114
Compliance of the outer/ middle/inner spring	mm/kN	2.76/4.52/ 7.78	2.67/3.82/ 7.08
Primary suspension springing stiffness for empty/ loaded conditions	kN/mm	1.12/1.16	1.21/1.25
Damping force of a vertical damper at V = 0.1 m/s (tension/compression)	kN	0.55/0.45	
Damping force of the vertical damper at V = 0.3 m/s	kN	1.1	
Maximum cross movement of the wheelset relative to the bogie (per side)	mm	3	

Vibration is damped by a vertical hydraulic shock absorber. Limiting the vertical movement of the wheelset is realized in the form of a metal bumper installed between the link-arm and the frame, and a pin preventing the wheelset from falling onto the track while lifting the bogie. These limiters also protect the drive system against damage resulting from excessive displacements.

2.4. Secondary suspension

The secondary suspension (Fig. 7) consists of two sets of air springs with rubber-metal springs of the emergency body support. The springs carry out lateral movement and rotation of the bogie in relation to the car body. The power supply and pneumatic spring control system is built on the body of the vehicle. The constant height of the springs, irrespective of the load, is maintained by weighing valves installed on the vehicle's frame and articulated with the bogie frame. Adjusting the height of the vehicle body from the rail head is possible through the use of adjustment washers under the rubber-metal springs of the emergency backrest. The maximum load of one set of springs is 170 kN with a supply pressure of 5.8 bar.

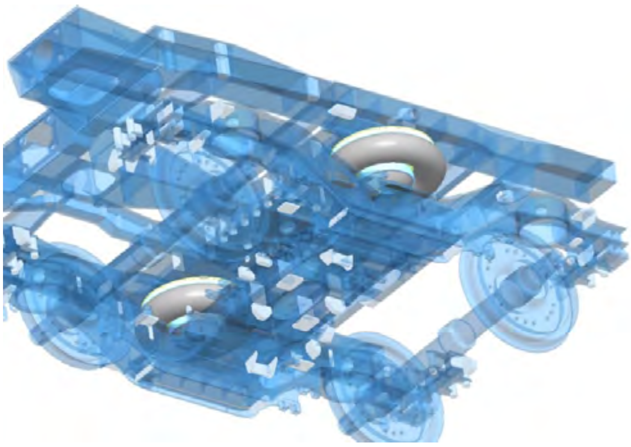

Fig. 7. Secondary suspension assembly for 41MN and 46AN bogies

2.5. Drive system

The bogie drive system (Fig. 8) consists of two sets: traction motor – diaphragm clutch on the motor side – gear mounted on the bogie frame: on one side it is mounted by a gear wheel and a bearing and suspension system by means of a flexible segment coupling on the wheel set axle, on the other sides attached by rubber-metal elements to brackets welded to the frame of the bogie.

The traction motor is a 3-phase asynchronous motor with a squirrel cage rotor designed for operation with a frequency converter. The motor is equipped with rotational speed sensors and with Pt100 thermometric sensors for temperature measurement of the stator windings (temperature setting values: warning 170°C, disconnection 180°C). The traction motor has external cooling. Cooling air is supplied from the vehicle by a corrugated bellows and discharged from the engine through ventilation grids. The basic parameters of the traction motor are shown in Table 5.

The traction motor is flange-mounted directly to the gearbox, thus no motor bearing is needed on the gearbox side. The rotor shaft is connected to the transmission input shaft by a flexible diaphragm coupling. There is a sliding roller bearing on the gear side. The traction motor with the transmission is suspended on the trolley of the vehicle by means of rubber-metal connectors.

The basic parameters of the traction gear are shown in Table 6.

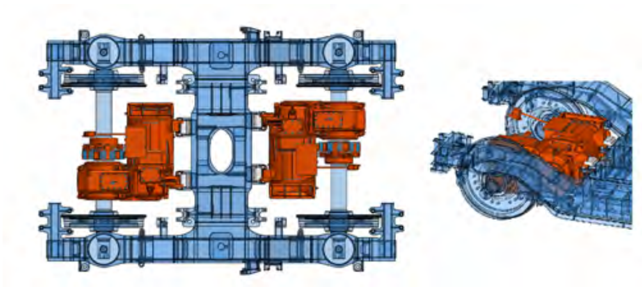

Fig. 8. Drive system of the 41MN bogie

Table 5. Basic parameters of the traction motor

Parameter	Unit	Value
Operating mode	–	S1
Power	kW	300
Voltage	V	2340
Current	A	96
Rotation speed	min^{-1}	2139
Frequency	Hz	72
Efficiency	%	94.3
Power factor cos φ	–	0.82
Torque	Nm	1339
Moment of inertia of the rotor mass	kgm^2	2.1
Weight	kg	engine without accessories – 629 diaphragm clutch – 31 rotor – 191
Insulation	–	VPI impregnation, thermal class 200 according to IEC 349

Table 6. Basic parameters of the traction gear

Parameter	Unit	Value
Type of transmission	–	two-stage
Gear ratio	–	5.98
Maximum rotation speed	min^{-1}	6570
Maximum transmittable torque	Nm	2846
Weight	kg	580 (gear with clutch) 85 (clutch only)

2.6. Traction force transmission

The longitudinal and transverse forces between the body and the bogie are transferred by means of a torsion pin bolted to the vehicle frame and then through the lower part of the towing device assembly to the bogie frame (Fig. 9). The towing apparatus unit is built on the steering pin on tapered roller bearings. Forces are transferred to the frame by means of two parallel guides with ball joints. In the longitudinal direction, the connection is backlash-free. In the transverse direction, after exhausting the allowed free play, the assembly cooperates with the rubber-metal bumpers. If it is necessary to lift the car body with the bogie after exhausting the vertical play between the bogie frame and the towing unit, the bogie is lifted through the pivot pin with the towing device assembly.

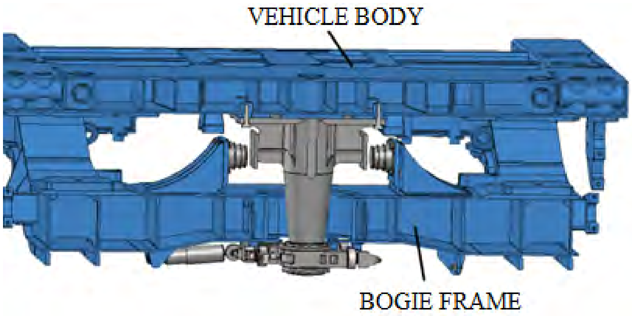

Fig. 9. System of transmission of tractive force in bogies type 41MN and 46AN

2.7. Brake actuators on bogies

The 227M vehicle for which the motor and rolling bogies have been designed is equipped with the following types of brakes mounted on the bogies:

- electrodynamic brake (ED) using the braking force from shifting the traction motor to generator operation - acting on the driving bogie
- direct type electro-pneumatic brake (EP-B)
- pneumatic combined brake (PN)
- a system of blocks that clean the rolling surfaces of the wheels, improving traction (KC)
- electromagnetic friction rail brake (Mg) –mounted on a rolling bogie
- parking spring brake (PS) – mounted on a trolley.

Two ϕ680/390 × 135 mm brake discs are mounted on each axle of the vehicle. The brake disc consists of two friction rings, called internal or external, depending on their position in relation to the wheel rim. The friction ring thickness and the number and geometry of the cooling fins are designed to keep the friction ring temperature within the acceptable range and minimize thermal and mechanical loads. In addition to heat dissipation, the cooling fins also support the friction ring on the wheel. Brake discs mounted on the wheels of the vehicle provide greater braking power compared to the classic solution consisting in the installation of the disc on the axle. It is directly related to the larger dimensions of the disc, which enable obtaining large friction radii.

Each axle of the vehicle is equipped with two brake calipers. Two types are used, the first has only an air brake cylinder, the second has an air brake cylinder and a spring brake cylinder. The compressed air pressure creates the braking force in the air brake cylinder. A "low" force spring serves to loosen the clamp when the pressure is released. In the spring brake cylinder, the braking force is generated by a "large" spring force. Applying compressed air creates a counter force. When the pressure is exceeded, the spring brake caliper is completely released. Each brake caliper is equipped with a stroke adjuster to minimize wear on the brake linings. The vehicle uses JURID 878 organic brake linings in accordance with UIC requirements – 200 cm^2 (400 cm^2 two halves) with a nominal thickness of 35 mm. In the vicinity of each wheel, pneumatic blocks are installed to clean the wheel tread from possible stickers, ensuring the optimal wheel-rail friction coefficient.

All elements of the braking system are controlled and powered from appropriate pneumatic panels. The actuators of the brake installed on the 41MN/46AN bogies are shown in red in Fig. 10.

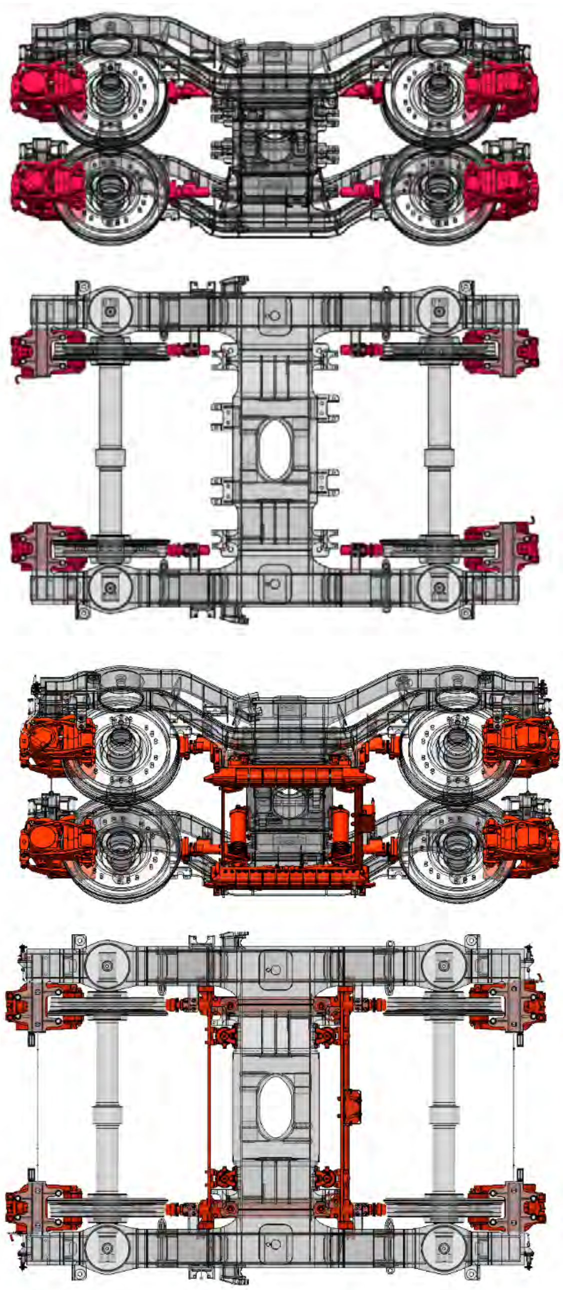

Fig. 10. Braking system of the 41MN type bogie (above) and the 46AN type bogie (below)

2.8. Anti-roll bar

The anti-roll bar is an element connecting the bogie frame with the vehicle body. It consists of a tube connected to the arms and adjustable levers attached to the vehicle's underframe. The torsional stiffness of the stabilizer is 1.5 MNm/rad. The levers have articulated ends enabling the stabilizer to rotate in relation to the trolley. The shape of the stabilizer arms allows for its collision-free operation when the body is fully turned in relation to the bogie.

Each of the bogies is equipped with two anti-roll bars. The use of this in the vehicle reduces the roll coefficient of the body and ensures the correct fit of the pantograph to the vehicle gauge by increasing the angular stiffness of the suspension. Its use allows to maintain the aforementioned coefficient of body roll in the range of $S \leq 0.4$. The simulation tests carried out showed that the coefficient value was 0.36 in the loaded state and 0.25 in the empty state. The installation of the tilt stabilizers is shown in Fig. 11.

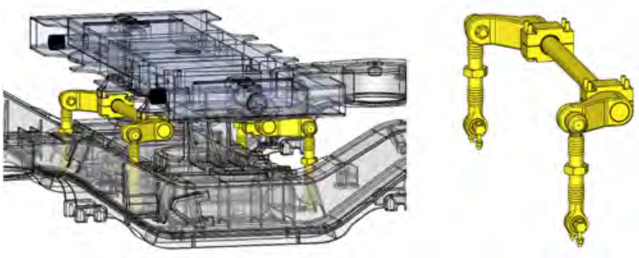

Fig. 11. Body anti-roll bar

2.9. Axle bearing housing arrangement

Axle bearing housings perform several functions:

- they are a housing for axial bearings, in the presented bogies, maintenance-free sealed bearings of TBU type are used,
- they are the mounting of the wheelset through the rocker arms to the frame of the bogie,
- devices and sensors responsible for the safety and driving of the vehicle are fixed to the front of the bearing housing body.

All axial bearing housings (Fig. 12) are equipped with temperature sensors. Each axle of the wheelset in the driving and rolling bogies has one axle bearing housing equipped with a grounding device (stiffening brush), in addition, one axle box on the axle has a built-in sensor for the anti-skid brake system, the other axle bearing housings are equipped, depending on the needs: with sensors for ETCS system and speedometer transmitter for the recorder.

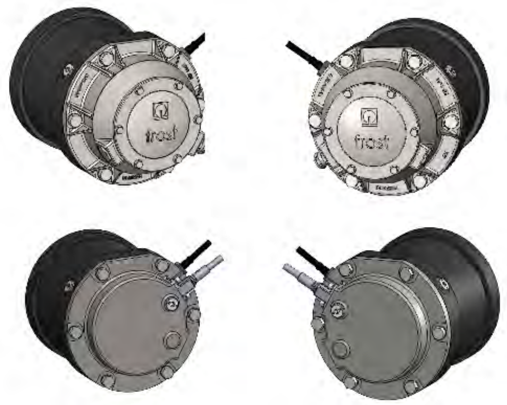

Fig. 12. Axle bearing housings

2.10. Elements of additional equipment

- Flange lubrication system

The vehicle is equipped with an oil lubrication system for the rims of the wheelsets supplied by the DELIMON company, shown in Fig. 13. The system is built on the rolling bogie wheels – the extreme ends of the vehicle. The trailing axle of the end bogies has nozzles on both the left and right side. Lubrication only takes place on the trailing axles in the direction of travel. The system has a sensor for the rotation of the trolley in relation to the box, therefore, when driving in a curve, additional lubrication of the wheel flanges may be activated. Each end bogie has an individual lubricant reservoir with a capacity of 6.5 liters. A plunger metering pump is mounted at the bottom of the tank.

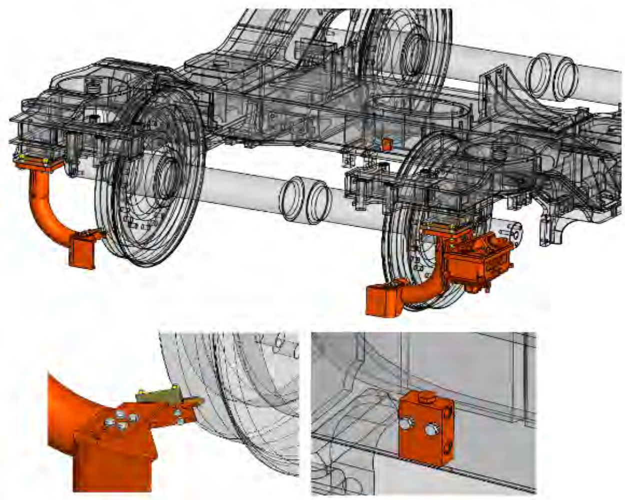

Fig. 13. Flange lubrication system of the 46AN bogie

- Sandblasting system

The vehicle is equipped with sandboxes of the SD1 type (Fig. 14). Each wheel of the driving bogie has a separate sand tank, which is heated by a heater with a thermostat. From each sandbox there is a flexible pipe leading the sand into the immediate vicinity of the wheel-rail contact with the use of a nozzle. The sandbox nozzles are also electrically heated. During normal vehicle operation, the sanders are activated automatically when a slip is detected when braking or starting. The amount of sand discharged from the sandbox depends on the value of the given pressure. The pressure value at the regulator outlet is determined in such a way as to ensure the amount of sand poured out at the level of 400 + 100 g/30 s of work. A sight glass is built into the sandbox reservoirs to assess the sand level. Additionally, the system has a sand level sensor informing the driver about the low sand level.

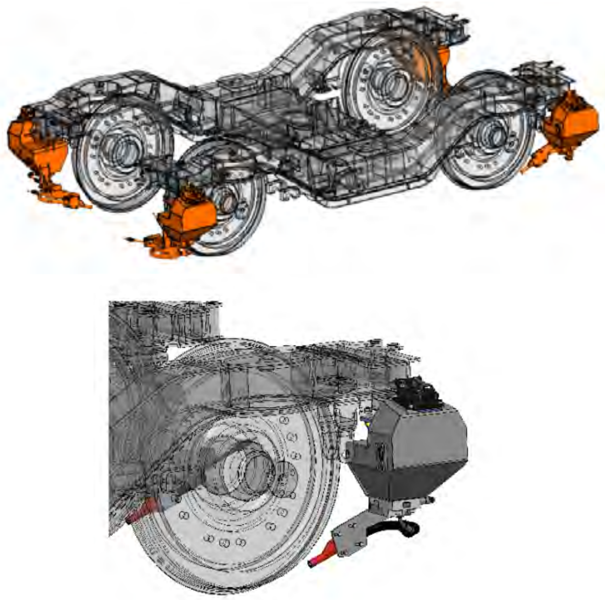

Fig. 14. Sanding system of the 41MN driving bogie

– Arrangement of electric wires on the bogie

In the construction of bogies, we can distinguish two types of electrical installation. The first of them – high-current one, supplies the actuators of devices with a safe voltage of 24 V. These elements include heaters for sand dosing nozzles of the sanding system, the wheel flange lubrication system, and the rail brake system.

The sensors mounted on the bogie constitute a second separate installation. These include sensors related to the braking system (anti-skid sensor), truck diagnostics and the Vehicle Safety System (ETCS).

The entire electrical installation is tight, i.e. all connecting elements and casing pipes are made of elements with a water-tightness class of IP68. In order to ensure the convenience of handling the box-bogie connection, all cables have been connected to a common connector located in the central part of the bogie, both the rolling and the driving bogie. The cable layouts on the bogie in question are shown in Fig. 15.

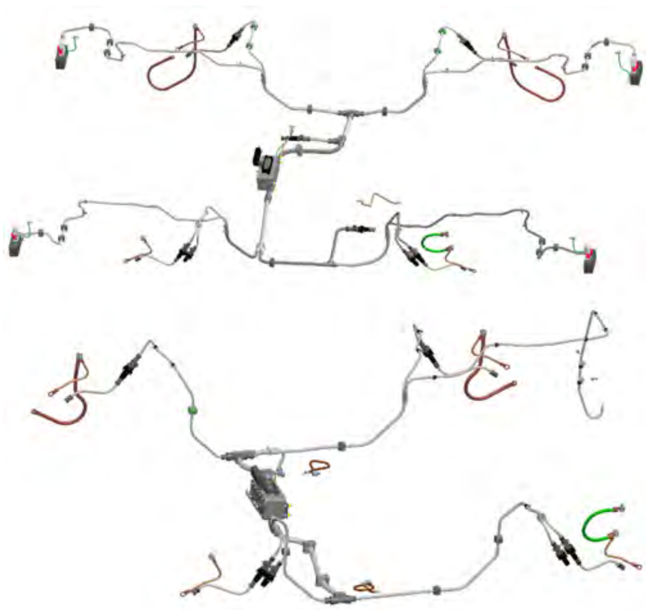

Fig. 15. Electric wiring for the 41MN (above) and 46AN (below) bogies

– Arrangement of pneumatic hoses on the bogie

The system of pneumatic conduits (Fig. 16) is made of stainless pipes, flexible connection conduits and bulkhead couplings. STAUFF clamps were used to attach the pipes to the trolley frame, which in turn

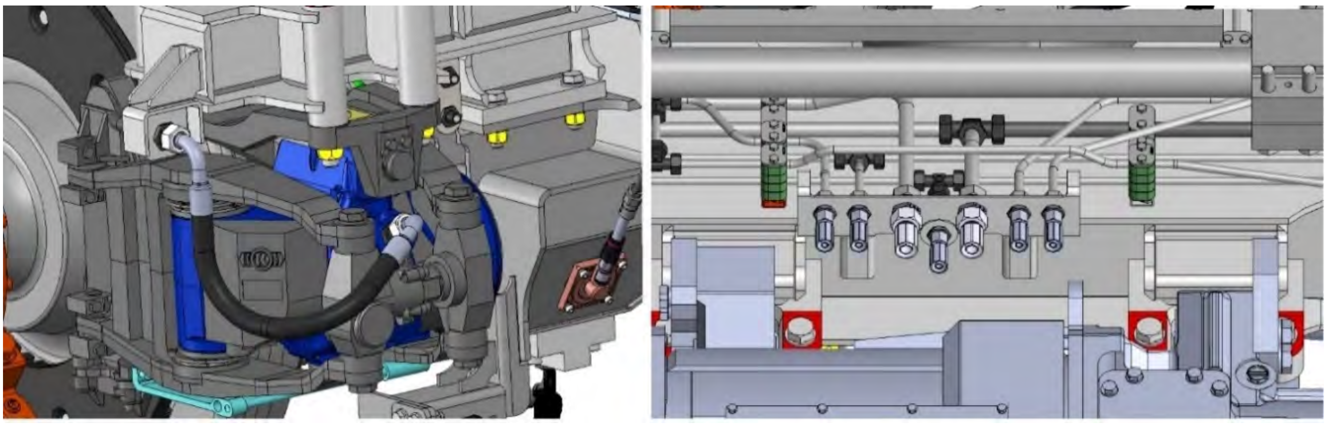

Fig. 16. The system of pneumatic hoses on the 41MN bogie

were screwed to the profiles using system T-nuts, allowing the clamps to move freely along the length of the profile. Pneumatic installation – just like the electric one, it has its connection in the central part of the bogie.

4. Summary

The 41MN and 46AN bogies have been developed for use in the 227M, 228M (FPS Plus) family of vehicles. The applied solutions of the running gear enable driving at a maximum speed of 160 km/h.

The unified structure of the frame allows for its easy adaptation to the installation of both components of the driving and rolling bogies. The basic bogie systems are designed to transfer the loads resulting from the pressure of the wheelset on the track, amounting to 18 tons. The appropriate selection of the primary and secondary suspension as well as the tractive force transmission and wheelsets guiding systems translates into good running properties of the bogies. This allows for a high level of safety, driving comfort and minimization of wheel tread wear. The use of the brake discs in the wheels made it possible to make good use of the space in the central part of the axle for the installation of the drive system.

When defining new development conditions for the designed running gears, one should take into account the criteria that must be met. The criteria should be:

– mechanical compatibility
– electrical compatibility
– pneumatic compatibility
– adequate material strength, analytically confirmed by means of calculation methods
– safety against derailment and dynamics proven by analytical calculation methods.

Nomenclature

ED	electrodynamic brake
EP-B	electro-pneumatic brake
ETCS	European Train Control System
HZT	hybrid traction units
PN	pneumatic combined brake
PS	parking spring brake
S	body roll
TBU	Tapered Bearing Unit
TSI	Technical Specifications for Interoperability
UIC	Union Internationale des Chemins de fe (International union of railways)

Bibliography

[1] Antkowiak T., Far. M. Analiza możliwości zaimplementowania wózka typu 41MN oraz 46AN do autobusu szynowego 51WE, *OR-12370*. Rail Vehicles Institute, Poznan 2021.

[2] Miklasz R. Running gears of a 227m-type mybrid vehicle. *XXIV Scientific Conference Rail Vehicles*. Cracov University of Technology, Cracov 2021.

[3] Operation and maintenance documentation of a bogie type 41MN for a rail bus 227M. Technical description. Rail Vehicles Institute, Poznan 2020.

[4] Operation and maintenance documentation of a bogie type 46AN for a rail bus 227M. Technical description. Rail Vehicles Institute, Poznan 2020.

[5] Commission Regulation (EU) No 1302/2014 of 18 November 2014 concerning a technical specification for interoperability relating to the 'rolling stock – locomotives and passenger rolling stock' subsystem of the rail system in the European Union Text with EEA relevance. http://data.europa.eu/eli/reg/2014/1302/oj

[6] Hasslinger H. Lastannahmen für Radsatzwellen–Bestandsanalyse. *Eisenbahntechnische Rundschau*. 12, 2009. https://eurailpress-archiv.de/SingleView.aspx?lng=en&show=17443

[7] Grubisic V., Fischer V. Sichere Bemessung von ICE-Radsatzwellen. *Eisenbahntechnische Rundschau*. 1-2, 2011. https://eurailpress-archiv.de

[8] Müller R. Aktuelle Probleme der Berührgeometrie Rad/Schiene. *ZEVrail Glasers*. 10(127), 2003. https://www.zevrail.de

[9] Ritscher U. Entgleisungssicherheit: Untersuchungen im Weichenbereich. *Eisenbahn-ingenieur*. 1, 2008. https://www.eurailpress.de

[10] Richard A., Sander M., Wirxel M. et al. Ermittlung von Inspektionsinterwallen mittels Risswachstumsuntersuchungen. *Eisenbahn-ingenieur*. 2, 2010. https://www.eurailpress.de

Article citation info:
Urbański P. Review of freight high speed railway (HSR). *Rail Vehicles/Pojazdy Szynowe*. 2022, 1-2, 49-61.
https://doi.org/10.53502/RAIL-152144

Rail Vehicles/Pojazdy Szynowe

www.railvehicles.eu

Review of freight high speed railway (HSR)

Patryk **Urbański**

[a] *Łukasiewicz Research Network – Poznan Institute of Technology/Center of Rail Vehicles, Poznan, Poland*

ARTICLE INFO

Received: 24 June 2022
Revised: 14 July 2022
Accepted: 15 July 2022
Available online: 20 July 2022

KEYWORDS

freight transport
cargo train
railway infrastructure
high speed railway
high speed train

The e-commerce market is gaining popularity globally every year. This market also entails the need to deliver the purchased goods at a time that is affordable for the user. One of the solutions is the use of High Speed Railway (HSR) for freight purposes, which is characterized by a relatively low rate of environmental nuisance. Based on the latest available market data and a literature review, an extensive review of the use of HSR, including for cargo transport, has been performed. The article presents an analysis of the demand for express freight transport. The potential and the demand for freight HSR have been demonstrated. The activities and analysis concerning the use of HSR for freight transport were described. Rail freight transport in Poland, Europe and China are characterized. Data on the use of the HSR infrastructure in the world are presented. HSR vehicles use for the transport of goods were presented. The potential and possibilities of using freight HSR in Europe were described. Based on the data, the use of this type of transport seems justified for LDHV shipments when the delivery time is crucial for the user and when the railway infrastructure and rolling stock are properly adapted.

1. Introduction

According to the data of the European Environment Agency from 2022 [12, 25], transport in the EU (European Union) is the only sector in which CO_2 emissions did not decrease comparing to 1990. Moreover, comparing the years 1990 and 2019, the amount of emitted compound increased by 25%. Considering GHG (Green House Gases) emissions in the EU from means of transport, the largest share of emissions come from road transport (71.7%), which mainly consists of emissions from cars (60.6%) and heavy duty trucks (27.1%). This state of affairs is caused by the availability of internal combustion vehicles and the well-developed road infrastructure in Europe [49]. Rail transport has by far the smallest share in GHG emissions in the EU, accounting for 0.4% [12], although it accounts for 8% of passenger and 19% of freight transport in Europe [42]. Despite the lowest share of harmful compounds emission among all means of transport, intensive works are being made in the railway sector to use more efficient propulsion systems [41, 44] and alternative fuels [8, 48], including hydrogen [18, 19, 24, 40] to reduce exhaust emissions [38].

Considering the emission of toxic compounds, such as heavy metals, in the EU-28 countries from non-road transport (air, rail, sea and in-land water transport), the increment factor of the described indicator, dividing into passenger and freight transport, has been growing since 2000 in both cases [25]. However, in the case of passenger transport, this increase is much bigger. In relation to the initial value, the indicator for passenger transport increased by almost 50%. Freight transport contributed to an approximately 10% increase in the emission of harmful compounds during 18 years. All of the above means that the transport of goods by rail has the lowest negative impact on the environment.

Additionally, a continuous increase in the demand for transport is noticeable, including rail transport as one of the most CO_2 emission and energy efficient [4, 29, 55] and cost-effective [31]. An example of a reason why the demand for the implementation of transport services is increasing is the e-commerce market. All over the world there is an increase in the number of transactions taking place via the Internet and online purchases. China is one of the largest representatives of this type of trade. An example is the increase in the express transport services provided in

* Corresponding author: patryk.urbanski@pit.lukasiewicz.gov.pl (P. Urbański)

this country, where in 2016 the number of transported volumes increased to 31.28 billion, and the revenues from the provision of this type of services increased 10 times since 2008 [58]. In turn, in 2020 "express transported" volume in China already reached the level of 83.4 billion pieces (Fig. 1). This means that the demand for services of this type is not only increasing but is accelerating at a dizzying pace [14, 59]. In order to cover the general demand for express transport of goods, railways are more and more often used, which on many levels can effectively compete with other means of transport.

For this reason, plans, considerations, simulations, optimizations [2, 54], predictions and real solutions for the use of HSR (High Speed Railway) for high speed freight transport [20, 35, 51, 52, 60] have been developed. Including comparative analysis of the use of air transport and HSR [47, 56], as well as the punctuality of express parcels transport by various means of transport [32] and the selection of optimal locations of consolidation centers to reduce GHG [9], mainly on China example. Works related to Freight HSR also include the development of tracking of transported goods [57], intelligent management systems [6], monitoring and calculations related to the rolling stock [3, 16] and issues related to the aerodynamics of HSR vehicles [50].

This paper describes an overview of data on freight transport in Poland, Europe and China. The key HSR railway lines in the world, on which HSR freight trains already run, were also presented, and the number of which will increase in the coming years due to a number of benefits.

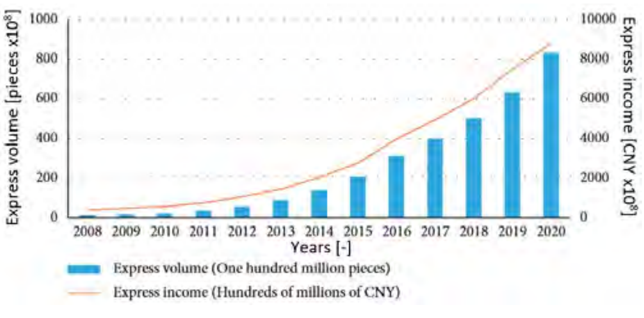

Fig. 1. The volume and income of express delivery during 2008–2020 in China [59]

2. Rail freight transport

2.1. Characteristics of rail freight transport in Poland

In order to correctly illustrate the structure of the rail market in Poland for freight transport, the data for the years 2011-2020 are presented below. The most important indicators are the mass of transported loads (Fig. 2), transport work performed (Fig. 3) and operational work (Fig. 4) [45].

Analyzing the data from 2011-2020, it can be seen that 2018 was characterized by the highest values for all three indicators, and years 2017-2019 were the best since 2011. In the case of the mass of transported goods, in 2018 it was 250.3 million tons, where the increase from 2016 was 12.6%. Then there was a decrease in 2019 to a value of 236.4 million tonnes. 2020 was the second least favorable year in the analyzed time period (only 2016 was characterized by a lower value of transported goods – a difference of 1 million tonnes). The decrease in cargo mass after 2018 could have resulted from a change in the structure of the transported groups of goods. With the same length of freight trains, the difference in weight between intermodal and mass trains is completely different. Additionally, drastic decrease in the described indicator in 2020 (–10.8% compared to 2018) was caused also by the outbreak of the COVID-19 virus pandemic, which affected not only the Polish, but also the global rail transport market [28, 46].

Fig. 2. Mass of cargo in rail freight transport in Poland in 2011-2020 (in million tonnes) [45]

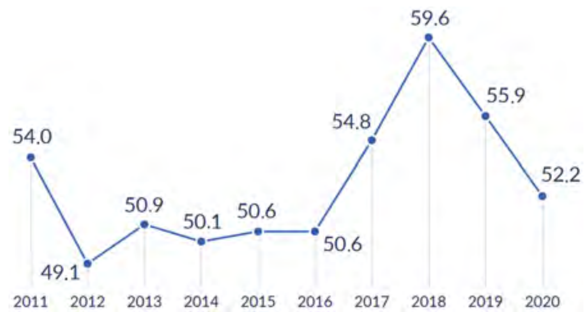

Fig. 3. Transport work performance in rail freight transport in Poland in 2011-2020 (in billion tonne-kilometers) [45]

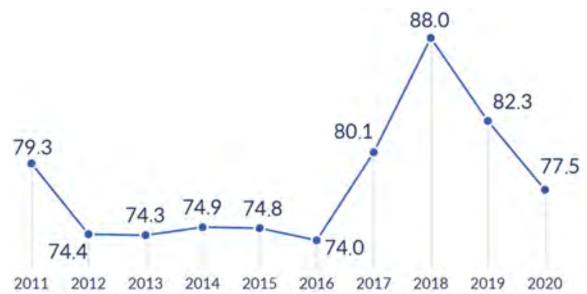

Fig. 4. Operational work in rail freight transport in Poland in 2011-2020 (in million train-kilometers) [45]

Transport work performance in 2011 amounted to 54 billion tkm (tonne-kilometers). Then, in the years 2012-2016, a stabilized situation was noticed, where the annual values were between 49.1 and 50.9 billion tkm. After this period, an increase to the value of 59.6 billion tkm was noticed in 2018 (an increase of 17.8% compared to 2016). From this year, the annual transport work performance has decreased to a value of 52.2 billion tkm in 2020.

The characteristic of the curve for operational work in 2011-2020 in Poland is very similar to the curve for transport work. In this case, the value in 2011 was 79.3 million train-kilometers. In 2012-2016, the value ranged from 74 to 74.9 million train-kilometers. Then, there was a two-year increase in the described index to the value of 88 million train-kilometers, which is the highest in the described time period. From 2018, a decrease to the value of 77.5 million train-kilometers in 2020 is visible.

Figure 5 shows the average speed for rail freight transport in general and for intermodal transport in 2013-2020 in Poland. The average speed for freight transport in 2020 was 25.9 km/h, which is the highest value in the analyzed time period. In the case of intermodal transport, the average speed was 30.3 km/h. This means that this value is one of the lowest during considered period. The lower average speed may result from the terracing of short border sections where the average commercial speed of trains is only 10 km/h. Nevertheless, intermodal transport in Poland is characterized by a higher average transport speed than conventional rail freight transport.

Fig. 5. Average commercial speed of freight trains in general and intermodal trains in Poland in 2013-2020 (km/h) [45]

Figure 6 presents the share of trains carrying out intermodal transport in particular speed ranges. Half of the transports were performed at a speed of less than 30 km/h, and almost 30% of the number of trains were going with an average speed within the range of 30–40 km/h. Only 7.66% of intermodal transports were carried out at speeds greater than 60 km/h.

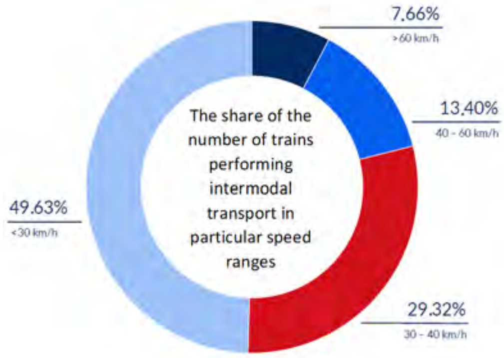

Fig. 6. Share of the number of trains performing intermodal transport in individual speed ranges in 2020 [45]

Figure 7 shows examples of intermodal trains with average speeds between reloading centers in 2020. Maximum and minimum values have been achieved on border routes. The highest speed is on the connection: Frankfurt Oder–Rzepin, where trains between Germany and Poland cover the route at an average speed of 90 km/h. In turn, the lowest value belongs to the connection: Brest–Małaszewicze. The average speed of intermodal trains on the Belarusian–Polish border is 4 km/h. Average speeds of domestic routes are varied and range from 27 km/h on the Gdańsk–Radomsko route to 63 km/h on the Gądki–Dąbrowa Górnicza route.

Fig. 7. Examples of intermodal train speed in Poland in 2020 [45]

Intermodal transport in Poland uses a rolling stock consisting mainly of platform wagons, of which there are over 13,000 in Poland. Trailed vehicles are also used for this type of transport to carry containers. In 2020, there were over 5,800 such vehicles. Considering the possibility of achieving the maximum speed of platform wagons for container transport, the speed higher than 100 km/h can only be reached by 23% of wagons (max 120 km/h). The other vehicles are designed for a maximum speed of 100 km/h.

2.2. Characteristics of rail freight transport in Europe

The transport work performance in rail freight transport in Poland against the background of European countries for the years 2010, 2019 and 2020 is presented in Fig. 8 [43]. In Europe, only in Germany in above-mentioned years transport work performance was greater than in Poland. In 2020, Germany was responsible for 30% of the total transport work performance in the European Union, amounting to 108 trillion tkm (twice as much as in Poland – 50 million tkm). In almost all countries, the described indicator increased in 2020 compared to 2010.

One of the indicators in rail freight is the transported mass of goods. In Europe, the leader in this ranking is also Germany. However, when comparing the years 2019 and 2020, it can be stated that the COVID-19 pandemic had a significant impact on the mass of transported loads. Only five EU countries noticed an increase in this indicator. In other cases, declines were noticed. Taking into account the number of transported mass, the most severe situation was related to Germany, where the decrease amounted to 20 million tons year on year, while the relatively largest decrease was recorded in Latvia, where the decrease amounted to 42% (Fig. 9).

Taking into account the characteristics of the goods transported in the EU, the classified goods that were transported in the greatest amount in 2020 were metal ores, which accounted for 12.8% of the total number, taking into account tkm. Coke and refined petroleum products, second in the ranking, accounted for 9.8%. The largest part, however, were goods that can be characterized as: other or not identified (38.2%) (Fig. 10).

In the case of goods counted in tonnes, in this case, classified goods also had the largest share of metal (15.6%). Coal and crude petroleum was second (12.1%), and the third major commodity was coke and refined petroleum (12.1%). As in the case of transport work performance, the products other or not identified constituted the largest part in the summary, as they comprised 1/3 of the share (Fig. 11). One of the solutions used in the transport of goods in Europe is also intermodal transport applied to the so-called LDHV (Low Density High Value) goods [7, 30].

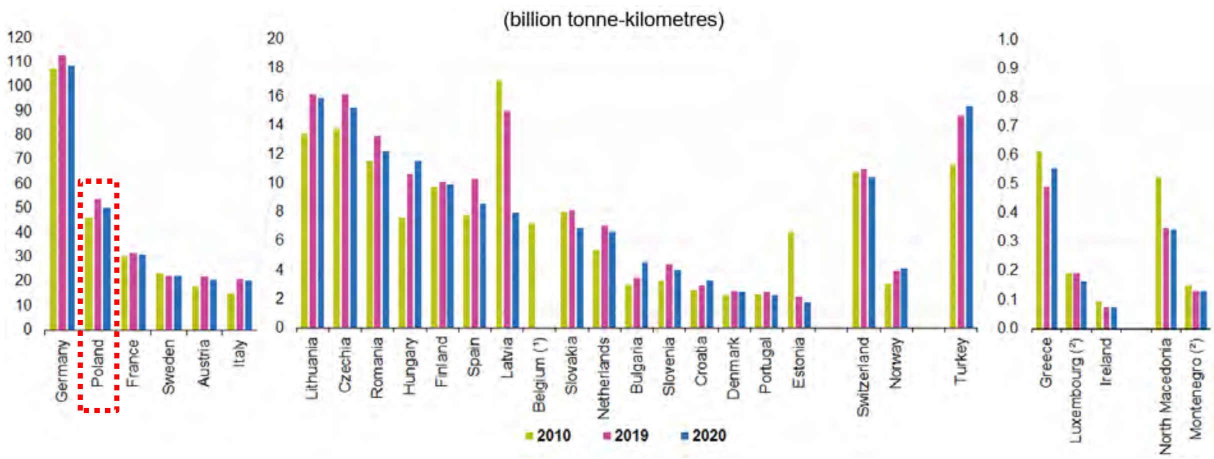

Fig. 8 Rail freight transport for main undertakings, 2010, 2019 and 2020 (billion tonne-kilometres). Countries are ranked based on 2020 data. Cyprus and Malta have no railways. (¹) 2019 and 2020 data not available. (²) 2010 based on quarterly data [43]

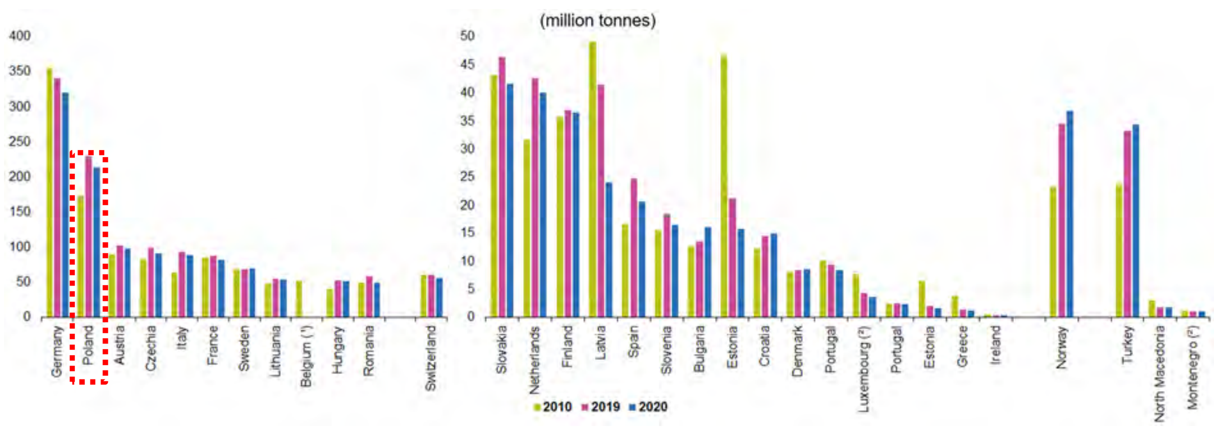

Fig. 9. Rail freight transport for main undertakings, 2010, 2019 and 2020 (million tonnes). Countries are ranked based on 2020 data. Cyprus and Malta have no railways. (¹) 2019 and 2020 data not available.(²) 2010 based on quarterly data [43]

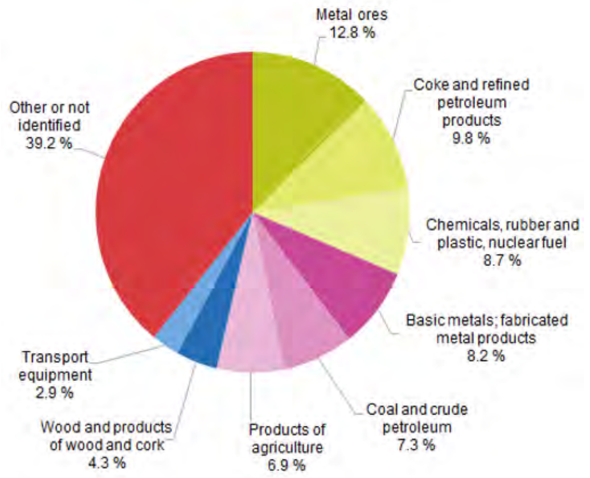

Fig. 10. Rail freight transport by type of goods for main undertakings, EU, 2020. Share based on tonne-kilometres [43]

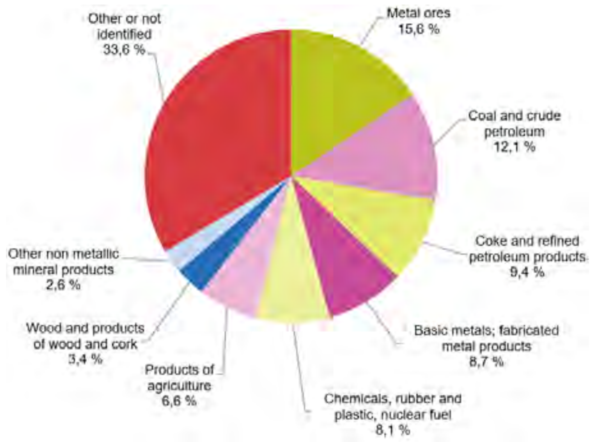

Fig. 11. Rail freight transport by type of goods for main undertakings, EU, 2020. Share based on tonnes [43]

3. High Speed Railway

High speed railway is a form of transport that is gaining more popularity all over the world every year [33]. Thanks to this form of transport, including more and more easier access to high speed communication for ordinary passengers, the possibilities of daily commuting of employees from distant regions to the place of employment increase significantly [17]. Every year, multi-million investments are made to expand the railway network adapted to moving at high speeds. According to UIC (International Union of Railways) [5] data, there are 20 countries in the world that have high speed railways, and the total length of HSR lines in the world is 56,130 km.

The country with the most extensive HSR is China. It is a world leader in this area with 38,283 km of lines. For comparison, the second country in the world with the longest HSR line is Spain with 3,487 km, which is over 11 times less than China. Asian countries with HSR lines are also Japan (3,041 km) and South Korea (893 km). Considering such an extensive infrastructure, especially in China, HSR in Asia accounts for 75% of the total length of HSR in the world. In Europe there is 21% of the total length of the HSR in the world (11,819 km), in the Middle East it is less than 2.1% (1,173), in North America (USA) 1.3% (735 km), and the rest of the lines (186 km) are located in Africa, more precisely in Morocco (Fig. 12).

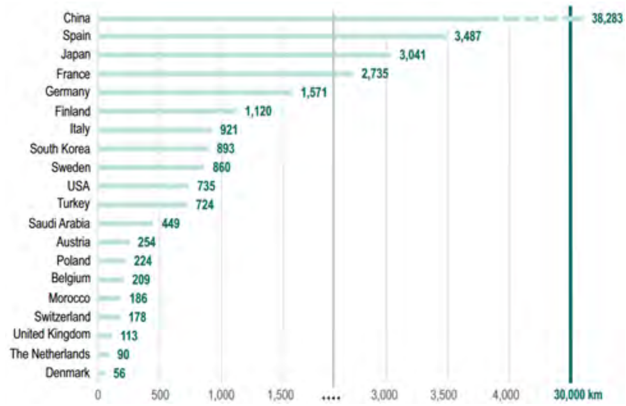

Fig. 12. Length of the high speed railway network in commercial operation by country [5]

Currently, the HSR line in the world is being expanded and according to the available data, 22,562 km of the line are under construction. This means that after the completion of construction, the network of HSR lines in the world will be 40% longer than today. The largest part of the expansion takes place in Asia, where 16,515 km of HSR lines are currently under construction. 3,079 km of lines are built in the Middle East, 2,405 km in Europe and 563 km of lines in North America.

It is worth noting that since 1990, when the total length of the HSR lines in the world was 2,767 km, the length of this type of lines has increased 155 times. One of the main reasons was the launch of intensive operations in China, where, among others, in 2008, the fastest railway route in the world those days, Beijing–Tianjin, was put into use with a maximum speed of 350 km/h. So far, it is still the fastest railway line in the world. Countries with the fastest railway lines having a maximum speed limit of 320 km/h are Japan, France and Morocco (Fig. 13).

Due to the length of the HSR lines, China is in first place. However, taking into account the density of the HSR network, the index of HSR lines per km^2 of the country, China is 8th in the ranking (3.989 m/km^2). This is due to the enormous area of the country and a significantly developed infrastructure, especially in the east of the country. South Korea has the densest HSR line (8.911 m/km^2), while Japan is in second place (8.045 m/km^2). European countries with the highest density index are Spain (6.892 m/km^2) and Belgium (6.846 m/km^2). Among the countries with HSR, the lowest value of the described index are countries outside Asia and Europe, i.e. Morocco (0.417 m/km^2), Saudi Arabia (0.209 m/km^2) and the USA (0.075 m/km^2) (Fig. 14). Figure 15 and Fig. 16 show the HSR network in Asia and in Europe, respectively.

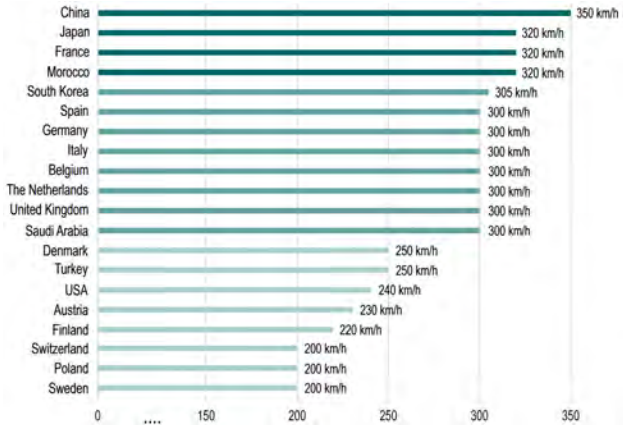

Fig. 13. Maximum speed of high-speed rail network by country (2020) [5]

Fig. 14. Density of the high-speed network in 2020 (meters of high-speed lines/country area in km^2 [5]

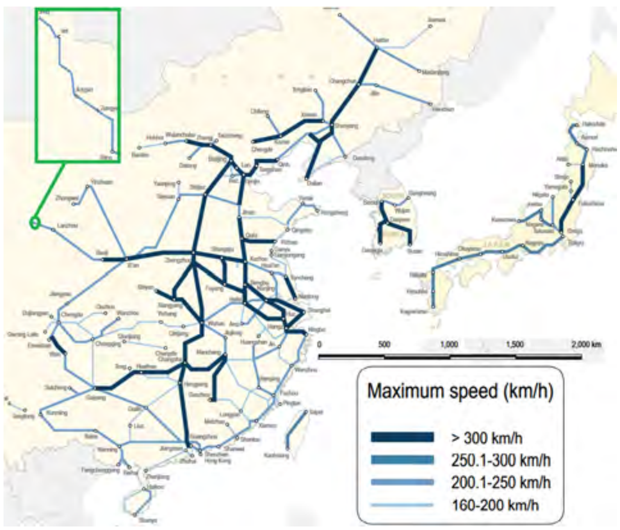

Fig. 15. Japan, South Korea and China Railway High-Speed (CRH) lines [5]

Fig. 16. High-speed railway lines in Europe [5]

4. Freight high speed trains

Rail transport using HSR was designed with passenger transport in mind. This is also confirmed by statistics, which say, among other things, that in China in 2020, despite the COVID pandemic, 2,357.7 million passengers used these services, and in Japan – 354.6 million passengers. This means that this type of transport has become a generally accessible form of transport for passengers. Due to the fast travel time, this type of railway has a significant potential for the transport of goods. The use of HSR for freight services is not only a plan, but is already being implemented on certain sections of the railway lines. Examples of the use of HSR in freight transport are presented below.

4.1. ETR.500 M-01 rail vehicle

The world's first high speed freight line was put into operation on November 7, 2018 by the Italian operator Mercitalia Fast (Gruppo FS Italiane). The line connects the Maddaloni-Marcianise terminal in Caserta with the Bologna Interport (approx. 550 km) (Fig. 17), one of the most important logistics hubs in northern Italy [36, 37]. Trains used for this operations (Fig. 18) are specially modernized and designed to transport time-sensitive products for customers such as couriers, logistics operators, manufacturers, distributors and developers.

Fig. 17. Italian high speed rail route used for freight transport [36]

Fig. 18. The Italian high speed freight train ETR M-01 Fast, a modernized version of the ETR 500 vehicle [39]

For this special and innovative service, the ETR 500 multiple unit rail vehicle (currently classified as ETR M-01 Fast) was used, consisting of two multi-system drive units – E.404.514, E.404.516, and 12 passenger units. Adaptation of passenger units for freight transport was made in workshops in Vicenza and Voghera. The air conditioning system and 220 volt static transducers for passenger services and electrical sockets have been removed. This operation had to be performed to compensate for 3.6 tons of ballast in order to maintain stability. The wagons (units) are equipped with a fire suppression system compliant with the TSI 2014 specification by means of two fire extinguishers and special ceiling smoke detectors. Each vehicle also has two cameras connected to a screen in the driver's cab. The lighting is made of neon tubes placed on the ceiling alongside the vehicle.

The transport capacity of the modernized vehicle is equal to 18 road semi-trailers or two Boeing 747 airplanes. The cargo space is divided into 12 sections, called wagons after modernization. Each wagon has 17 load spaces (boxes) called "racks" and numbered in ascending order from 1 to 17 (Fig. 19). In total, in one wagon there is space for 60 containers with dimensions of 71×80×180 cm (Fig. 20).

Fig. 19. Scheme of the internal division of each wagon with 17 boxes designed to put the containers on wheels and to mark the 12 wagons in the M01 train [22]

Fig. 20. Freight space in one of the wagons of the ETR M-01 Fast train by Mercitalia [36]

One container takes up a space of about 1 m^3 and it is possible to transport up to 250 kg of goods in it. The shipping unit is designed for easy and quick loading and unloading due to the use of wheels (Fig. 21).

Fig. 21. Loading of containers on wheels to the high speed freight train ETR M-01 Fast [34]

In terminals, the loading and unloading of wheeled containers is carried out by means of 12 removable platforms that connect the warehouse dock with the level of the train floor. The operations are therefore only performed through one door (Fig. 22). The use of such a solution allows to maintain 17 tons of load per axle, which is a value required on high speed lines.

Fig. 22. Loading platform in the ETR M-01 Fast vehicle [34]

The yellow tubular structures are a frame for securing the containers and allow the containers to be fastened with special belts (Fig. 23). The standard load capacity is 7 tons per wagon, however, in the case of transporting heavier goods, it is possible to remove/adjust the ballast.

Fig. 23. Containers in the cargo area secured with belts and prepared for transport [36]

The train runs between the Maddaloni-Marcianise terminal (Caserta near Naples) and Bologna Interporto in 3 h and 20 minutes (average speed 180 km/h). A truck covers the same route in about 6–7 hours. Although the vehicle is adapted to a maximum speed of 300 km/h, it was decided to limit the driving speed of the ETR.500 M-01 to 250 km/h. Data on the ETR 500 train and the modernized version of the ETR.500 M-01 are presented in Table 1.

Mercitalia estimates that its new service could remove nearly 9,000 trucks from the heavily congested A1 motorway, which would reduce carbon dioxide emissions to the atmosphere by around 80% compared to road transport.

4.2. Fuxing CR400BF

The Chinese State-owned Rolling Stock Manufacturer – CRRC – provided transportation services for the Double 11 Shopping Festival 2020 from November 1 to November 20, 2020, it was a worldwide online shopping festival. In order to improve operational efficiency, the Chinese National Rail Administration has allowed the CRRC to convert Fuxing CR400BF trains (Fig. 24) from passenger to freight trains, ensuring that trains can be completely converted back [15].

On November 1, 2020, the Fuxing CR400BF-3087 high speed train, the first to convert to a freight electric multiple unit, took off with 40 tons of packages and crates from Beijing and Tianjin shipped to the Double 11 Shopping Festival (Fig. 25). Friction belts and pulley systems were temporarily used on the train and on the platform, not only to prevent damage to the floor and packaging, but also to improve loading efficiency. The train reached the Hankou railway station in Wuhan in five hours, traveling over 1,100 km between Beijing and Wuhan. Carrying out the transport proves the feasibility of the service.

Table 1. Technical data of the ETR 500 and ETR.500 M-01 units [21, 36]

	ETR 500 (passenger)	ETR.500 M-01 (modernized freight)
Producer	Trevi (Alstom, Bombardier, AnsaldoBreda consortium)	
Production	30 complete multiple units + 60 drive units (for 1st generation single system sets)	1
Number in use	59 passenger multiple units	1
System	drive unit + 11 intermediate units + drive unit (originally-2004, 2011-present) drive unit + 12 intermediate units + drive unit (2004-2010) drive unit + 8 intermediate units + drive unit (ETR 500 F, Turin-Milan)	drive unit + 12 intermediate units + drive unit
Carrier	FS/Trenitalia	Mercitalia Rail
Maximum speed	360 km/h	250 km/h (limited for safety reasons) 300 km/h (no limits)
Continuous power	2×4400 kW	
Number and type of motors	8 asynchronous electric motors	
Mass	598 t	
Gauge	1435 mm	
Transport capacity	575 passengers	from 7 t to 10.6 t – per intermediate unit

Table 2 presents the most important data concerning the CRRC Electric Multiple Unit (EMU) – the Fuxing CR400BF vehicle. The vehicle is adapted to travel at a speed of 420 km/h, but the usable speed is 350 km/h.

The Fuxing CR400BF high-speed train is characterized by the ability to carry out high speed journeys, punctuality, safety and with environmental protection, which corresponds to the modern requirements of the large-scale transport and logistics sector. According to the CRRC, in the future, the company will continue to research the EMU rapid delivery service [26].

Fig. 24. CR400BF train at Beijing South station [23]

Fig. 25. Load space of the CR400BF high speed train adapted to the freight transport [26]

Table. 2. Technical data of the CR400BF vehicle [13]

Fuxing CR400BF		
Producer	CRRC Changchun Railway Vehicles Co., Ltd.	[–]
Production	2016-present	[years]
System	8 units (4 drive units, 4 driven units)	[–]
Maximum speed	420	[km/h]
Usable speed	350	[km/h]
Traction power	10 140	[kW]
Electric motors	YQ-625 3 Phase AC Induction Motor (Zhuzhou CRRC Times Electric)	[–]
Number and type of motors	8 asynchronous electric motors	[pcs]
Width	3 360	[mm]
Height	4 050	[mm]
Length	211	[m]
Gauge	1 435	[mm]
Axle load	< 17	[t]
Type of traction	25/50 AC from overhead power lines	[kV/Hz]
Traction system	Water cooled Inverter control IGBT-VVVF (Zhuzhou CRRC Times Electric)	[–]

4.3. China's first high-speed freight train

A new generation of high speed freight trains that can carry up to 110 tons of goods rolled off the production line in Tangshan, Hebei Province in northern China (Fig. 26). The new trains, developed by CRRC Tangshan Co Ltd, a part of China Railway Rolling Stock Corp, the country's largest rolling stock producer in terms of production volume, can travel at a maximum speed of 350 km/h [10, 27, 53].

Fig. 26. Chinese high speed freight train in a production hall [11]

Equipped with eight units, the EMU is also characterized by an increased ability to adapt to weather changes. The vehicle can operate in temperatures from –25°C to 40°C. Unlike air and road transport, the high speed freight train is less exposed to the elements, such as heavy rain and strong winds. Train is able to cover 1,500 km distance in five hours [11].

A high speed freight train uses technologies such as big data analysis, Beidou satellite navigation systems, virtual information storage in the cloud, ultra-wide range solutions, precise weight control of transported goods and advanced algorithms for intelligent storage goods and load distribution in the cargo space. These systems are also helpful in working procedures such as accurate identification and positioning of cargo during cargo loading and unloading operations. Each wagon has a pair of loading doors 2.9 m wide, which means those train cargo doors have the largest degree of opening in the world (Fig. 27).

Fig. 27. Loading door – 2.9 m wide [11]

In the cargo spaces is designed floor system with built-in conveyors (Fig. 28), which automatically distribute the goods on the vehicle (Fig. 29). Filling the cargo space with transport units thanks to this system reaches the level of 85% (Fig. 30). The system used is similar to that used in transport aircraft.

Fig. 28. Automatic floor conveyor system for cargo [1]

Fig. 29. Platform for automatic distribution of transported goods in the cargo space [1]

High speed freight trains meet the demand for high speed freight transport over medium and long distances ranging from 600 km to 1,500 km. This type of train has significant advantages such as transport on time, high frequency of goods handling, low transport costs and operational capability regardless of the weather.

The front end of the high speed freight train uses the bionic structure of the Chinese sturgeon (fish) skeleton, which increases the slimness of the front of the vehicle. The results of the wind tunnel tests showed that the shape and design of the vehicle nose are very advanced and significantly reduce the running resistance compared to the existing models (Fig. 31).

Fig. 30. Loading space with transport units [1]

China is seeking to increase its global competitiveness in the rail sector by expanding rail networks with a wider range and higher speeds. The Chinese rail operator China State Railway Group plans to build 200,000 km of railroads by the end of 2035, and big part of this will be HSR. All cities over 200,000 residents will be connected to the rail network by 2035, and cities larger than 500,000 will have access to the HSR network [14]. It means that such express vehicles will be more and more needed.

5. Summary

The transport of goods, especially express transport, becomes a determinant of modern trade and enables the efficient development of the economy. The rapid development of the e-commerce department, which makes online trading possible, contributed significantly. Ordinary users have the opportunity to buy or sell items that reach the recipient in record time. Meeting such demanding time standards is extremely complicated and requires the involvement of a well-developed transport infrastructure. On the other hand, the use of a high speed means of transport generates significant costs. This means that in some cases express transport may not be an effective solution.

Fig. 31. First, specially designed Chinese high speed freight train [11]

The examples presented in the article show, despite the increased costs, a significant increase in the popularity of express freight transportation. For this reason, the use of HSR – classified as the top of the most expensive form of rail transport, until recently reserved only for passengers – becomes an interesting prospect with great potential for the implementation in freight transport.

The most developed country in this area is China, which, having the longest HSR network in the world, is intensively working on express freight transport. The solutions of the high speed passenger train Fuxing CR400BF were developed, which, after being adapted to the transport of goods, became a cargo vehicle.

A special EMU vehicle is the recently developed by CRRC Tangshan Co Ltd. It is unique because it is the world's first rail vehicle designed from the beginning for freight transport at speeds of up to 350 km/h. The vehicle also has an automated cargo space, which significantly contributes to increasing the efficiency of the transport. It seems that China, planning huge investments related to the expansion of the HSR network, will increasingly look for solutions in freight transport using HSR.

In the case of Europe, a fairly well-developed HSR network is used so far for passenger transport. The exception is the solution in Italy, where the carrier Mercitalia Fast adapted the Italian high speed train called ETR M-01 Fast for freight transport. The vehicle regularly running on a high speed route with a length of over 500 km is intended for the so-called LDHV shipments and is an advantageous alternative to other modes of transport.

Mercitalia Fast uses the HSR line dedicated to passenger transport and runs through two important transport terminals. Interporto Bologna, one of the largest intermodal logistics hubs in Europe, is home to more than 120 industrial and freight logistics companies and three rail terminals. Interporto Maddaloni-Marcianise, near Caserta is big terminal 30 km from Naples. Due to the location of the terminals and the HSR line connecting them, it was decided to use the HSR train for the transport of goods.

The reasons for the lack of use of HSR in Europe on a larger scale are mainly financial reasons, as well as the nature of the goods transported. In the EU, rail transport mainly transports goods with large dimensions and weight. Such goods do not require transport at high speeds, which is confirmed, inter alia, by the average transport speed of freight trains in Poland (the second country in Europe in terms of rail freight transport work performed) of 25 km/h.

In the event of an increased demand for express freight, the railway infrastructure in European countries with HSR is well-adapted. Therefore, it seems necessary to establish regular long-distance connections while maintaining the profitability of transport. Additionally, the development of logistics centers adapted to this type of transport would be needed.

Such created line for freight HSR would be used for the transport of light goods inside the country due to the small number of connections of the HSR network between countries. An alternative to international connections for the transport of freight HSR would be international connections with a reduced average shipping speed, with only sectional increased speeds.

Nomenclature

CRH	china railway high-speed
EMU	electric multiple unit
ERTMS	European rail traffic management system
EU	European Union
GHG	green house gases
HSR	high speed train
LDHV	low density high value
UIC	international union of railways
tkm	tonne-kilometers

Bibliography

[1] A bullet freight train with a designed speed of 350 km/h rolls off the assembly line in Tangshan, China. It’s the world’s first 350 km/h freight train. *China Xinhua News*. https://twitter.com (accessed on 06.2022).

[2] Abramov A., Podorozkina A., Bilenko G. et al. Optimization of freight train speeds on railway transport. *Transportation Research Procedia*. 2022, 61, 371-375. https://doi.org/10.1016/j.trpro.2022.01.060

[3] An W., Wu R., Shi J. et al. Research on hunting instability monitoring system of high speed freight bogie. *IOP Conference Series: Materials Science and Engineering*. 2020, 790(1), 012170 https://doi.org/10.1088/1757-899X/790/1/012170

[4] Andrzejewski M., Daszkiewicz P., Gallas D. et al. Methods of reducing energy consumption for mass transit vehicles. *Rail Vehicles/Pojazdy Szynowe*. 2016, 3, 13-20. https://doi.org/10.53502/RAIL-138737

[5] Atlas – High-speed Rail 2021. https://uic.org (accessed on 06.2022).

[6] Balog M., Sokhatska H., Iakovets A. Intelligent systems in the railway freight management. In: Trojanowska J., Ciszak O., Machado J. M., Pavlenko I. eds., Advances in Manufacturing II, *Springer International Publishing*. Cham. 2019, 390-405. https://doi.org/10.1007/978-3-030-18715-6_33

[7] Boehm M., Arnz M., Winter J. The potential of high-speed rail freight in Europe: how is a modal shift from road to rail possible for low-density high value cargo?. *European Transport Research Review*. 2021, 13(1), 4. https://doi.org/10.1186/s12544-020-00453-3

[8] Breuer J.L., Scholten J., Koj J.C. et al. An overview of promising alternative fuels for road, rail, air, and inland waterway transport in Germany. *Energies*. 2022, 15(4), 1443. https://doi.org/10.3390/en15041443

[9] Cheng Z., Zhao L., Wang G. et al. Selection of consolidation center locations for China railway express to reduce greenhouse gas emission. *Journal of Cleaner Production*. 2021, 305, 126872. https://doi.org/10.1016/j.jclepro.2021.126872

[10] China presents freight train to break speed record with 350 kmph. https://www.railtech.com (accessed on 06.2022).

[11] China's high-speed trains enter the freight sector. https://www.linkedin.com (accessed on 06.2022).

[12] CO_2 emissions from cars: facts and figures (infographics) | News | European Parliament https://www.europarl.europa.eu (accessed on 06.2022).

[13] CRRC high speed train – fuxing. https://www.crrcgc.cc (accessed on 06.2022).

[14] CRRC Tangshan unveils high speed freight train. http://www.railpage.com.au (accessed on 06.2022).

[15] CRRC uses fuxing high-speed EMU for Double 11 Shopping Festival | EqualOcean. https://equalocean.com (accessed on 06.2022).

[16] Deng G., Peng Y., Yan C. et al. Running safety evaluation of a 350 km/h high-speed freight train negotiating a curve based on the arbitrary Lagrangian-Eulerian method. *Proceedings of the Institution of Mechanical Engineers, Part F: Journal of Rail and Rapid Transit*. 2021, 235(9), 1143-1157. https://doi.org/10.1177/0954409720986283

[17] Dong X. High-speed railway and urban sectoral employment in China. *Transportation Research Part A: Policy and Practice*. 2018, 116, 603-621. https://doi.org/10.1016/j.tra.2018.07.010

[18] Durzyński Z. Hydrogen-powered drives of the rail vehicles (part 1). *Rail Vehicles/Pojazdy Szynowe*. 2021, 2, 29-40. https://doi.org/10.53502/RAIL-139980

[19] Durzyński Z. Hydrogen-powered drives of the rail vehicles (part 2). *Rail Vehicles/Pojazdy Szynowe*. 2021, 3, 1-11. https://doi.org/10.53502/RAIL-142694

[20] Ertem M.A. Keskin Özcan M. Freight transportation using high-speed train systems. *Transportation Letters*. 2016, 8(5), 250-258. https://doi.org/10.1080/19427867.2015.1122395

[21] ETR 500, Wikipedia. https://en.wikipedia.org (accessed on 06.2022).

[22] Ferrovie.it – Mercitalia Fast, l'ETR.500 per le merci ad alta velocità. https://www.ferrovie.it (accessed on 06.2022).

[23] Fuxing (train), Wikipedia. https://en.wikipedia.org (accessed on 06.2022).

[24] Gallas D., Stobnicki, P. Adoption of modern hydrogen technologies in rail transport. *Journal of Ecology Engineering*. 2022, 23(3), 84-91. https://doi.org/10.12911/22998993/145291

[25] González Ortiz A., Guerreiro C., Soares J. Air quality in Europe: 2020 report. *European Environment Agency*. Publications Office, LU, 2020. https://data.europa.eu/doi/10.2800/786656

[26] High speed rail freight in China: cargo-partner. https://www.cargo-partner.com (accessed on 06.2022).

[27] High-speed trains buoy freight sector. http://global.chinadaily.com.cn (accessed on 06.2022).

[28] Impacts of the COVID-19 crisis and national responses on European railway markets in 2020. Independent Regulator's Group – Rail. https://irg-rail.eu (accessed on 06.2022).

[29] International Energy Agency, The Future of Rail: Opportunities for energy and the environment. OECD, 2019. https://doi.org/10.1787/9789264312821-en

[30] Islam D.M.Z., Zunder, T.H. Experiences of rail intermodal freight transport for low-density high value (LDHV) goods in Europe. *European Transport Research Review*. 2018, 10(2), 24. https://doi.org/10.1186/s12544-018-0295-7

[31] Janić M. Estimation of direct energy consumption and CO_2 emission by high speed rail, transrapid maglev and hyperloop passenger transport systems. *International Journal of Sustainable Transportation*. 2021, 15(9), 696-717. https://doi.org/10.1080/15568318.2020.1789780

[32] Jia X., He R., Chai H. Optimizing the number of express freight trains on a high-speed railway corridor by the departure period. IEEE Access. 2020, 8, 100058-100072. https://doi.org/10.1109/ACCESS.2020.2995176

[33] Jiao J., Harbin J., Li Y. Fast tracks: a comparison of high speed rail in China, Europe and the United States. *Journal of Transportation Technologies*. 2013, 3, 57-62. https://doi.org/10.4236/jtts.2013.32A007

[34] Kemmeter A.F. de, Fast Mercitalia: parcels at 250 km/h. https://mediarail.wordpress.com (accessed on 06.2022).

[35] Ma M., Zhao P., Qiao K. Study on night transportation organization of high-speed rail express products. *Journal of Physics: Conference Series*. 2021, 1732(1), 012040. https://doi.org/10.1088/1742-6596/1732/1/012040

[36] Merci-Italia fast. http://www.clamfer.it (accessed on 06.2022).

[37] Mercitalia Fast: the world's first high-speed rail freight service. https://www.railway-technology.com (accessed on 06.2022).

[38] Merkisz-Guranowska A., Andrzejewski M., Daszkiewicz P. et al. Modern systems for reducing the toxicity of rail vehicle exhaust. *Rail Vehicles/Pojazdy Szynowe*. 2016, 3, 33-38. https://doi.org/10.53502/RAIL-138739

[39] Pallotta L. Ferrovie: un anno di ETR 500 Mercitalia Fast. https://www.ferrovie.info (accessed on 06.2022).

[40] Pielecha I., Engelmann D., Czerwinski J. et al. Use of hydrogen fuel in drive systems of rail vehicles. *Rail Vehicles/Pojazdy Szynowe*. 2022, 1, 10-19. https://doi.org/10.53502/RAIL-147725

[41] Pielecha I., Merkisz J., Andrzejewski M. et al. Ultracapacitors and fuel cells in rail vehicle drive systems. *Rail Vehicles/Pojazdy Szynowe*. 2019, 2, 9-19. https://doi.org/10.53502/RAIL-138526

[42] Rail transport should once again become a driver of development – EU monitor. https://www.eumonitor.eu (accessed on 06.2022).

[43] Railway freight transport statistics. https://ec.europa.eu (accessed on 06.2022).

[44] Rasiński T., Michnej, M. Application of hybrid drives in diesel locomotives. *Rail Vehicles/Pojazdy Szynowe*. 2019, 1, 18-25. https://doi.org/10.53502/RAIL-138503

[45] Report on rail transport market operations 2020. The Office of Rail Transport, 2021. https://utk.gov.pl (accessed on 06.2022).

[46] Schofer J.L., Mahmassani H.S., Ng M.T.M. Resilience of U.S. Rail intermodal freight during the COVID-19 pandemic. *Research in Transportation Business & Management*. 2022, 43, 100791. https://doi.org/10.1016/j.rtbm.2022.100791

[47] Socorro M.P., Viecens M.F. The effects of airline and high speed train integration. *Transportation Research Part A: Policy and Practice*. 2013, 49, 160-177. https://doi.org/10.1016/j.tra.2013.01.014

[48] Stawecki W., Merkisz-Guranowska A., Andrzejewski M. et al. The use of alternative fuels in railway vehicles. *Rail Vehicles/Pojazdy Szynowe*. 2017, 1, 10-19. https://doi.org/10.53502/RAIL-138459

[49] Szymanski P., Ciuffo B., Fontaras G. et al. The future of road transport in Europe. Environmental implications of automated, connected and low-carbon mobility. *Combustion Engines*. 2021, 186(3), 3-10. https://doi.org/10.19206/CE-141605

[50] Tian H. Review of research on high-speed railway aerodynamics in China. *Transportation Safety and Environment*. 2019, 1(1), 1-21. https://doi.org/10.1093/tse/tdz014

[51] Watson I., Ali A., Bayyati A. An investigation into the benefits and constraints of shifting freight traffic from roads onto high-speed railways. *WIT Transactions on The Built Environment*. 2018, 541-551. https://doi.org/10.2495/CR180481

[52] Watson I., Ali A., Bayyati A. Freight transport using high-speed railways. International Journal of Transport Development and Integration. 2019, 3(2), 103-116. https://doi.org/10.2495/TDI-V3-N2-103-116

[53] World's first 350 km/h freight train off assembly line – Xinhua | English.news.cn. http://www.xinhuanet.com (accessed on 06.2022).

[54] Xiao H., Huang S., Hang B. et al. Optimization of operation plan for express freight train. *Kuwait Journal of Science*. 2021, 48(1), 50-58. https://doi.org/10.48129/kjs.v48i1.7800

[55] Xu X., Kent S., Schmid F. Carbon-reduction potential of electrification on China's railway transport: An analysis of three possible future scenarios. *Proceedings of the Institution of Mechanical Engineers, Part F: Journal of Rail and Rapid Transit*. 2021, 235(2), 226-235. https://doi.org/10.1177/0954409720921989

[56] Yang H., Dobruszkes F., Wang J. et al. Comparing China's urban systems in high-speed railway and airline networks. *Journal of Transport Geography*. 2018, 68, 233-244. https://doi.org/10.1016/j.jtrangeo.2018.03.015

[57] Yi L., Jiang P., Zhang D. et al. Freight train speed tracking based on optimal preview control. *2021 IEEE 5th Conference on Energy Internet and Energy System Integration* (EI2). 2021, 4167-4173. https://doi.org/10.1109/EI252483.2021.9713225

[58] Yu X., Lang M., Gao Y. et al. An empirical study on the design of China high-speed rail express train operation plan – from a sustainable transport perspective. *Sustainability*. 2018, 10(7), 2478. https://doi.org/10.3390/su10072478

[59] Yu X., Zhou L., Huo M. et al. Research on high-speed railway freight train organization method considering different transportation product demands. *Mathematical Problems in Engineering*. 2021, 5520867, 1-17. https://doi.org/10.1155/2021/5520867

[60] Zhao L., Zhao Y., Hu Q. et al. Evaluation of consolidation center cargo capacity and locations for China railway express. *Transportation Research Part E: Logistics and Transportation Review*. 2018, 117, 58-81. https://doi.org/10.1016/j.tre.2017.09.007

Article citation info:
Nagórny B., Maćkowiak A., Rokossowski M. et al. Implementation of the test method for trackside emissions of magnetic disturbances from rolling stock according to ERA/ERTMS/033281. *Rail Vehicles/Pojazdy Szynowe*. 2022, 1-2, 62-67. https://doi.org/10.53502/RAIL-152231

Rail Vehicles/Pojazdy Szynowe

www.railvehicles.eu

Implementation of the test method for trackside emissions of magnetic disturbances from rolling stock according to ERA/ERTMS/033281

Bartłomiej **Nagórny** [*], Adam **Maćkowiak**, Michał **Rokossowski**, Krzysztof **Sieczkarek**, Radosław **Szczepański**, Tomasz **Warzyński**

[a] *Łukasiewicz Research Network – Poznan Institute of Technology, Poznan, Poland*

ARTICLE INFO

Received: 9 March 2022
Revised: 15 July 2022
Accepted: 20 July 2022
Available online: 20 July 2022

KEYWORDS

EMC testing
LabView software
railway transport
traffic control

The aim of the work presented in this article was to made and implement original computer software made in the LabVIEW environment. That program automate the measurement of emissions of magnetic disturbances coming from rolling stock. It is dedicated for oscilloscope card and RSAL 5340, RSAH 5324 rolling stock antennas for axle counter. The indicated algorithms of proceeding coming directly from the standards, additional own methods of fast data analysis was made. Communication between the measurement cards and computer using USB with self-power USB hab was used. The software is fully compatible with the requirements contained in the ERA/ERTMS/033281.

1. The general background

The growing demand for the comfort and diagnostic capabilities of rail vehicles has resulted in the need for a wide use of electronics. At the same time, traffic control devices are changing along with the development of the railway infrastructure. These are both modern station systems, line blockades and train detection devices. The increasingly complex rolling stock is a source of potential interference that may affect the operation of rolling stock detection devices [1–3]. The issue of ensuring the interoperability of rolling stock and railway infrastructure is important for the implementation of a single *European Railway Traffic Management System* – ERTMS, and as part of it, for the dissemination of the use of the *European Train Control System* – ETCS safe train control system.

A number of different types of track vacancy meter systems are used on European railways, operated by only one or more infrastructure managers, while rolling stock is usually prepared and released for operation over a larger area of the European rail network, which causes a significant complexity of the compatibility problem [4]. Determining the permissible levels of interference for individual frequencies in the operating band of rail sensors is the subject of the so-called frequency management process, covered in particular by the European standardization activity.

Before new rail vehicles are allowed to operate, verification of their *Electromagnetic Compatibility* – EMC with rail traffic control devices is carried out. One of the element of the research is the assessment of disruptive variable magnetic fields produced by the rolling stock. In terms of the subject matter of this article, the main document defining the requirements for rolling stock is ERA/ERTMS/033281 [6], which presents, i.e., the limits of magnetic field strengths for AC traction and the method of measuring these fields. Example of measurements results to previous of the document are presented in [7]. It is worth mentioning that the authors of this work are asked if the research methodology according the two documents ERA/ERTMS/033281 and CLC/TS 50238-3 is good enough for confirming compatibility of rolling stock with train detection systems. These documents do not take into account the case where two trains pass each other near the wheel counters.

As representatives of the Łukasiewicz Research Network – Poznan Institute of Technology (Ł–PIT),

[*] Corresponding author: bartlomiej.nagorny@pit.lukasiewicz.gov.pl (B. Nagórny)

Radio Technologies and Electromagnetic Compatibility Laboratory we have created a portable measuring stand for testing magnetic fields generated by railway vehicles, regardless of their power supply method.

2. Theoretical basics

2.1. Research on magnetic fields generated by rolling stock

In accordance with the requirements of the CLC/TS 50238-3 document [3], the measurements of the magnetic fields generated by rolling stock should be carried out with an antenna with standardized dimensions (length 15 cm, width 5 cm and height 5 cm) independently for three measurement planes: X, Y, Z (Fig. 1).

Fig. 1. Rail-mounted measuring antenna with the indicated directions of the plane

The limit values for the magnetic field strength from traction vehicles are defined for three frequency ranges:

- 27 – 52 kHz
- 234 – 363 kHz
- 740 – 1,250 kHz

The values of the limits for all separated axes are defined in table 10 of the ERA ERTMS document [6].

Łukasiewicz Research Network – Poznań Institute of Technology has measuring equipment that meets the applicable European requirements for this type of research. Our portable test bench consists of:

- two measuring antennas (Schwarzbeck RSAL 5340 and RSAH 5324), each with three output signals for X, Y, Z planes
- laptop (Lenovo, ThinkPad)
- three oscilloscope cards with USB communication (PicoScope series 4000)
- self-powered USB hub (D-Link)
- own measurement and data analysis software (PPM_210820_1.1.8.vi)

Test set-up for magnetic fields measurements in accordance with standard is shown in Fig. 2.

Fig. 2. Set-up for magnetic fields measurements

The voltage values induced in the antennas are registered by three oscilloscope cards with sample interval 400 ns and sensitivity of voltage measurement 500 mV. Each card has two inputs channels and one output channel for signal generator which was not used for measurements. The registration results are saved on the measurement computer, where the next analysis is carried out in accordance with the ERA/ERTMS/033281 guidelines, using dedicated, own software. The result of this analysis are the characteristics of the intensity values of the magnetic fields strength as a function of frequency, compared with the limit values for each of the measured planes.

2.2. LabVIEW software

A graphical development environment for data acquisition, analysis, and presentation from National Instruments is called LabVIEW (Laboratory Virtual Instrument Engineering Workbench). The main difference between LabVIEW and other applications like C or Pascal is that LabVIEW does not use text-based languages to create lines of code. LabVIEW uses a graphical programming language, G, to create programs in block diagram form. LabVIEW programs appearance and operation imitate physical instruments, such as oscilloscopes and multimeters because of that this programs are called virtual instruments. LabVIEW contains a comprehensive set of tools for acquiring, analyzing, displaying, and storing data, as well as tools for debugging.

All LabVIEW programs have a front panel and a block diagram. The front panel is the graphical user interface. This interface collects user input and displays program output. The front panel can contain knobs, push buttons, graphs, and other controls and indicators. The block diagram contains the graphical source code of application. In the block diagram one can program an application to control and perform functions on the inputs and outputs created on the front panel. The block diagram can include functions and structures from the built-in LabVIEW libraries. It also can include terminals that are associated with controls and indicators created on the front panel [5].

The front panel of application generating sine wave is shown in Fig. 3, its block diagram is shown in Fig. 4.

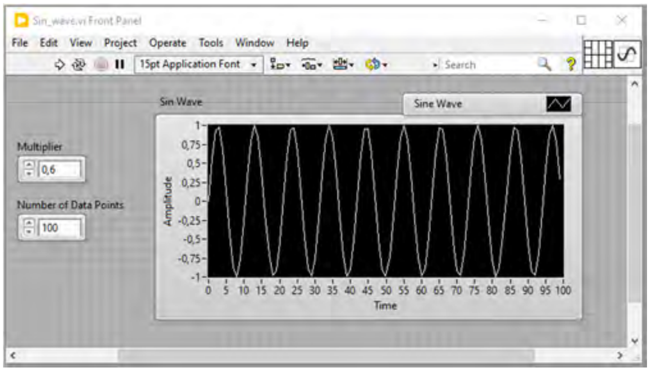

Fig. 3. Front panel of LabVIEW application

3. Measurement application

3.1. General information

The **PPM** is a software application for capturing and evaluating EMC signals fully developed in Ł–PIT. The design of the measurement application is based on the Laboratory's many years of research experience and made according to ERA/ERTMS/033281 requirements. After loading the main program window appears (see Fig. 5). All menus are programmed as easy as possible. During start up the USB devices are checked. A message box will appear if some USB devices are not connected correctly. Before reconnection the operator should check correct cabling including the connection cables to the USB hub.

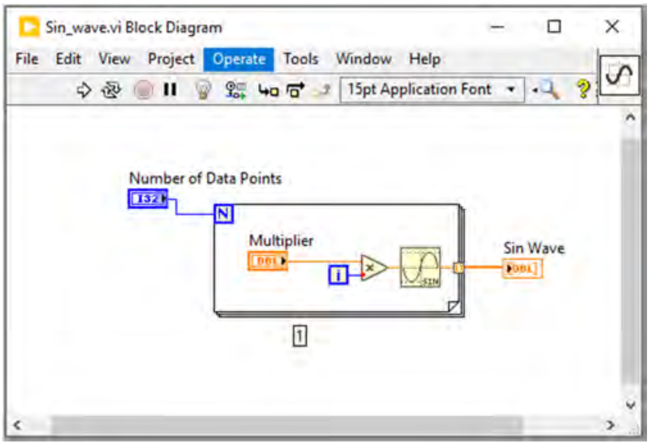

Fig. 4. Block diagram of LabVIEW application shown in Fig. 3

The program is divided into three tabs:

– Description
– Acquisition
– Results

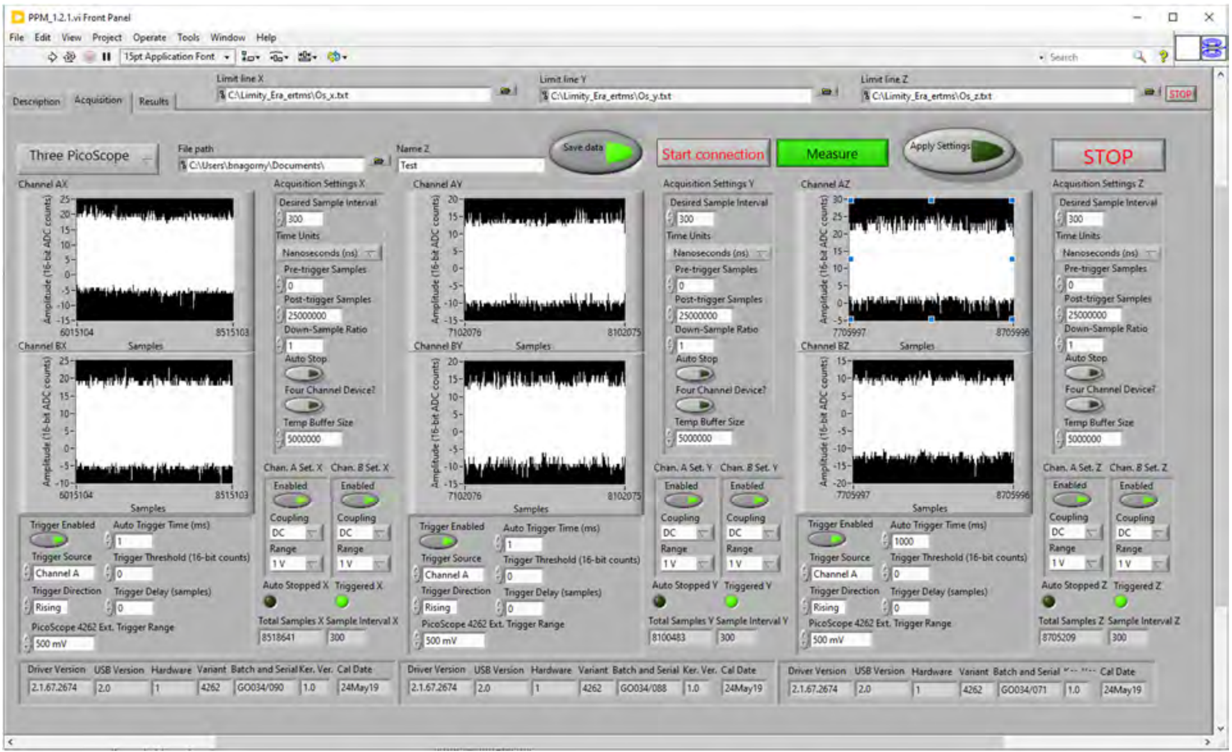

Fig. 5. Program panel – view of the acquisition mode

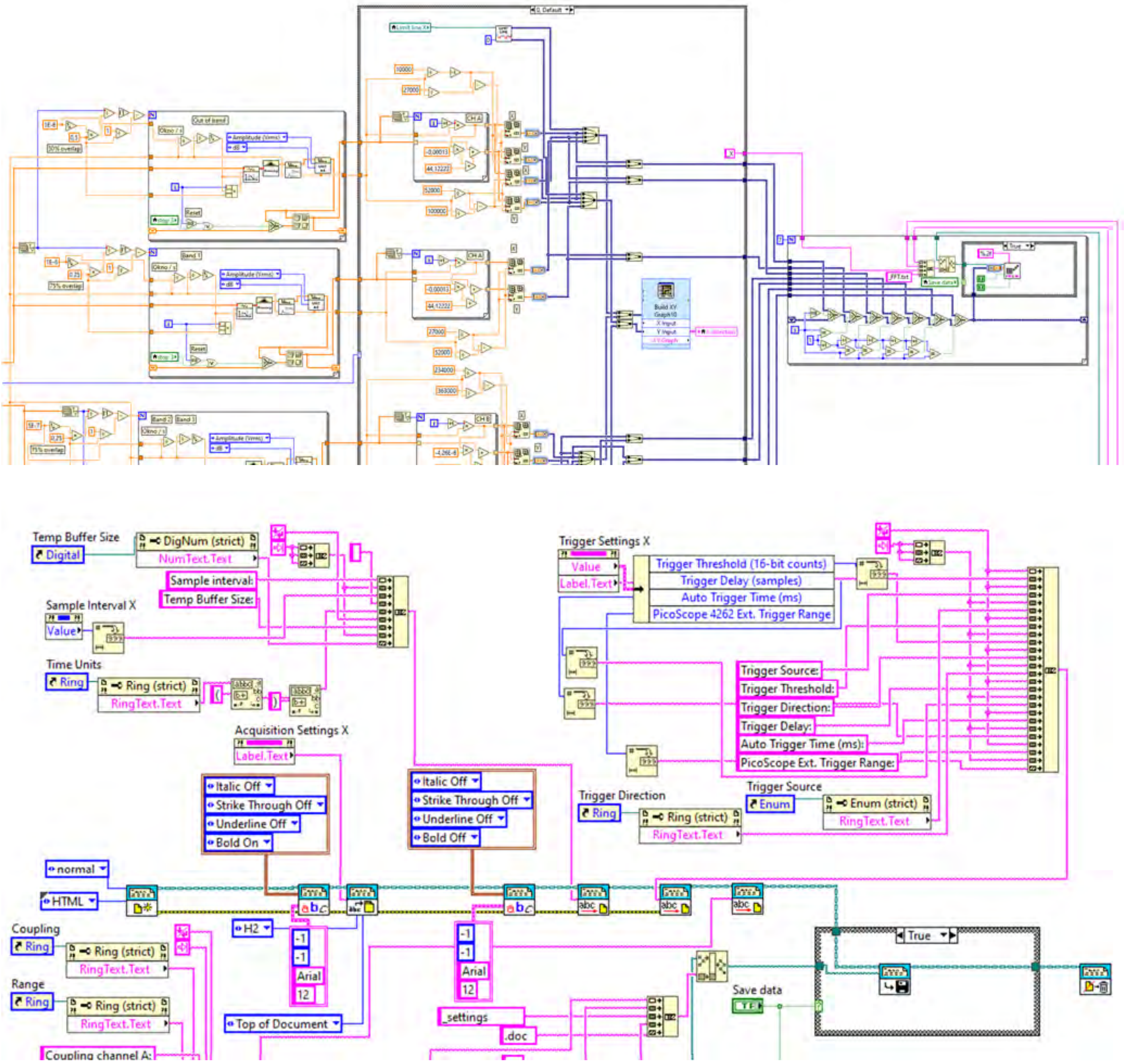

Fig. 6. Part of the block diagram of LabVIEW application shown in Fig. 5

In **description** part general information about functionality of the application are describe.

The screenshot of the **PPM** software for capturing and evaluating EMC signal panel is shown in the Fig. 5. The part of the block diagram of our software is shown in Fig. 6.

3.2. Acquisition mode

The main menu **acquisition** shows all important parameters. Each time when application is run a default parameters are set. In the main window the parameters can be changed. Approval of the new settings is done by pressing the button “Apply Settings”.

The huge memory of each sampling devices (Pico Scope) samples the whole data into the internal buffer. After the data will be transferred and store to the local or external hard disk.

The connection with Pico Scope is initialize after pushing button “Start connection”. Pushing button “Measure” will start measurement. Pushing button “STOP” will stop measurement.

The measurement results (raw data) are directly stored as a txt file. Each axis (x, y and z) is stored in a separate file with the extension *.txt. The saving path of the data can be pre-configured in the acquisition section of the application. The measurement settings are saved as a doc file separate for each axis.

3.3. Results mode

The main part of the **results** panel are the measurement visualization components, on which the data appears after the finished measurement.
On the graphs are shown the broadband evaluation using *Fast Fourier Transformation* – FFT with *Hanning window (green lines)*. The result are presented for each axis in a separate graphs. The Figure 7–9 shows the result of many thousand FFT during 15 s sampled data. The analyzed data are directly stored as a txt file in three separate file for each axis. The saving path is the same like for measurement raw data.

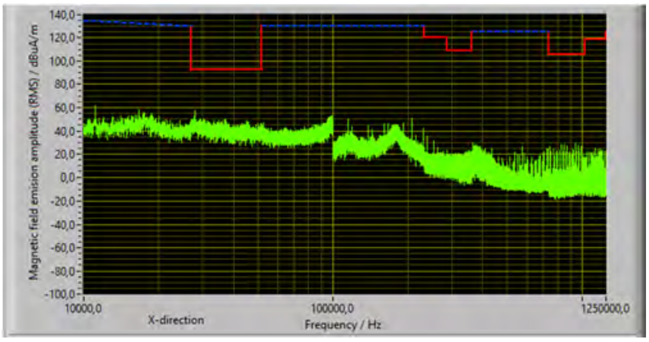

Fig. 7. Program panel – view of the results mode for X-axis

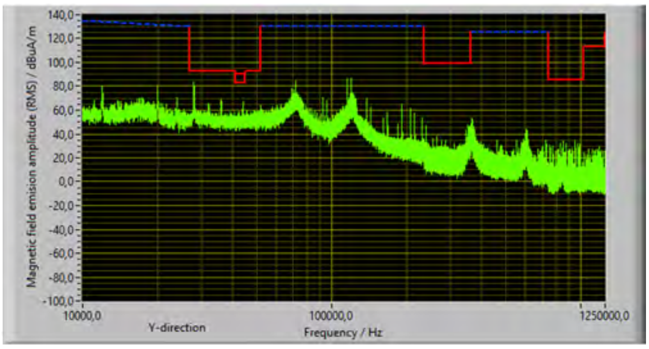

Fig. 8. Program panel – view of the results mode for Y-axis

Blue dash line indicate out of band region where FFT with Hanning window, 50% overlap is used as evaluation method. Red solid line indicate in-band limits. These regions are demonstrated by broadband evaluation using FFT with Hanning window, 75% of time overlapping and time windows of 1 ms for Band 1, 0.5 ms for Band 2 or Band 3. More details are provided in the document ERA ERTMS [6].

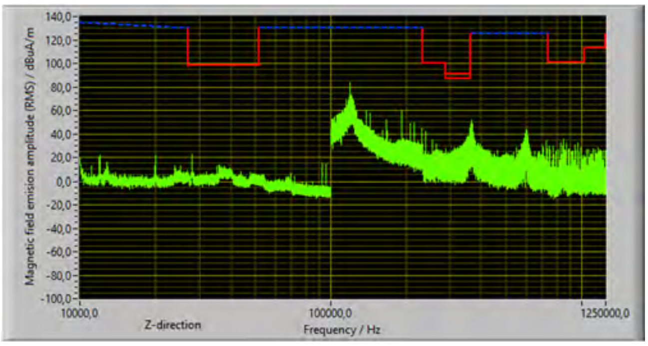

Fig. 9. Program panel – view of the results mode for Z-axis

The visible discontinuities in the spectra in Fig. 7 and Fig. 9 are the result of different mounting of the two antennas on the rail, resulting from different positioning tolerances for each of the antennas.

3. Summary

The aim of work described in present article was to create software for the measurement of magnetic field emission for railway applications. The applications were created by use of LabVIEW (version 2020 SP1) graphical development environment. This choice was dictated by the universality of the libraries available in LabVIEW, which ensure relatively easy communication with the majority of electronic measuring devices operating on the market. Additionally, creating an application in LabVIEW environment does not need advanced programming skills.

The PPM program is fully compatible with the requirements contained in the ERA/ERTMS/033281. The main advantage of our program is possibility of easy modification following the changes in [6]. This is not provided by the commercially available programs.

The program created within this work were put into practice in Radio Technologies and Electromagnetic Compatibility Laboratory at Łukasiewicz Research Network – Poznan Institute of Technology, Poland.

Acknowledgements

This work was partially funded by National Research and Development Center and PKP Polish Railway Lines – Project EMC4CCS BRIK No. POIR.04.01.01-00-0021/17.

Nomenclature

ERTMS	European Railway Traffic Management System
ETCS	European Train Control System
EMC	Electromagnetic Compatibility
LabVIEW	Laboratory Virtual Instrument Engineering Workbench
FFT	Fast Fourier Transformation
Ł –PIT	Łukasiewicz Research Network – Poznan Institute of Technology

Bibliography

[1] CLC/TS 50238-1 Railway applications – Compatibility between rolling stock and train detection systems - Part 3: General. 2020.

[2] CLC/TS 50238 Railway applications – Compatibility between rolling stock and train detection systems – Part 2: Compatibility with track circuits. 2020.

[3] CLC/TS 50238-3 Railway applications – Compatibility between rolling stock and train detection systems – Part 3: Compatibility with axle counters. 2019.

[4] Directive 2014/30/EU of the European Parliament and of the Council on the harmonization of the laws of the Member States relating to electromagnetic compatibility. 2014.

[5] Getting Started with LabVIEW 2020 Community Edition 2020.

[6] Interfaces between control-command and signalling trackside and other subsystems – ERA/ERTMS/033281. 2018 v. 4.0.

[7] Olejniczak T., Woźniak K., Kowalski M. Test of rolling stock compatibility with axle counters. *Rail Vehicles/Pojazdy Szynowe* 2017, 3, 61-65. https://doi.org/10.53502/RAIL-138450

Article citation info:
Pielecha I., Dimitrov R., Mihaylov V. Energy flow analysis based on a simulated drive of a hybrid locomotive powered by fuel cells. *Rail Vehicles/Pojazdy Szynowe*. 2022, 1-2, 68-76. https://doi.org/10.53502/RAIL-152703

Rail Vehicles/Pojazdy Szynowe

www.railvehicles.eu

Energy flow analysis based on a simulated drive of a hybrid locomotive powered by fuel cells

Ireneusz **Pielecha** [a, *], Radostin **Dimitrov** [b], Veselin **Mihaylov** [c]

[a] *Institute of Combustion Engines and Powertrains, Poznan University of Technology, Poznan, Poland*
[b] *Dept. Transport Engineering and Technologies, Technical University of Varna, Varna, Bulgaria*

ARTICLE INFO

Received: 25 July 2022
Revised: 8 August 2022
Accepted: 9 August 2022
Available online: 9 August 2022

KEYWORDS

rail vehicles
energy flow
hybrid vehicles
fuel cell simulation
high voltage battery

Implementation of hybrid drives in rail vehicles is a solution aimed at limiting the negative environmental impact of transport. The use of fuel cell systems is a contemporary trend in the development of locomotives. The paper presents an energy flow analysis in a hybrid locomotive powered using fuel cells. The parallel hybrid drive system consisted of fuel cells, batteries and an electric motor. The simulations and analyzes were performed with the use of AVL Cruise M software. A simulated route, with a length of approximately 300 km, was used as basis for the analysis, taking into account a typical speed profile of a locomotive in passenger traffic. The energy flow and consumption values were estimated, and mean hydrogen consumption values were determined.

1. Introduction

The number of locomotives powered by electricity has increased in recent years. In 2019, diesel was used as the main source of propulsion for locomotives only in Estonia, Latvia and Lithuania [10]. Electricity was the main source of power supply for traction vehicles (except locomotives) in Spain (87.4%), France (78.7%), Latvia (76%), Austria (72.9%), Poland (87.7%), Portugal (78.6%) and Sweden (96.8%) [10].

The densest rail networks in the EU in 2019 could be found in regions of Germany and the Czech Republic such as: Berlin (698 km/1000 km^2) and Prague (491 km/1000 km^2). High rail network densities (of about 120 km/1000 km^2) were also recorded in other regions of the Czech Republic, Germany, the Netherlands and Poland – Fig. 1.

Implementing hybrid drives for use in rail vehicles is a trend that allows the reduction of the negative environmental impact of the transport sector. The share of hybrid drives in rail vehicles rose to approximately 4,900 units in 2020 and a further increase to 8,400 units is expected to take place by 2030 (this is an annual increase of approximately 5.5%) [13, 16].

Some companies, including: Alstom, Bombardier, Siemens, Wabtec Corporation and others, are investing in the development of trains powered by alternative fuels. Alstom was one of the first companies to present a locomotive with PEM (Proton Exchange Membrane) fuel cells powered by hydrogen fuel [4]. The hybrid battery-hydrogen system was equipped with fuel cells with a capacity of 400 kW and batteries with a capacity of 111 kW and an operational voltage of 800 V. Each of the traction motors had a power of 314 kW. Hydrogen was stored in special tanks with a hydrogen mass capacity of 2 × 94 kg at a pressure of 35 MPa [20]. In March 2018, Alstom received two orders for a total of 25 Coradia Lint hydrogen regional trains in southern Germany. As of today, these trains operate among others in: Italy, France, the Netherlands, Sweden and Austria [5]. In September 2018, Bombardier launched their own new Electro-Hybrid Train called Talent 3 [17].

The Japanese proposal for a hybrid drive rail solution with fuel cells was the HYBARI project, which was the result of cooperation between Toyota, Hitachi and the Japanese railways (JR East – East Japan Railway Company) [14, 15]. The vehicle uses two electric motors with a power of 95 kW each and a stack of

* Corresponding author: ireneusz.pielecha@put.poznan.pl (I. Pielecha)

PEM fuel cells (four cells with a power of 60 kW) forming a Toyota Mirai module, and are supplemented by two Li-Ion batteries with an energy storage capacity of 2 × 120 kWh.

In Poland, the Corantia iLint locomotive was first presented in 2021 [8]. It is assumed that replacing one regional diesel train with a hydrogen train would result in the equivalent of retiring 400 cars from regular traffic on the roads [5].

Siemens offers the Mireo Plus H vehicle which runs on a battery-hydrogen drive. The system uses 200 kW fuel cells from Ballard. The vehicle range is estimated to be 600 km (for the two-unit system) and 1000 km (for the three-unit system) [22].

There are currently several projects for the use of fuel cells in various forms of transport:

1. IMMORTAL (IMproved lifetiMe stacks fOR heavy-duty Trucks through ultrA-durabLe components); a project focusing on the development of fuel cells and their applications in heavy-duty vehicles
2. Flagships; a project to build a cargo ship powered by fuel cells
3. FCH2RAIL (Fuel Cell Hybrid Power Pack for Rail Applications); a project in which Belgium, Germany, Spain, Portugal and Toyota (as a supplier of fuel cells) participate to develop a zero-emission locomotive propulsion system
4. H2Haul (Hydrogen fuel cell trucks for heavy-duty, zero-emission logistics); testing of 16 heavy-duty vehicles equipped with fuel cells.

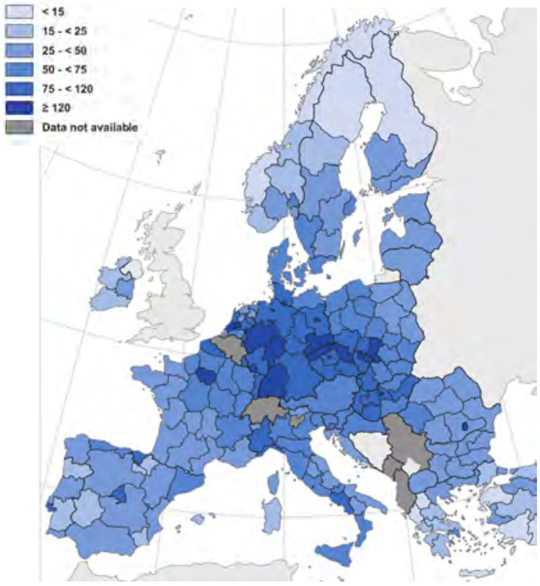

Fig. 1. European railway lines density in 2019 (in km of railway line per 1000 km^2) [10]

2. Fuel cells in rail vehicles

Using fuel cell systems to power locomotives is a fairly modern trend in their development. Low-temperature fuel cells are the ones most often used in transport means as a power source for electric motors [19]. In fuel cell (FC) systems, batteries are a necessary systems used for powering the fuel cells (in the first phase of their operation) and to generate supplementary power when driving in dynamic conditions, along with supercondensator (SC) due to their much higher power density values compared to batteries (BAT) [7, 11]. Research with the use of SC + BAT + FC conducted for vehicles of various classes (tram, passenger train, light rail vehicle, locomotive – tram, passenger train, railcar and freight locomotive) allowed for the optimal selection of power sources and energy storage [11, 12].

Simulation tests of hybrid rail vehicle systems with fuel cells can prove to be a significant source of information about the energy flow. Such studies enable the assessment of energy and hydrogen consumption in a locomotive traveling on a simulated route [1]. The simulation model presented in [1] included five modules: batteries, fuel cells, vehicle dynamics, power distribution and a controller. SOFCs (solid oxide fuel cells) require much higher temperature values to ensure their proper operation (to enable the flow of ions through the electrolyte). One of the proposals is a SOFC system with a Brayton turbine and a Rankin cycle [3]. Such a solution has made it possible to obtain an overall system efficiency of about 80%, while the efficiency of the cell itself was between just 45% and 65% [23]. The constant pressure to reduce the consumption of energy and fuel (including hydrogen) leads to optimization works in the field of eco-driving of such drives [6, 18], and the potential use of ammonia to power SOFC cells [2].

3. Aim of research work

The aim of the conducted research was to analyze the energy flow in the hybrid drive system of a locomotive equipped with fuel cells and high-voltage batteries. The analysis was performed on a typical route simulating traffic at speeds of up to 130 km/h. Energy consumption by drive systems and hydrogen consumption were all determined. The presented model enables the analysis and evaluation of hydrogen consumption on typical routes serviced currently by diesel locomotives.

4. Research method

4.1. Drive system model

The simulation test drives were carried out with the use of AVL Cruise M software. This software enables the simulation of energy flow processes in propulsion systems, including hybrid drives.

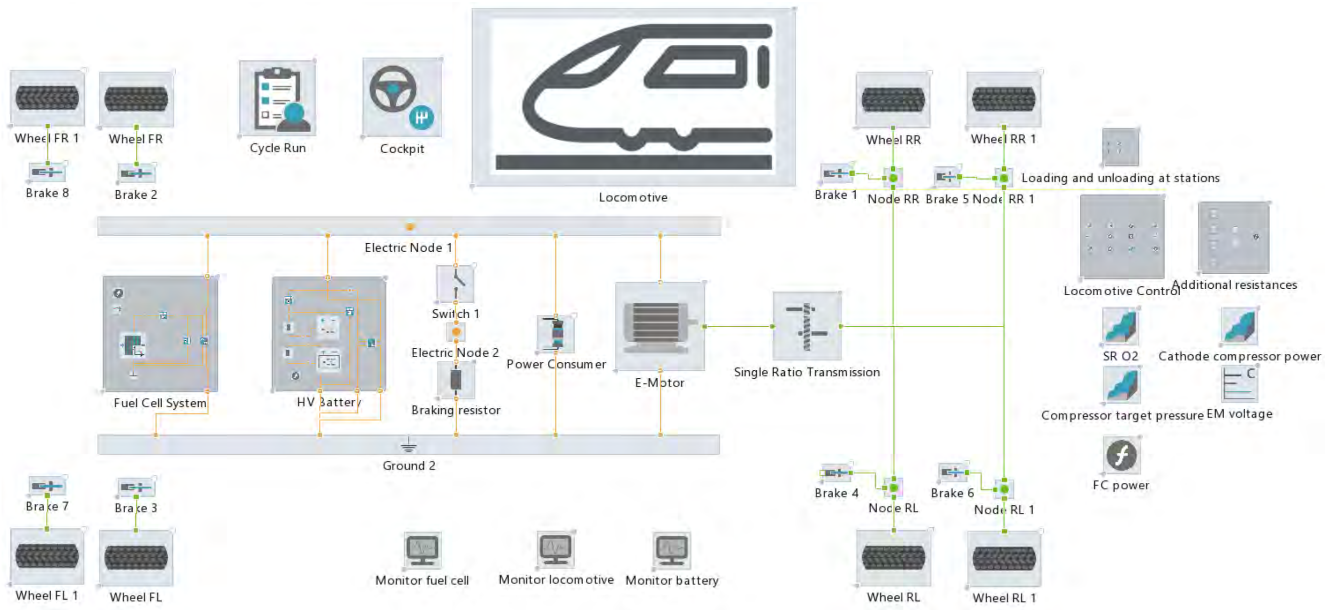

Fig. 2. Locomotive drive system model

The article presents an energy flow simulation in a locomotive (without carriages) that was equipped with fuel cells, batteries and an electric motor (Fig. 2). Some of the data included in the model was based on other papers [9, 21].

The locomotive, weighing 80 tons (Table 1), was equipped with an electric motor with a power of 2,600 kW. As shown in Fig. 2, the torque is transferred from the drive to the two axles. A low-temperature fuel cell system with a capacity of over 3 MW was connected in parallel to two batteries (connected in series) with a capacity of 1.7 MW as well as two DC-DC voltage converters. The fuel cell operated at a voltage of 4000–5000 V, the battery at about 2000 V and the electric motor at about 2000 V. Additionally, a braking resistor (power consumer) was included in the

Table 1. Technical data of locomotive

Locomotive		
Distance from hitch to front axle	m	16
Wheel base	m	12
Height of support point at bench test	m	0.5
Distance from point of force application to front axle	mm	4000
Curb weight	t	80
Gross weight	t	90
Reference vehicle for driving resistance		
Frontal area	m^2	10
Drag coefficient	–	0,75
Weight	t	82
Transmission ratio	–	5.5
Mass properties		
Moment of inertia	kg m^2	50
Wheel properties		
Friction coefficient of tire	–	0.7
Reference wheel load	kN	100
Wheel load correction coefficient	–	0.01
Rolling radius		
Static	mm	546
Dynamic	mm	550

system. It was activated when the braking power was greater than a specified maximum regenerative power. The locomotive had a wheelbase of 16 m and was equipped with a permanent gear with a ratio of 5.5 between the electric motor and the wheels. The function of resistance to motion is described by:

$$F = A + B \times V^2 \tag{1}$$

where: a = 143 N, b = 03399 N/(km/h)^2, V – driving speed in km/h.

4.2. Scope of research

The energy flow tests were carried out on a regular locomotive route with a travel distance of 328 km. The simulation runtime was 14,225 s. The tests were carried out taking into account the locomotive mass of 82 t. The analysis covered the operating conditions of the fuel cell, the high-voltage battery and the electric motor. An analysis of energy flow, energy recuperation, and average energy consumption per 100 km was carried out.

5. Hybrid drive system with fuel cells

5.1. Fuel cells operating conditions

In the simulation model, 4,500 individual fuel cells with a total cell area of 2,720 cm^2 were used. The technical parameters of the fuel cell model were included in Table 2.

Because it is necessary to adjust the voltage value of the cells stack and the electric motor, the stack of fuel cells was connected to a DC-DC voltage converter (at 95% efficiency) (Fig. 3).

Table 2. Technical data of fuel cell

Number of cell	–	4500
Cell area	cm^2	2720
CCL proton conductivity	A/(V cm)	3
Ideal open circuit voltage	V	1,23
Cat. layer thickness	cm	0.001
GDL thickness	cm	0.025
Maximum current	A	2500

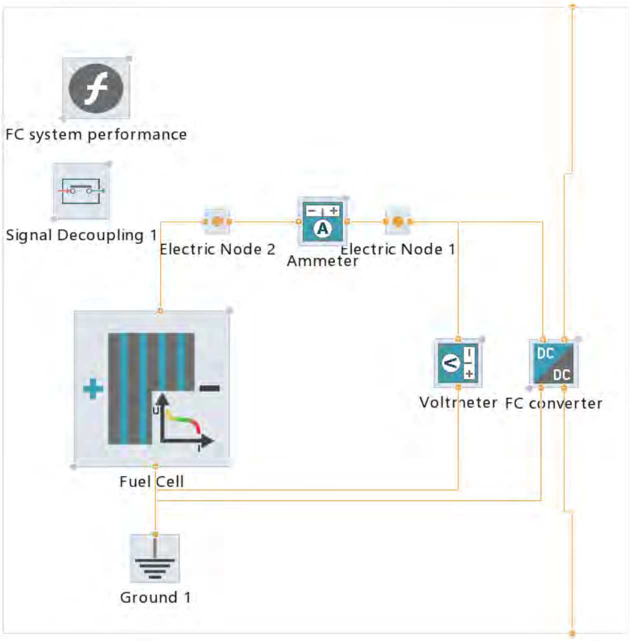

Fig. 3. Fuel cell model with measurement conditions and DC-DC voltage converter

The characteristics of the fuel cell stack used were shown in Fig. 4. The maximum power value was obtained with a current of about 1 kA. The cell voltage was limited to approximately 3.2 kV with these operating parameters. The operating temperature range of the cell stack was 30–80°C, at an air pressure of 1 bar and a humidity of 70%.

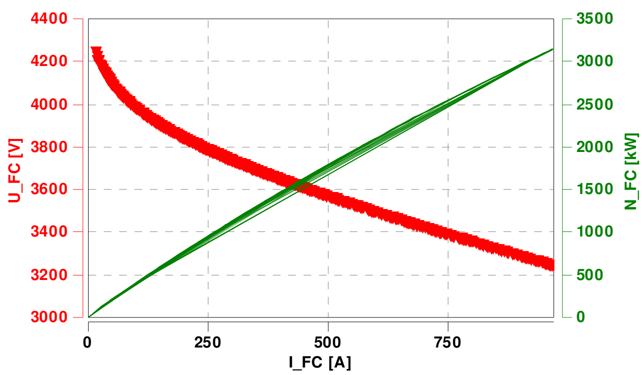

Fig. 4. Current-voltage characteristics of the fuel cell stack

5.2. Battery operating conditions

The locomotive system used two battery modules connected in series (Fig. 5). Each battery consisted of 4 rows of 262 cells connected in series. The cell voltage value was in the range of 3–5 V. The full specification of the battery cells was included in Table 3.

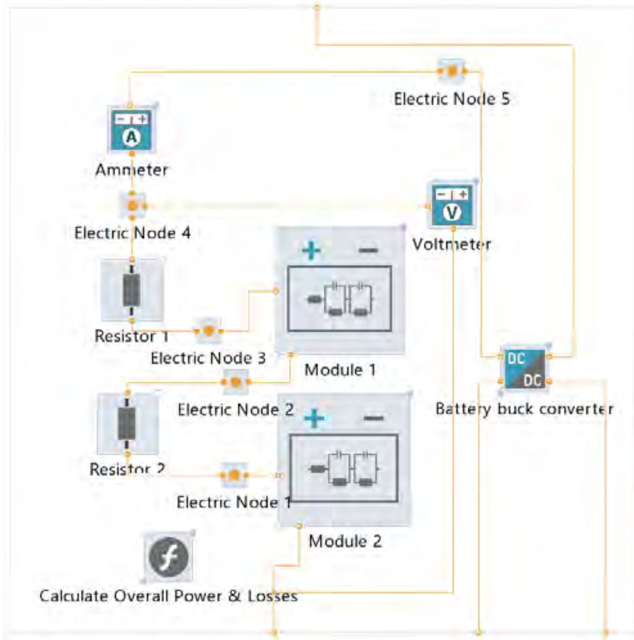

Fig. 5. Model of a high voltage batteries connected in series with a DC-DC voltage converter

Table 3. Technical data of battery

Number of cell per cell-row	–	262
Number of cell-rows	–	4
Minimum voltage	V	3
Maximum voltage	V	5
Maximum charge	Ah	25
Initial charge	%	60

The characteristics of a single battery cell were shown in Fig. 6. Assuming the battery state of charge (SOC) was in the range of 20–80%, the battery voltage was found to be in the range of 3.6–4.0 V.

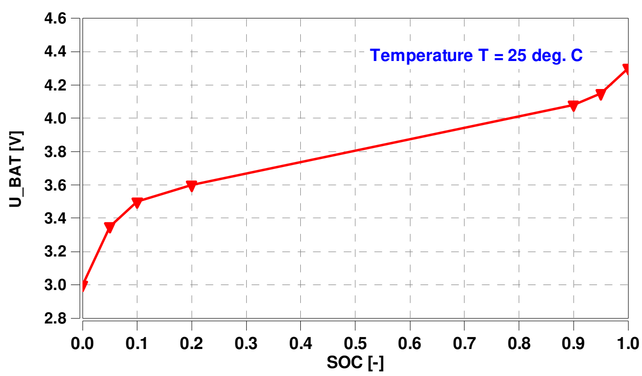

Fig. 6. Characteristics of the battery cell voltage depending on its charge level

The characteristics of resistance changes were shown in Fig. 7. It was assumed that these values during the battery charging and discharging were the same.

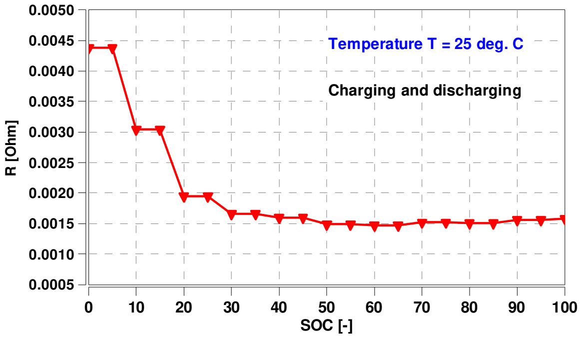

Fig. 7. Characteristics of the cell's resistance during charging and discharging

5.2. Electric motor operating conditions

The system used an asynchronous electric motor design operating in two quadrants (the first and the fourth). The torque characteristics were shown in Fig. 8. The maximum value of the torque was maintained up to the speed of 3000 rpm. The maximum engine speed was 7500 rpm. The engine was characterized by high efficiency values (over 90%) in the range of 2200–2500 rpm. When acting as a generator, however, the motor efficiency does not exceed 80%.

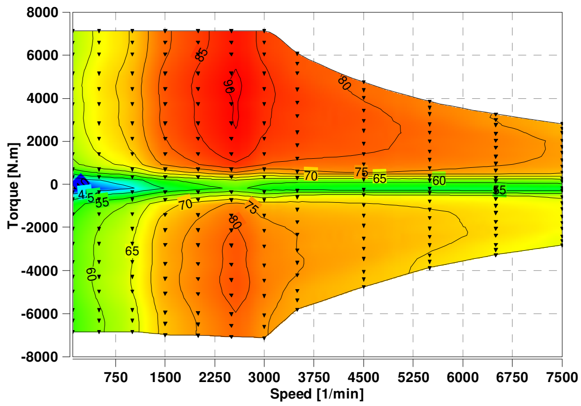

Fig. 8. Electric motor torque characteristics

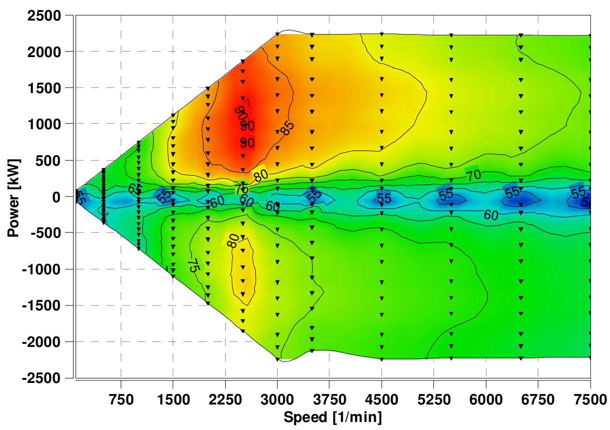

Fig. 9. Electric motor power characteristics

The electric motor power characteristic (Fig. 9) indicates constant power values in a fairly large range of rotational speeds. The maximum power of 2,240 kW can be obtained at a speed of 3,000 rpm.

5.3. Energy flow analysis

The route, simulated in the AVL Cruise M software, was used to analyze the energy flow. The 328 km route connects Helsingor in Denmark with Karlskrone in Sweden. The duration of the trip was 3 h 57 min. The maximum speed of the locomotive was 120 km/h. The driving speed profile of the locomotive was shown in Fig. 10.

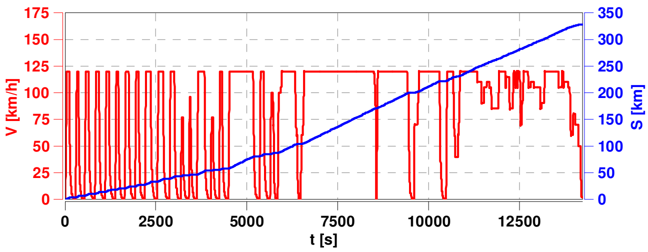

Fig. 10. Locomotive speed profile along with the distance covered

The data in Fig. 10 shows that the initial route was characterized by frequent stops. Longer sections of uniform drive speed can be found in the central part of the route. The final part of the route consisted of varying driving speeds, but without stopping the locomotive. As the profile shows, the first 30% of the route distance was covered more slowly, with frequent locomotive from stops. On the remaining 70% of the route the locomotive was travelling at a nearly constant speed. The mean travel speed was calculated to be about 83 km/h.

The values of the locomotive traction force and the power loss were also determined. These values were compiled into Fig. 11. The data shows that the average, maximum traction force was about 100 kN. The instantaneous, maximum power losses were measured at about 200 kW (the mean values results were determined by analyzing only the peaks of the values in Fig. 11).

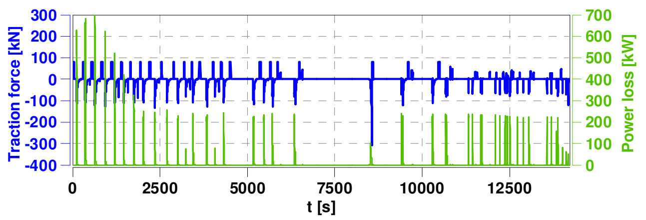

Fig. 11. Locomotive traction force and power loss

Because the fuel cell is the main source of the locomotive's propulsion, its power was more than twice that of the batteries. The operating conditions of the fuel cell were shown in Fig. 12. The frequent change of the locomotive travel speed caused the cell current intensity to jump up to about 1000 A at certain points. As a result, the voltage drops to about 3200 V. Idle operation of the fuel cell (not providing power) caused the voltage to reach its maximum value. At steady speeds (approx. 120 km/h), the power drawn from the fuel cell was measured at 180 kW. The power drawn from the battery, however, was only 11 kW.

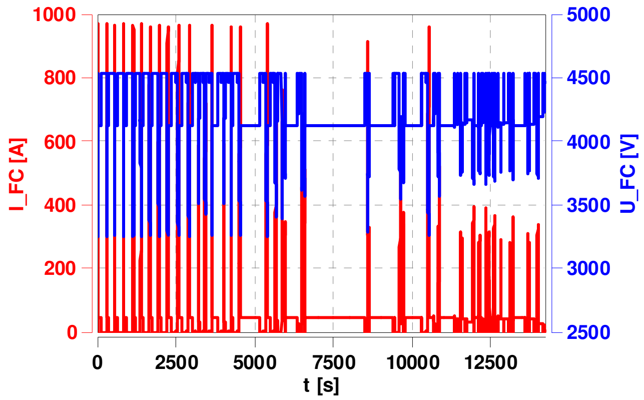

Fig. 12. Fuel cell operation characteristic when travelling on the simulated route

The drive system characteristics indicated that the maximum instantaneous power of the fuel cell stack reached 3 MW. About 1 MW of power was used in the final phase of the route, without stops but with a changes in travel speed. The total fuel cell energy value in the simulation was estimated at 0.875 MWh (Fig. 13).

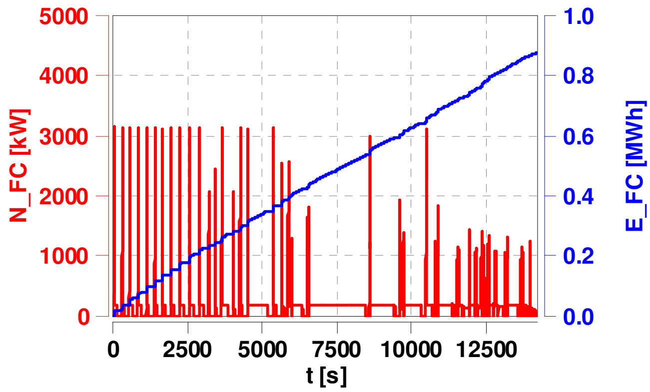

Fig. 13. The fuel cell power characteristics and its total energy consumption on the simulated route

A detailed analysis of a single acceleration (Fig. 14) after the locomotive stopped showed an almost two-fold decrease in the fuel cell voltage, with an increase in the current consumption to about 1000 A. This was mirrored by a slight decrease in the battery SOC. Subsequent locomotive braking caused this value to be greater (SOC = 0.61) than before braking (SOC = 0.60). This means that when the locomotive brakes, it was possible to increase the SOC by 1%.

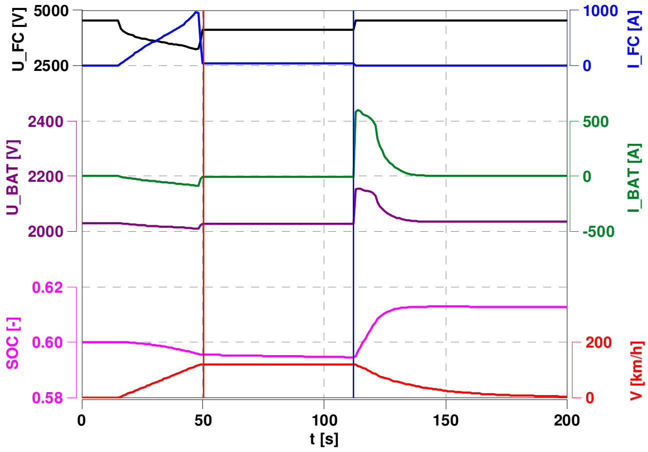

Fig. 14. Analysis of an individual speed profile change, including acceleration, constant speed and braking until the locomotive came to a stop

The voltage-current characteristic of the battery has shown much higher current values used during braking than during acceleration (Fig. 15). As the current value increased, the voltage value also increased. The density of test points increased at points of vehicle acceleration and braking. The characteristics in Fig. 15 show that the same current values (positive during braking and negative during acceleration) meant that the respective power values may be higher when the locomotive was braking. During braking, the voltages were found to be about 10% greater than the corresponding voltages during acceleration of the rail vehicle.

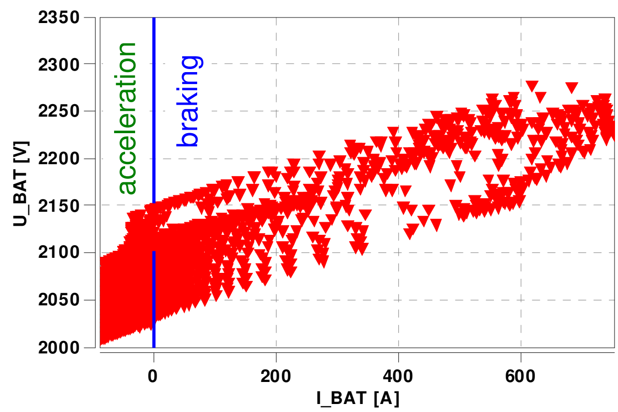

Fig. 15. Battery current-voltage characteristics

Analyzing Figs 14 and 15 indicated low values of the battery current used to drive the locomotive. Much higher currents (about 8 times) were used during braking of the vehicle. The highest currents occurred in the initial braking phase (Fig. 14) with the highest voltage values occurring at the same time. Under such conditions, the maximum recovered power was approximately 1.7 MW.

The battery characteristics indicated its continuous recharging for the whole driving profile. This is due to an increase in the battery voltage (Fig. 16). The value of the current during the constant driving speed was about 200 A. Such values were obtained during the test time t = 7500 s. Each braking with the rail vehicle increased the charging current. The driving profile showed that the battery voltage increased by 110 V during the 320 km trip, which resulted in an increase in the battery charge level from 60% to over 90% (Fig. 17).

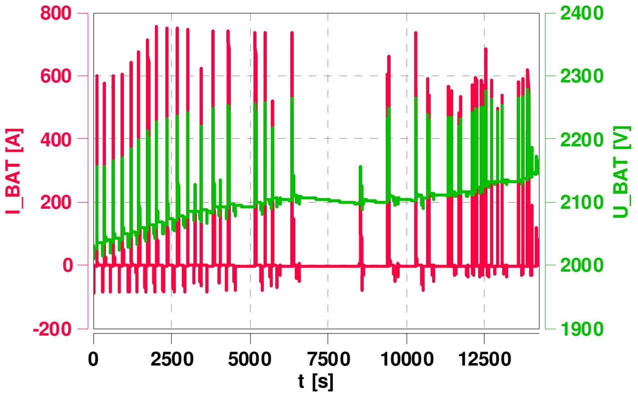

Fig. 16. Battery current-voltage characteristics for the simulated route

The maximum power drawn from the battery was about 1.8 MW (Fig. 17) when the locomotive was accelerating to a speed of 120 km/h. The value of the absolute increase in battery energy (including its discharge during acceleration) on the entire route was determined as 0.071 MWh (based on positive and negative current value from Fig. 16):

$$E\_BAT = I\_BAT \cdot U\_BAT \cdot \Delta t \tag{2}$$

Almost 50% of this energy was obtained after travelling just the first 30% of the route distance. Thus proving that the hybrid drive solution used was very efficient.

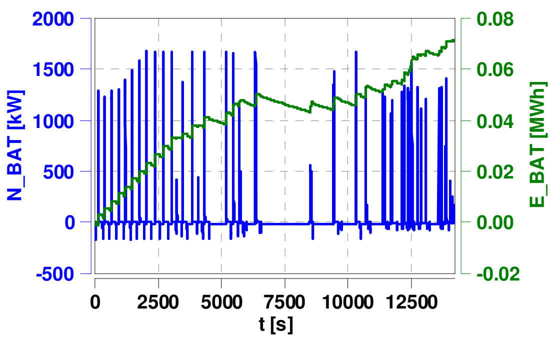

Fig. 17. Characteristics of battery power and total energy consumption throughout the simulated route

Although quite a large portion of the locomotive braking energy was recovered, the energy consumption of the fuel cell was nevertheless much higher and amounted to 0.875 MWh. The difference in energy consumption was therefore over 12 fold (Fig. 18).

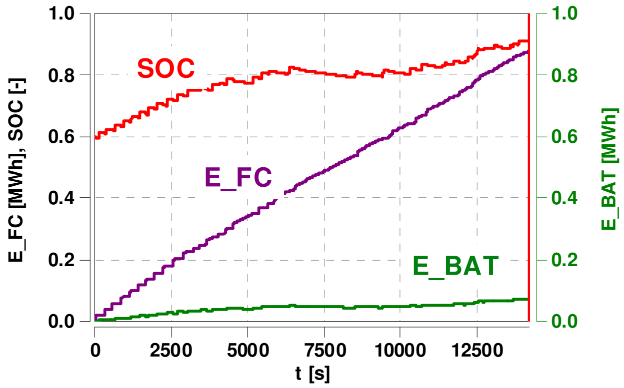

Fig. 18. Changes in energy consumption along with an increase in the battery charge level during the simulated journey

The hydrogen consumption during the fuel cell operation equaled 40.6 kg. Thus the average hydrogen consumption was 12.2 kg/100 km of the travel distance of a 82 t locomotive. Taking into account the energy used by the fuel cells and the energy recovered by the battery, then an average energy consumption value was of 245 kWh per 100 km of travel.

By taking into account the current values that were related to the battery power output, it is possible to determine the value of energy consumed by the battery.

The battery energy discharge value (only positive current value from Fig. 16 and eq. (2)) was 0.052 MWh.

This means that the energy recovery was 36% greater than the energy loss of the batteries for the locomotive drive (0.071 MWh/0.052 MWh × 100% = = 36%).

6. Conclusions

The AVL Cruise M simulation environment is a software that enables a complete analysis of the energy flow in the drive system of a hybrid electric motor, fuel cells and batteries.

Based on the performed analyses, it has been concluded that:

1. The hybrid drive system (fuel cell, battery and electric motor) can be an alternative to electric or diesel drive systems of locomotives and passenger trains on passenger routes. Hydrogen storage and transportation remain an issue, however.

2. The 82 t locomotive can be powered by a 2.2 MW propulsion system without losing its drive properties up to a speed of 120 km/h.
3. The average energy consumption value of a locomotive weighing 82 t was 245 kWh/100 km; fuel cell hydrogen consumption was 12.2 kg/100 km.
4. Recuperative braking of the locomotive increased the absolute value of the battery SOC; this remained true even after taking into account the battery power used to move the vehicle; the energy recovery for the batteries was 36% greater than the energy used to the locomotive drive.

Acknowledgements

This work has been done under AVL University Partnership Program.

Nomenclature

BAT	battery
CCL	cathode catalyst layer
DC	direct current
E	energy
EU	European Union
FC	fuel cell
GDL	gas diffusion layers
I	current
JR East	East Japan Railway Company
Li-Ion	Lithium-Ion battery
PEM	Proton Exchange Membrane
R	resistance
SC	supercondensator
SOC	state of charge
SOFC	solid oxide fuel cell
t	time
T	temperature
U	voltage
V	speed

Bibliography

[1] Akhoundzadeh M.H., Panchal S., Samadani E. et al. Investigation and simulation of electric train utilizing hydrogen fuel cell and lithium-ion battery. *Sustainable Energy Technologies and Assessments*. 2021, **46**, 101234. https://doi.org/10.1016/j.seta.2021.101234.

[2] Al-Hamed K.H.M., Dincer I. A new direct ammonia solid oxide fuel cell and gas turbine based integrated system for electric rail transportation, *eTransportation*. 2019, **2**, 100027, https://doi.org/10.1016/j.etran.2019.100027

[3] Al-Hamed K.H.M., Dincer I. A novel integrated solid-oxide fuel cell powering system for clean rail applications. *Energy Conversion and Management*. 2020, **205**, 112327. https://doi.org/10.1016/j.enconman.2019.112327

[4] Coradia iLint. A full emission-free train. http://aurich-bahn.de/wordpress/wp-content/uploads/2012/07/Coradia-iLint-Product-sheet.pdf

[5] Coradia iLint™ – the world's 1st hydrogen powered train. https://www.alstom.com/solutions/rolling-stock/coradia-ilinttm-worlds-1st-hydrogen-powered-train

[6] Deng K., Fang T., Feng H. et al. Hierarchical eco-driving and energy management control for hydrogen powered hybrid trains. *Energy Conversion and Management*. 2022, **264**, 115735. https://doi.org/10.1016/j.enconman.2022.115735.

[7] D'Ovidio G., Ometto A., Valentini O. A novel predictive power flow control strategy for hydrogen city rail train. *International Journal of Hydrogen Energy*. 2020, **7**, 4922-4931. https://doi.org/10.1016/j.ijhydene.2019.12.067

[8] Durzyński Z. Hydrogen-powered drives of the rail vehicles (part 1). *Rail Vehicles/Pojazdy Szynowe*. 2021, **2**, 29-40. https://doi.org/10.53502/RAIL-139980

[9] Engineering ToolBox – Resources, Tools and Basic Information for Engineering and Design of Technical Applications! https://www.engineeringtoolbox.com/rolling-friction-resistance-d_1303.html

[10] Eurostat. Road, rail and navigable inland waterways networks by NUTS 2 regions. https://ec.europa.eu/

[11] Fragiacomo P., Piraino F. Energy performance of a fuel cell hybrid system for rail vehicle propulsion. *Energy Procedia*. 2017, **126**, 1051-1058. https://doi.org/10.1016/j.egypro.2017.08.312

[12] Fragiacomo P., Piraino F. Fuel cell hybrid powertrains for use in Southern Italian railways. *International Journal of Hydrogen Energy*. 2019, **44**(51), 27930-27946. https://doi.org/10.1016/j.ijhydene.2019.09.005

[13] Gechev T., Punov P. Popular fuel cell types - a brief review. *60th Annual Scientific Conference – University of Ruse and Union of Scientists*. Sofia. 2021, 57-66. https://conf.uni-ruse.bg/bg/docs/cp21/4.1/4.1-13.pdf

[14] JR East, Hitachi and Toyota to develop hybrid (fuel cell) railway vehicles powered by hydrogen. 6.10.2020. https://global.toyota/en/newsroom/corporate/33954855.html

[15] JR East, Hitachi and Toyota to develop hybrid fuel cell trains. *Fuel Cells Bulletin*. 2020, **11**, 6. https://doi.org/10.1016/S1464-2859(20)30506-X

[16] Market Research Report. Hybrid Train Market by Propulsion Type (Electro Diesel, Battery Operated, Hydrogen, CNG, LNG, and Solar), Application (Passenger and Freight), Operating Speed (> 100 km/h,

100-200 km/h, < 200 km/h), Battery Technology, and Region – Global Forecast to 2030. August 2020. https://www.marketsandmarkets.com/Market-Reports/hybrid-train-market-238438631.html

[17] Owano N. Bombardier electric hybrid train to keep Germany's green ambitions on track. https://techxplore.com/news/2018-09-bombardier-electric-hybrid-germany-green.html

[18] Peng H., Chen Y., Chen Z. et al. Co-optimization of total running time, timetables, driving strategies and energy management strategies for fuel cell hybrid trains. *eTransportation*. 2021, **9**, 100130. https://doi.org/10.1016/j.etran.2021.100130

[19] Pielecha I., Engelmann D., Czerwinski J. et al. Use of hydrogen fuel in drive systems of rail vehicles. *Rail Vehicles/Pojazdy Szynowe*. 2022, **1**, 10-19. https://doi.org/10.53502/RAIL-147725

[20] Ritter M. Hydrogen as the key for emission-free rail transport – opportunities and challenges. Alstom. 15.07.2017. https://www.fch.europa.eu

[21] Sarma U., Ganguly S. Modelling and cost-benefit analysis of PEM fuel-cell-battery hybrid energy system for locomotive application. *2018 Technologies for Smart-City Energy Security and Power* (ICSESP). 2018. https://doi.org/10.1109/icsesp.2018.8376691

[22] Siemens. Mireo. https://www.siemens.com/mireo

[23] Wachsman E.D., Lee K.T. Lowering the temperature of solid oxide fuel cells. *Science*. 2011, **334**(6058), 935-939. https://doi.org/10.1126/science.1204090

Article citation info:
Matusiak K., Goliwąs D., Kaluba M. Adsorption dryer for use in railways. *Rail Vehicles/Pojazdy Szynowe*. 2022, 1-2, 77-85. https://doi.org/10.53502/RAIL-152486

Rail Vehicles/Pojazdy Szynowe

www.railvehicles.eu

Adsorption dryer for use in railways

Kacper **Matusiak** *, Damian **Goliwąs**, Marian **Kaluba**

Łukasiewicz Research Network – Poznan Institute of Technology, Poznan, Poland

ARTICLE INFO

Received: 28 April 2022
Revised: 27 July 2022
Accepted: 28 July 2022
Available online: 31 July 2022

KEYWORDS

adsorption dryer
compressed air dryer
railway pneumatic brake system
brake system

Pneumatic brake, which use compressed air as a working medium, is the main brake of rail vehicles. The equipment used in the braking system requires sufficiently clean, without water vapour medium to work properly. Removing water vapour from the air prevents condensation and ice formation during winter, which guarantees correct brake operation. For this purpose, adsorption dryers are used in the railways to ensure the required pressure dew point value. This article includes an overview of available compressed air drying methods, the results of calculations and bench test of the dryer prototype developed at the Institute. Assumptions and requirements for the device intended for use in railways are based on European standards and UIC cards.

1. Introduction

Due to the railway industry development and increase speed of the railway vehicles, the safety requirements are more stringent for them. Bearing this in mind, it is quite obvious that the overall objectives must be searching new solutions and achieving better parameters.

Compressed air is working medium necessary for the proper working of railway vehicle. Unit of compressed air generation and treatment supplies systems such as: pneumatic brake, self-levelling air suspension, toilet, pantograph lifting, door opener, sandboxes, sirens. The role of the pneumatic brake is of utmost importance. The brake system is one of the critical components in ensuring the safety and reliability of the railway vehicle.

The right compressed air purity is key to safe, economic and reliable pneumatic system. It is also required to provide the right amount of compressed air, considering changing work environment.

Three primary contaminant types as prevalent in a compressed air system can be identified: particles, water (liquid and vapour), oil. Removal of water contamination is singularly important for proper operation of the vehicle. Insufficiently dried compressed air can shorten the useful life of a vehicle. In order to ensure appropriate purity class for compressed air, water should be removed from the working medium immediately after the compressor. Compressed air dryers, filters, separators and cyclone separators are used to separate water from the compressed air [6].

2. Literature review

Adsorption dryers are subject of the contemporary studies and are being still intensively improved.

In 1979, Litchfield et al. [10] developed an analytical model for freeze dryer that included both sublimation and adsorption. Moreover, numerical experiments were carried out by the authors and the results were compared with the experimental data. Compressed air systems with adsorption dryers used in rail vehicles were described by Schaumann and Stanley [18] in 2008. In this article the results from experimental researches were published. In 2008, Djaeni et al. [5] presented the results of numerical calculations of multistage adsorption dryer. The authors considered the profiles of water and vapour in the dryer and also its thermal efficiency. An automatic regenerative adsorption aerosol dryer was presented by Tuch et al. [21] in 2009. The authors conducted experiments to optimize the efficiency of particle transmission. This adsorption dryer has found its application in monitoring networks

* Corresponding author: matusiak.kpr@gmail.com (K. Matusiak)

where the aerosol is dried below 50% r.H. Drying methods in railway were considered by Ripol-Saragosi [15] in 2010. The author presented the most reliable way of drying compressed air. In 2000, Mobley published a 12-chapter book [11] in which author considered the basics and problems of hydraulics and pneumatics. Chapter 15 of this book is devoted to air dryers. In 2011, Atuonwu et al. [2] developed a methodology for designing an energy-efficient adsorption dryer. The author compared a conventional dryer with an adsorption dryer designed in accordance with the developed methodology. It turned out that the energy consumption of the adsorption dryer decreased by 55%. In 2011, these authors [3] presented a procedure for optimizing a low-temperature adsorption dryer. Research on saving energy from the adsorption dryer was conducted by Kang et al. [7] in 2016. The authors considered an adsorption dryer, which was used in a process of air purification in a one company' room production. Based on experimental data, researchers searched for the optimal operating conditions for the adsorption dryer. In 2019, Ripo-Saragosi et al. [16] considered the main problem of compressed air systems- water freezing. The authors focused on the potential dangers of frozen water in railway air braking systems. In this article intelligent adsorption dryer was proposed in the aim to solve the problem of water freezing. In the same year Zhang et al. [23] presented the technology of automatic identification of a regenerative adsorption dryer. The technology proposed by authors analyzes the time curve of regeneration process, thanks to which the detection of the problem is very fast. Numerical studies of the drying and regeneration process of the air dryer adsorbent were made by Kozlov et al. [9] in 2020. The author conducted research on an exemplary scheme of an air dryer with separate processes of drying and adsorption. The results showed that such an air dryer provides a stable dew point. A double tower dryer for application in railway, pneumatic braking systems were considered by Xu et al. [4] in 2021. The authors presented the designed dryer and emphasized that its use in rail vehicles most effectively removes moisture from compressed air. In 2022, Sureshkannan et al. [19] developed a design procedure of adsorption dryer with a heatless regeneration mode. The proposed dryers can be used in applications requiring a dew point from –40 to –70°C and in which air pressure ranges from 5 bar, and inlet pressure temperature from 25 to 45°C.

3. Solutions overview

In this article the author focuses on machine designed to remove the humidity content of compressed air – compressed air dryer. There are many of compressed air dryers on the market, depending on the mechanism they use to eliminate water. Current compressed air dryer types include the following:

1. refrigeration with separation (refrigerant dryer),
2. overcompression,
3. air flows through membranes (membrane dryer),
4. adsorption (adsorption dryer),
5. absorption (absorption dryer).

Each of these dryer types will be discussed in some detail.

3.1. Refrigerant dryer

Refrigerant drying means that compressed air temperature is lowered below the dew point temperature. As a result of the cooling process, water vapour in compressed air is condensed and then separated. Water in the form of condensate is stored in reservoirs from which it is removed into the ambience. Refrigerant dryers consist of two heat exchangers: an air-to-air and an air-to-Freon.

Refrigerant dryer includes two heat exchangers. Compressed air flows through air-to-air heat exchanger, which is designed to cool the warm air coming from the compressor using of the cooled dried air. Cooling the warm air separates the condensate from vapour. Separated water is stored in reservoirs. And them compressed air flows through the air-to-Freon heat exchanger, where it is cooled again (precipitating water again). In the next stage compressed air temperature in air-to-air heat exchanger is increased using warm air from the compressor. Increasing temperature of compressed air to a room temperature prevents re-condensation of the dried working medium in the pneumatic system [1].

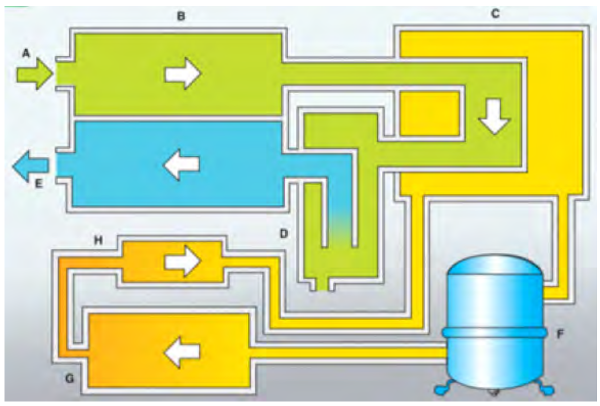

Fig. 1. Operational principle of a refrigerant dryer [1]: A – incoming compressed air, B – air/air heat exchanger, C – air/coolant heat exchanger, D – water separator E – dry compressed air, F – compressor, G – condenser, H – expansion valve

Advantages:

1. the cheapest method of removing water from compressed air,

– simple design,

– low pressure loss.
Disadvantages:
– limited dew point capability (up to 0°C),
– an increase in the ambient or compressed air temperature results in drop in performance of a device.

3.2. Overcompression

Compressed air drying using of overcompression consists in compressing working medium to a pressure higher than the operating pressure required in the pneumatic system. As a result of air compression, water vapour concentration increases. Then, after cooling the compressed air, it is saturated and condensed. In the next stage, the air expands to working pressure required for proper system operation. In this way achieving a lower pressure dew point temperature [22].

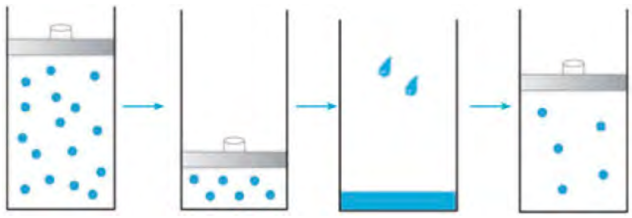

Fig. 2. Operational principle of an overcompression [22]

Advantages:
– the simplest method of drying compressed air.
Disadvantages:
– low efficiency,
– low flow rate,
– expensive method.

3.3. Membrane dryer

In the membrane dryer, the process of drying the compressed air is handled by a membrane cartridge. Cartridge consists of thousands of polymer tubes. Membranes ensure proper water vapour permeability, as a result of which water from the compressed air stays at the inside of the tubes.

In a membrane dryer wet air flows through the middle of the dryer case, in which there is membrane cartridge. Drying is caused by the counter flow of wet compressed air and regenerative air (10–15% of all dried compressed air). The regeneration air is expanded to the atmospheric pressure, which reduces its humidity. During the drying process, water vapour molecules pass through the walls and then are condensed on the outer surface with the fiber. Due to the humidity difference between dry compressed air and the regeneration air, the condensed water diffuses into the regeneration air. The dried air of the required quality feeds the pneumatic system and a small amount of it is directed to the membrane insert as regeneration air [1, 6].

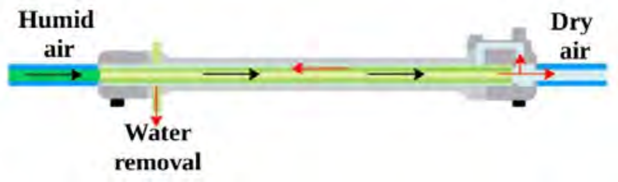

Fig. 3. Operational principle of a membrane dryer [1]

Advantages:
– dew point temperature up to –40°C,
– requires no external power source,
– simple design and high reliability,
– resistance to high and continuous pressure.
Disadvantages:
– low efficiency,
– loss of efficiency due to the consumption of 10–15% of the regeneration air,
– low resistance to sudden changes in pressure,
– highly sensitive to oils and aerosols.

3.4. Absorption dryer

Absorption drying is a chemical method of separating water from compressed air. Water is removed by passing air through a reservoir filled with absorbent and as a result the water vapour is bound with the desiccant. The most commonly used substances responsible for the process of binding water from compressed air are sodium chloride and sulfuric acid.

Compressed air is supplied to the reservoir filled with absorbent, in which the process of chemical binding of water molecules with the absorbent takes place. After flowing through absorbent, the dried air rises to the top of the reservoir and then flows through the outlet to further devices of the pneumatic system. The water-saturated absorbent is regenerated. In the second reservoir, absorbent is heated, so that the water contained in it is evaporated and flows into the atmosphere. The regenerated, unsaturated absorbent is directed back to the drying reservoir [1].
Advantages:
– constant efficiency regardless of the temperature,
– simple operation and design.
Disadvantages:
– low efficiency,
– high value of a pressure dew point of the dried air,
– require frequent replacement of the adsorbent material.

3.5. Adsorption dryer

Adsorption drying involves the removal of water from the compressed air on the surface of the desiccant material – the adsorbent. Adsorption can be divided into physical adsorption and chemical adsorption. Chemical adsorption is related to ionic or covalent bonds, while physical adsorption is related to the forces of intermolecular attraction. Physical adsorption (in which moisture migrating to the driest medium possible) is used in adsorption dryers. The adsorbent is highly porous material with a large specific surface area. A significant specific surface allows water vapour to accumulate on its surface.

The adsorption dryer has two columns filled with the adsorbent, which operate alternately: drying and regenerating. Depending on the work cycle to one of the columns is incoming compressed air. The second column regenerated adsorbent at the same time. In the drying column, the adsorbent collects the humidity contained in the flowing compressed air. Dried and purified compressed air leaves the dryer column. Part of the dried compressed air is directed to the regeneration column. In the regeneration column dried air is decompressed, so that the medium absorbs the water contained in the adsorbent. After flowing through the regeneration column, the wet air is directed to the atmosphere. A cyclic process change is implemented after adsorbent saturation in the drying column and adsorbent regeneration in the regeneration column [1, 6].

Depending on the adsorbent regeneration method, there are four different types of adsorption dryers:
- cold-regenerated adsorption dryers,
- heat regenerated adsorption dryers,
- blower regenerated dryers,
- heat of compression dryers.

Advantages:
- very low pressure dew point,
- slight pressure drops,
- no thermal influence on the environment,
- reliability.

Disadvantages:
- unstable dew point value,
- require regular adsorbent replacement,
- drop in efficiency due to the intake of regenerative air,
- sensitivity of the adsorbent to contamination from oil aerosols.

4. Requirements

Adsorption dryers are mainly used in traction vehicles because of very low pressure dew point achieved and the low pressure drops. Currently, membrane dryers are also increasingly used, mainly due to their small size and the lack of an external energy source. The dryer used in traction vehicles should meet the following requirements [8, 12–14, 20]:
- in accordance with ISO 8573-1 the dew point should be lower than –40°C,
- in accordance with UIC 612-2, the operating pressure should be between 8 and 10 bar,
- correct operation with variable humidity level (0–100%),
- correct operation with temperature ranging from –25°C to +45°C – for the T3 zone,
- high dust and dirt resistant in the working environment,
- significant vibrations resistance,
- proper maintenance susceptibility,
- protection against water freezing in the dryer.

5. Construction of adsorption dryer

The prototype of the adsorption dryer made by the Rail Vehicles Institute "TABOR" consists of three basic elements: inlet control valve covers (item 1), outlet covers (item 2) and columns (item 3). It is a cold-regenerated compressed air adsorption dryer.

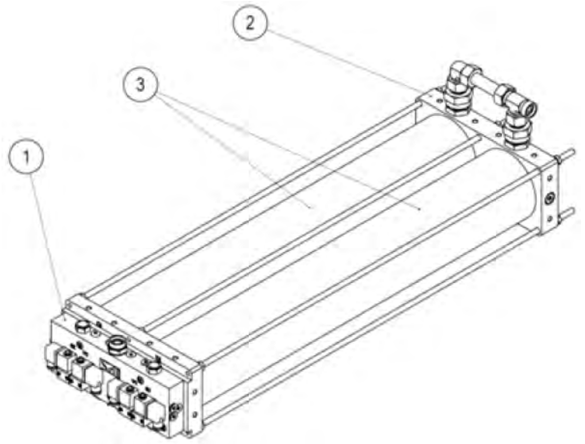

Fig. 4. Construction of the adsorption dryer

The purpose of the inlet control valve cover assembly (item 1) is to direct and control the flow of compressed air through the valves. Depending on the drying cycle of the dryer, the stream is distributed to the appropriate columns for the drying or regeneration task. The purpose of the outlet cover assembly (item 2) is to direct a portion of the dried compressed air (approx. 10–15%) into the regeneration column and exhaust the remaining dried compressed air to other devices of the pneumatic system. Columns (item 3) are filled with adsorbent. Depending on the cycle carried out, in the drying column, the air flowing through the drying material is dried, while in the regeneration column, water condensed on the surface of the adsorbent is removed. The dryer has heating elements which protect against water freezing in plate ducts.

The adsorbent selected for the dryer is a nanoporous molecular sieve which belongs to the group of aluminosilicate materials (zeolites). The high adsorption capacity of the desiccant material allows it to achieve a pressure dew point down to –80°C. The advantage of zeolites is a wide range of application temperatures, high abrasion resistance and low air flow resistance.

6. Working principle

The pre-dried air reaches the valve assembly of the inlet control plates, which, depending on the current cycle of operation, directs the medium to the appropriate column. The desiccant collects the water contained in the compressed air flowing through the column. Then the dried air leaves the drying column. The non-return valves built in the set of outlet covers ensure the flow of dry air to the outlet and prevent the flow of regeneration air to further elements of the pneumatic system. The dryer prototype designed by the Railway Vehicle Institute "TABOR" uses pre-dried compressed air (approx. 10–15%) in the regeneration process. The regeneration air expands in the regeneration column, increasing its ability to accumulate water vapour. Then, as it rapidly flows through the adsorption bed, it binds water and push it into the atmosphere. At the end of work cycle, each column switches tasks.

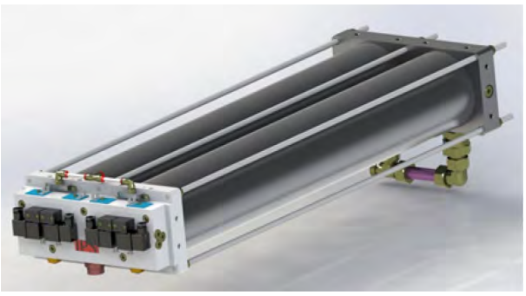

Fig. 5. Adsorption dryer IPS "TABOR"

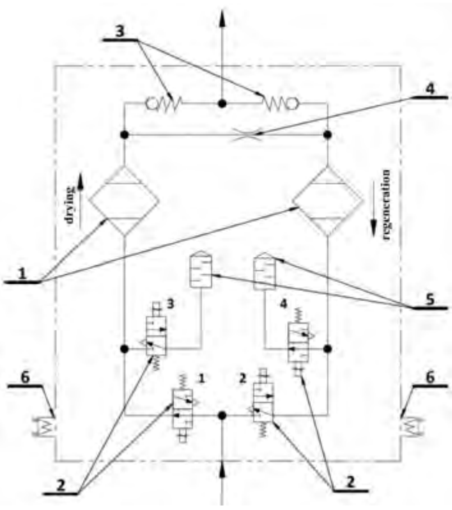

Fig. 6. Pneumatic diagram of the developed adsorption dryer: 1 – dryer column, 2 – electro-pneumatic valve, 3 – non-return valve, 4 – nozzle, 5 – noise damper, 6 – heating element

7. Methodology of calculations

To determine the required adsorption capacity of the dryer, it is necessary to calculate the mass flow rate of water vapor remaining in the compressed air after pre-drying in the cooler. For this purpose, a calculation methodology is proposed to check ensure this requirement.

In subsection 7.2 “Assessment of the required adsorption capacity” calculations were carried out according to methodology.

Properties of atmospheric air

Before proceeding with calculations, it is necessary to determine the conditions in which the adsorption capacity of the dryer will be tested. For this purpose, it is necessary to determine the values of the following parameters:

- atmospheric air pressure p_1 expressed in hPa,
- atmospheric air temperature T_1 expressed in °C,
- relative atmospheric air humidity φ_1 expressed in %,
- compressor capacity $\dot{V}_s$ expressed in $\frac{m^3}{h}$.

Based on the Enthalpy–entropy chart (Mollier diagram) and the values of the parameters of atmospheric air pressure p_1, atmospheric air temperature T_1, relative atmospheric air humidity φ_1 should be determined:

- humidity content in atmospheric air x_1 expressed in $\frac{g}{kg}$,
- atmospheric air density ρ_1 expressed in $\frac{kg}{m^3}$.

The next stage is to calculate the mass flow rate of atmospheric air intake by a compressor $\dot{m}_p$ expressed in $\frac{kg}{h}$, which is calculated as follows:

$$\dot{m}_p = \dot{V}_s \cdot \rho_1 \tag{1}$$

where $\dot{V}_s$ is compressor capacity and ρ_1 is atmospheric air density.

The next stage is to determine the amount of water vapor in the intake atmospheric air. For this purpose, it is necessary to calculate the mass flow rate of water vapor in the intake atmospheric air $\dot{m}_{H_2O(p)}$ expressed in $\frac{kg}{h}$:

$$\dot{m}_{H_2O(p)} = x_1 \cdot \dot{m}_p \tag{2}$$

where x_1 is humidity content in atmospheric air and $\dot{m}_p$ is mass flow rate of atmospheric air intake by a compressor.

Properties of the compressed air after the cooler

Next, it is necessary to determine the values of the properties of the humid compressed air after the cooler (directly behind the dryer). For this purpose, it is necessary to determine:

– compressed air pressure p_2 expressed in hPa,
– compressed air temperature T_2 expressed in °C,
– relative compressed air humidity φ_2 expressed in %,

Based on the Enthalpy–entropy chart (Mollier diagram) and the values of the parameters of compressed air pressure p_2, compressed air temperature T_2, relative compressed air humidity φ_2 should be determined:

– humidity content in compressed air x_2 expressed in $\frac{g}{kg}$.

Water vapor in compressed humid air

Compression of air by the compressor raises the temperature of the compressed air and lowers the relative humidity of the air. In the cooler, the temperature of the compressed air is lowered and condensate is condensed.

In the first step, determine the amount of condensed water behind the cooler. Determine the difference Δx of the humidity content in atmospheric air x_1 and humidity content in compressed air x_2 expressed in $\frac{g}{kg}$:

$$\Delta x = x_1 - x_2 \tag{3}$$

Then calculate the mass flow rate of condensed water behind the cooler $m_{H_2O(1)}$ expressed in $\frac{kg}{h}$:

$$\dot{m}_{H_2O(1)} = \Delta x \cdot \dot{m}_p \tag{4}$$

where Δx is difference of the humidity content in atmospheric air x_1 and humidity content in compressed air x_2 and $\dot{m}_p$ is mass flow rate of atmospheric air intake by a compressor.

Water vapor remaining in compressed humid air $\dot{m}_{H_2O(p1)}$ is calculated as the difference mass flow rate of water vapor in the intake atmospheric air $\dot{m}_{H_2O(p)}$ and mass flow rate of condensed water behind the cooler $m_{H_2O(1)}$:

$$\dot{m}_{H_2O(p1)} = \dot{m}_{H_2O(p)} - \dot{m}_{H_2O(1)} \tag{5}$$

Maximum adsorption capacity of the dryer

The adsorption capacity of an adsorbent depends on the properties of the adsorbent and the capacity of the vessel in which it is placed. To calculate the adsorption capacity, the following data are required:

– capacity of the vessel filled with the adsorbent V_0 expressed in m^3,
– adsorbent density ρ_a expressed in $\frac{kg}{m^3}$,
– adsorbent capacity $V_{H_2O(k)}$ expressed in $\frac{kg\,H_2O}{100\,kg\,adsorbent}$.

The mass of the adsorbent in vessel is calculated as follows:

$$m_{H_2O(k)} = V_0 \cdot \rho_a \cdot V_{H_2O(k)} \tag{6}$$

A single drying cycle takes about 4 min. The maximum adsorption capacity of the dryer $\dot{m}_{H_2O(k)}$ can be calculated. It is determined by mass flow rate and expressed in $\frac{kg}{h}$:

$$\dot{m}_{H_2O(k)} = \frac{m_{H_2O(k)}}{4\ min} \tag{7}$$

where $m_{H_2O(k)}$ is mass of the adsorbent in vessel.

Required adsorption capacity of the dryer

In the order to check whether the purity of the compressed air is sufficient, the condition according to which the value of the maximum adsorption capacity of the dryer $\dot{m}_{H_2O(k)}$ is greater than the value of the condensed mass flow water vapor remaining in compressed humid air $m_{H_2O(p1)}$ must be met:

$$\dot{m}_{H_2O(k)} > \dot{m}_{H_2O(p1)} \tag{8}$$

Fulfillment of the above condition indicates correct operation of the dryer.

8. Research and simulations

Tests and calculations were carried out to verify the correctness of the structure of prototype.

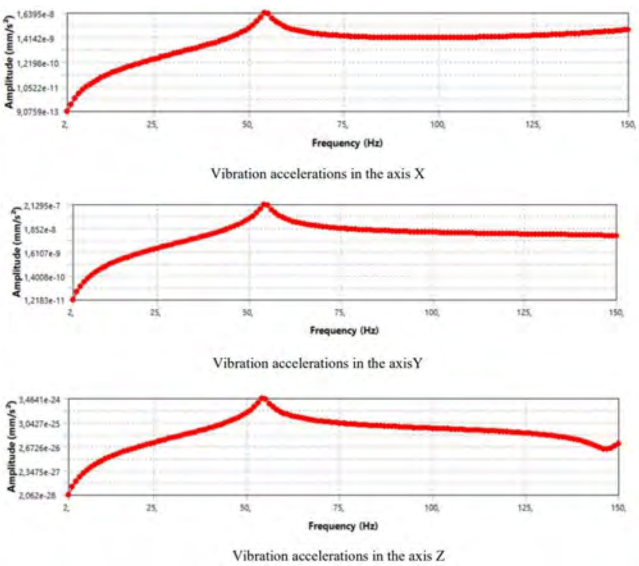

Fig. 7. Vibration accelerations in the axis X, Y, Z

A numerical strength test was carried out – modal analysis of free vibrations of the external rod. Finite element method was used to perform a modal analysis. The test concerned the flaccid external rod connecting the upper plate with the lower plate. This the most exposed element to the negative effects of vibrations. Failure to meet the requirements for resistance to vibrations may cause unwanted noise and resonance, which in turn may lead to damage to the dryer components.

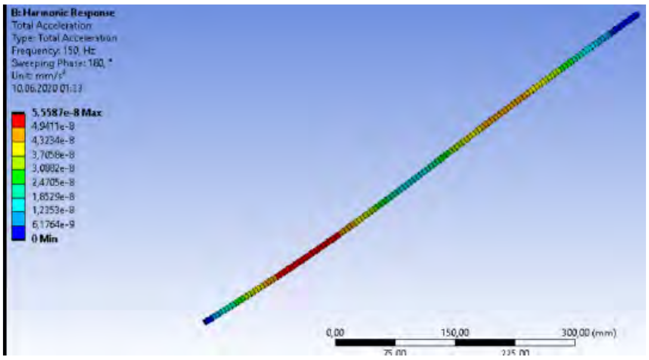

Fig. 8. Modal analysis for 150 Hz

The obtained results meet the requirements of the PN-EN 61373 standard [14]. Modal analysis results indicate a high durability of the device [17].

As part of the prototype, tests were carried out on the adsorbent. The basic quantities necessary for the correct operation of the device were checked:

- selection of dryer operating parameters,
- assessment of adsorption capacity,
- pressure dew point test.

8.1. Selecting key algorithm parameters

The parameters of the dryer operation algorithm were selected based on the determination of the times of individual dryer cycles. These parameters ensure proper drying of the compressed air in the drying column and regeneration of the adsorbent in the regeneration column. The test allowed to determine the operation time of a single drying cycle, the adsorbent drying time and the adsorbent regeneration time.

8.2. Assessment of the required adsorption capacity

In order to determine whether the dryer properly removes water from compressed air, it should be checked whether the adsorption capacity of the dryer is higher than the amount of water vapour remaining in the pre-dried air. Using the Mollier graphs (H-X), the properties of air saturated with water vapour intake by a compressor were determined:

- pressure: $p_1 = 1013.25$ kPa,
- temperature: $T_1 = 30°C$,
- relative air humidity: $\varphi_1 = 100\%$,
- air density: $\rho_1 = 1.15\,\frac{kg}{m^3}$,
- humidity content in air: $x_1 = 27.1\,\frac{g}{kg}$.

Based on the above data and the assumed compressor capacity of $\dot{V}_s = 62\,\frac{m^3}{h}$, the air mass flow was calculated:

$$\dot{m}_p = \dot{V}_s \cdot \rho_1 = 62\,\frac{m^3}{h} \cdot 1.15\,\frac{kg}{m^3} = 71.3\,\frac{kg}{h} \tag{9}$$

The water vapour mass flow contained in the intake air was calculated:

$$\dot{m}_{H_2O(p)} = x_1 \cdot \dot{m}_p = 27.1\,\frac{g}{kg} \cdot 71.3\,\frac{kg}{h} = 1.932\,\frac{kg}{h} \tag{10}$$

In the next stage, the content of water vapour in the compressed air was determined. For this purpose, the properties of compressed air saturated with water vapour were determined:

- pressure: $p_2 = 9$ bar $= 9000$ kPa,
- temperature: $T_2 = 50°$ C,
- relative air humidity: $\varphi_2 = 100\%$,
- air density: $\rho_2 = 9.65\,\frac{kg}{m^3}$,
- humidity content in air: $x_2 = 8.6\,\frac{g}{kg}$.

Then, the difference in the humidity content of air intake from the atmosphere and compressed air was determined:

$$\Delta x = x_1 - x_2 = 27.1\,\frac{g}{kg} - 8.6\,\frac{g}{kg} = 18.5\,\frac{g}{kg} \tag{11}$$

Based on the different values for the humidity content of air intake from the atmosphere, compressed air and the calculated mass flow of the intake air, the amount of condensed water behind the cooler was determined:

$$\dot{m}_{H_2O(1)} = \Delta x \cdot \dot{m}_p = 18.5\,\frac{g}{kg} \cdot 71.3\,\frac{kg}{h} = 1.326\,\frac{kg}{h} \tag{12}$$

The residual water vapour content in the compressed humid air was calculated:

$$\dot{M}_{H_2O(p1)} = \dot{m}_{H_2O(p)} - \dot{m}_{H_2O(1)} = 1.932\,\frac{kg}{h} - 1.326\,\frac{kg}{h} = 0.606\,\frac{kg}{h} \tag{13}$$

The adsorption capacity of the dryer was then determined. It should be higher than the calculated amount of water vapour that is remained in the compressed humid air. The calculations were performed for the following data:

- inner diameter of the dryer column: $d_k = 116$ mm,
- height of the dryer column: $h_k = 519$ mm,
- adsorbent density: $\rho_a = 800\,\frac{kg}{m^3}$,
- adsorbent capacity: $V_{H_2O(k)} = 19.5\,\frac{kg\ H_2O}{100\ kg\ adsorbent}$.

Capacity of single dryer column:

$$V_0 = \pi \cdot \left(\frac{d_k}{2}\right)^2 \cdot h_k = \pi \cdot \left(\frac{116\ mm}{2}\right)^2 \cdot 519\ mm = 0.00548\ m^3 \tag{14}$$

Adsorption capacity of the adsorbent contained in the column

$$M_{H_2O(k)} = V_0 \cdot \rho_a \cdot V_{H_2O(k)} = 0.00548\ m^3 \cdot 800\ \frac{kg}{m^3} \cdot \frac{19.5\ kg}{100\ kg} = 0.854\ kg \quad (15)$$

A single drying cycle takes about 4 min, so the vapour adsorption capacity of the new dryer is:

$$M_{\dot{H_2O}(k)} = \frac{m_{H_2O(k)}}{4\ min} = \frac{0{,}854\ kg}{4\ min} = 12.78\ h > m_{\dot{H_2O}(p1)} = = 0.606\ \frac{kg}{h} \quad (16)$$

The water vapour adsorption capacity of the adsorbent is sufficient for the proper operation of the device. During compression in the compressor small amounts of oil enters the dryer column. This clogs the pores of the molecular sieve and reduces the adsorption capacity of the adsorbent. A much higher value of the adsorption capacity ensures reliable operation of the device and the maintenance of correct operating parameters over a long period of time (1–2 years of operation).

8.3. Pressure dew point test

The pressure dew point test consists in measuring the pressure dew point temperature of the dried air coming out from dryer. The measurement is made with a specialized device.

In railway practice, the pressure dew point temperature should be at least 30°C lower than the ambient temperature. The test lasted 5 minutes and was carried out for the new dryer and regularly during its operation. Measurements for the described dryer were carried out using a portable CS INSTRUMENTS DP 510 meter. The tests showed that the new dryer achieves a pressure dew point of –70°C, while during operation the observed dew point is from –60°C to –40°C. These values meet the requirements of ISO 8573-1. The achieved dew point value guarantees high-purity compressed air and ensures proper operation of the dryer, even when part of the adsorbent bed is worn.

9. Summary

In traction vehicles, compressed air is essential medium for proper operation. Ensuring proper purity, and in particular removing contaminants such as humidity and water, is essential for correct vehicle operation.

In the dryer market there are many designs with different drying methods. Adsorption dryers and membrane dryers are used in traction vehicles.

The adsorption dryer prototype designed by the Railway Vehicles Institute "TABOR" meets the requirements of railroad standards, UIC cards, as well as requirements for installation and serviceability.

The prototype was subjected to bench tests and calculations. Tests showed that the device was properly designed and meets the requirements. Modal analysis of the normal mode of the outer bar proved that the values of vibration acceleration are lower than the values allowed by the standard.

Selection of the dryer operating parameters made it possible to determine the working cycle times of the dryer. The determined working cycle times allow for proper drying of compressed air and regeneration of adsorbent. The evaluation of the required adsorption capacity proved that the amount of adsorbent in the column is sufficient for proper operation of the device for at least one year. The conclusion of the pressure dew point test is that the pressure dew point value increases during operation.

The adsorption capacity of the desiccant decreases during operation because the pores of the adsorbent are clogged with oil and dust from the abraded adsorbent.

In the future, the dryer designed by the Institute of Railway Vehicles "TABOR" can be modified or new elements can be added. Further work should be oriented towards:

– adding a device for measuring the humidity of dried compressed air,
– looking for a new adsorbent.

Bibliography

[1] Atlas Copco. Compressed air manual. Atlas Copco, Wilrijk, 9, 2019.

[2] Atuonwu C., van Straten G., van Deventer H.C. et al. Improving adsorption dryer energy efficiency by simultaneous optimization and heat integration. *Drying Technology*. 2011, 29, 1459-1471. https://doi.org/10.1080/07373937.2011.591516

[3] Atuonwu C., van Straten G., van Deventer H.C. et al. Model-based energy efficiency optimization of a low-temperature adsorption dryer. *Chemical Engineering Technology*. 2011, 34(10), 1723-1732. https://doi.org/10.1002/ceat.201100145

[4] Xu B., Zhang X., Zhang S. et al. Research on double tower dryer based on air brake system of rail vehicle. *Journal of Physics: Conference Series*. 2021, 1948, 012126. https://doi.org/10.1088/1742-6596/1948/1/012126

[5] Dajeni M., Bartels P.V., Sanders J.P.M. et al. Computational fluid dynamics for multistage adsorption dryer design. *Drying Technology*. 2008, 26(4), 487-502. https://doi.org/10.1080/07373930801929532

[6] Goliwąs D. Uzdatnianie sprężonego powietrza w pojazdach trakcyjnych. *Pojazdy Szynowe*. 2007, 4, 31-43. https://doi.org/10.53502/RAIL-139837

[7] Kang S.-W., Chang S.-H., Kim H.-J. et al. A study on operating method to save energy from the adsorption dryer in the process of purifying compressed air. *Journal of Society of Korea Industrial and Systems Engineering*. 2016, 39(3), 180-191. https://doi.org/10.11627/jkise.2016.39.3.180

[8] Code UIC 612-2. Specific sub-system requirements (traction, braking, etc.) for EMU/DMU, locomotives and driving coaches (Rolling stock sub-system requirements, requirements for economic purposes, requirements for railway standardisation), 2009.

[9] Kozlov V., Piskun E., Ilicheva O. Investigation of the processes of adsorbent regeneration by compression heat in an adsorption dryer of compressed air. *Matec Web of Conferences*. 2020, 324, 02009. https://doi.org/10.1051/matecconf/202032402009

[10] Litchfield R.J., Liapis A.I. An adsorption-sublimation model for a freeze dryer. *Chemical Engineering Science*. 1979, 34(9), 1085-1090. https://doi.org/10.1016/0009-2509(79)85013-7

[11] Mobley R.K. Fluid Power Dynamics. *Newnes* 2000.

[12] Polski Komitet Normalizacyjny PN-EN 50125-1 Kolejnictwo – Warunki środowiskowe stawiane urządzeniom – Część 1: Tabor i wyposażenie pokładowe. 2014.

[13] Polski Komitet Normalizacyjny PN-EN 60721-3-5 Klasyfikacja warunków środowiskowych Część 3-2: Klasyfikacja grup czynników środowiskowych i ich ostrości. Transport i przeładunek. 2018.

[14] Polski Komitet Normalizacyjny PN-EN 61373 Zastosowania kolejowe. Wyposażenie taboru kolejowego. Badania odporności na udary mechaniczne i wibracje. 2011.

[15] Ripol-Saragosi L. Compressed air mechanical drying for railway branch of Europe. *Transport Problems*. 2010, 5(4), .

[16] Ripol-Saragosi T., Ripol-Saragosi L. Compressed air drying process energy consumption decrease by intellectual management systems implement. *International Multi-Conference on Industrial Engineering and Modern Technologies*. 2019, 1-6. https://doi.org/10.20858/tp.2018.13.4.2

[17] Rusinski E., Czmochowski J., Smolnicki T. Zaawansowana metoda elementów skończonych w konstrukcjach nośnych. *Oficyna Wydawnicza Politechniki Wrocławskiej.* Wrocław 2000.

[18] Schaumann S.P. Air compressor systems for passenger rail applications. *International Compressor Engineering Conference*. 2008, 1918, 1-9. https://docs.lib.purdue.edu/icec/1918

[19] Sureshkannan V., Vijayan S., Lenin V.R. Design and performance analysis of compressed air adsorption dryer with heatless regeneration mode. *Heat and Mass Transfer*. 2022, 58, 631-641. https://doi.org/10.1007/s00231-021-03136-4

[20] Techniczna specyfikacja interoperacyjności odnosząca się do podsystemu „Tabor — lokomotywy i tabor pasażerski” systemu kolei w Unii Europejskiej nr 1302/2014. 2014.

[21] Tuch T.M., Haudek A., Muller T. et al. Design and performance of an automatic regenerating adsorption aerosol dryer for continuous operation at monitoring sites. *Atmospheric Measurement Techniques*, 2009, 2, 417-422. https://doi.org/10.5194/amt-2-417-2009

[22] White paper. Compressed air drying. Atlas Copco. Belgium 2016.

[23] Zhang Y., Zhang Q.M., Wang R. et al. Safety analysis and fault automatic recognition technology of regenerative adsorption dryer. *IOP Conference Series: Earth and Environmental Science*. 2019, 237(3), 032058. https://doi.org/10.1088/1755-1315/237/3/032058

Article citation info:
Warzyński T., Sieczkarek K., Maćkowiak A. et al. Propaedeutic of the methodology of improving electromagnetic compatibility of railway traffic control systems in relation to the implementation of the EMC4CCS – BRIK project. *Rail Vehicles/Pojazdy Szynowe*. 2022, 1-2, 86-89. https://doi.org/10.53502/RAIL-152937

Rail Vehicles/Pojazdy Szynowe

www.railvehicles.eu

Propaedeutic of the methodology of improving electromagnetic compatibility of railway traffic control systems in relation to the implementation of the EMC4CCS – BRIK project

Tomasz **Warzyński** [a, *], Krzysztof **Sieczkarek** [a], Adam **Maćkowiak** [a], Bartłomiej **Nagórny** [a], Radosław **Szczepański** [a], Michał **Rokossowski** [a]

[a] *Poznań Institute of Technology, Łukasiewicz Research Network, Poznan, Poland*

ARTICLE INFO

Received: 8 March 2022
Revised: 19 August 2022
Accepted: 23 August 2022
Available online: 23 August 2022

KEYWORDS

electromagnetic compatibility
distributed system
BRIK project
overall equipment effectiveness
electromagnetic compatibility

The purpose of this article is to introduce to the methodology of increasing electromagnetic compatibility in distributed system, on the example of the implementation of works in the field: "Research and improvement of electromagnetic compatibility of railway traffic control devices and rolling stock", which are the subject of the BRIK project. The methodology is defined here as a set of rules for conducting research in order to achieve an intended goal. The article proposes a procedure to improve the EMC condition of distributed systems. For monitoring the quality of the system operation in terms of electromagnetic compatibility, the implementation of the OEE indicator was suggested.

1. Introduction

The definition of the railway infrastructure as a distributed system is included in the definition of a system, understood as a set of autonomous technical components connected in such a way that the user has the impression of using a single system [1]. In extensive railway structures, this is what is intended to be preserved. An example is Centralized Traffic Control (CTC), a railroad signaling system that operates in North America, which combines train route mapping decisions that were previously carried out by local signaling operators. One of the elements influencing the achievement of such an assumption is the interoperability of the system – its ability to ensure the safe and uninterrupted movement of trains. Directive (EU) 2016/797 of the European Parliament and of the Council [3] provides guidelines and constituting essential requirements, including electromagnetic compatibility between the devices of the system, as well as the system and its operating environment. By meeting these requirements, the expected compliance can be achieved. It is a factor that causes that the risk of loss of functionality of a distributed system is at the ALARP level – *as low as reasonably practicable*. To keep them in the changing environmental conditions and quality requirements of the user and functions, technical procedures are necessary, an example of which, in the field of electromagnetic compatibility, is the project BRIK – research and development in railway infrastructure [2].

The research and organizational experience and practices applied during the implementation of the BRIK project prompted the team of authors of this article to prepare a proposal for a universal methodology for improving electromagnetic compatibility. It no longer applies to a single device – for example an axle counter, not only to an installation – for example a railroad crossing. It concerns systems that are interconnected in an interoperable structure.

Detailed results of the BRIK project are available through the entities that ordered its implementation – NCBR and PKP [2]. Their discussion is the subject of prepared separate publications.

* Corresponding author: tomasz.warzynski@pit.lukasiewicz.gov.pl (T. Warzyński)

The methodology of increasing the EMC (Electromagnetic Compatibility) level, according to which the BRIK project was implemented, described in chapter 2.1, is linear, with the result included in the last stage of the process. The proposed new methodology with a performance indicator, described in chapter 2.2, has a solution based on the principle of internal feedback.

2. Methodology

2.1. Methodology according to the BRIK project

The aim of the BRIK project was to develop technical guidelines for the creation of a working environment for railway traffic control devices that are particularly exposed to disturbances from modern rolling stock in the form of electromagnetic fields with a wide frequency spectrum. Based on the research and analyzes, technical criteria were proposed in three aspects: emission limits for disturbances generated by railway equipment, immunity levels for these devices, and methods of shielding and limiting the interactions of disturbances propagated by on-board equipment of rolling stock and track-side equipment. The results of the technical tests carried out were compared with the existing environmental conditions and the applicable normative documents. The project consisted of several stages:

1. Environmental interview and polling, in order to determine the broadest possible spectrum of problems in the operation of devices that may have a genesis in the case of incompatibility between trackside devices and rolling stock devices.
2. *In-situ* tests and laboratory tests were carried out based on the interview data in order to determine the model of disturbances from the rolling stock.
3. Analysis of the obtained test results in the context of the applicable standards listed in the mandatory regulations.
4. Testing the sensitivity of devices with the use of a designated model, susceptible to disturbances from the operating environment.
5. Specification of relevant technical guidelines having for improving the compatibility between traffic control equipment and rolling stock.

Regarding point 1 – the implementation of this stage of the process consisted in collecting data by means of questionnaires and conducting interviews combined with an on-site inspection in places of railway infrastructure where there were incidents indicating the lack of electromagnetic compatibility. The milestone of this stage is the classification of the probable cases of electromagnetic incompatibility between the rolling stock and railway traffic control devices and the selection of sites for field tests and recommending types of devices for laboratory tests.

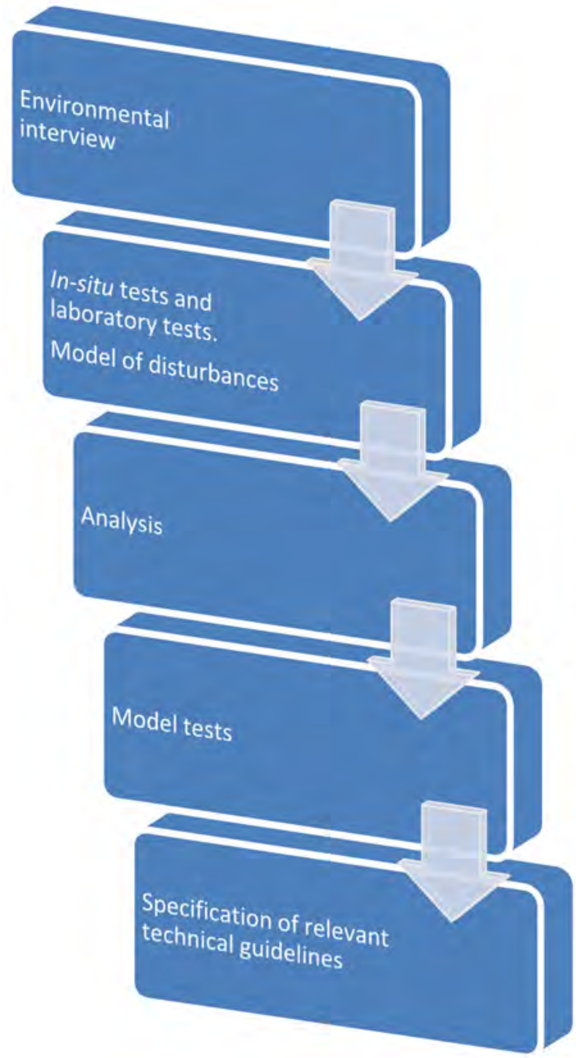

Fig. 1. The process of improving electromagnetic compatibility of distributed system according to the BRIK project

2.2. Methodology with an efficiency index

Using the methodology proven in the BRIK project – understood as a set of principles concerning the methods of improving the electromagnetic compatibility of the railway network, this article proposes a generalization that can be applied to all distributed systems. A significant change in the procedure of this method is the addition of an indicator monitoring the quality level of the system's operation that generates appropriate scenarios of operations.

The catalog of solutions used for local systems, mainly manufacturing systems, includes the Overall Equipment Effectiveness (OEE) [5] indicator, which can be implemented in the proposed solution.

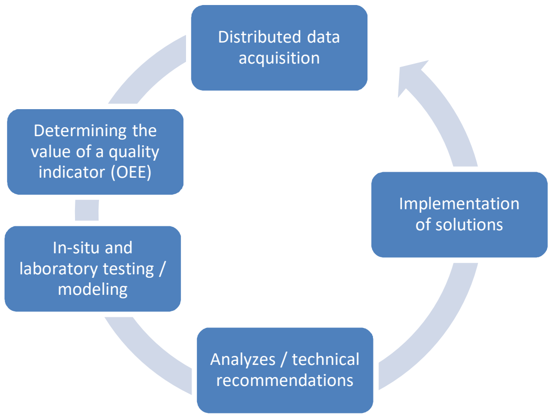

Fig. 2. General diagram of the proposed EMC improvement procedure in distributed systems

Overall Equipment Effectiveness is the gold standard for measuring productivity. OEE is the single best metric for identifying losses, benchmarking progress, and improving the quality.

By measuring OEE and base losses, you can gain important information on how to systematically improve your production process.

OEE is calculated as the product of its three constituent factors:

$$OEE\ [\%] = Availability \times Performance \times Quality$$

– Availability score of 100% means the process is always running during Planned Time. In particular, availability is degraded by failure states
– Performance takes into account Slow Cycles and Small Stops. A Performance score of 100% means when the process is running it is running as fast as possible.
– Quality takes into account defective products/ services. A Quality Score of 100% means no defects.

In order to calculate the OEE indicator, it is necessary to collect data, process it, and then prepare the results in a useful form.

These processes can be carried out using the "paper" method, the method manually supported by software, but also the Manufacturing Execution System (MES) or the OEE calculator [4, 5].

There is a tendency to replace the manual form of recording and calculating performance coefficients, including OEE, in favor of the use of specialized IT systems, thanks to which it is possible to monitor the effectiveness of processes in real time and their reporting for any period and in any context [6].

Selected categories proposed by the concept of "Six Big Losses" [7] can be used to analyze the EMC state of an interoperable system. It is consistent with the idea of determining the OEE indicator and may be the target of activities aimed at improving the quality, reliability and efficiency of distributed railway systems.

Examples of detectable and monitorable loss factors for EMC:
– Availability Loss: Setup and Adjustments, Breakdowns – e.g. downtime resulting from a failure caused by loss of immunity to SURGE, EFT or ESD disturbances;
– Performance Loss: Reduced Speed, Small Stops – e.g. operation of automatic locks in systems with axle counters under the influence of magnetic fields from rolling stock, in situations that do not require intervention;
– Quality Loss: Production Rejects, Startup Rejects – e.g. emerging interference in radio transmissions due to incorrect installation of power supply systems.

3. Conclusions

Electromagnetic compatibility not only between devices but also between installations and, as shown by the implementation of the BRIK project – in the railway infrastructure, is of great importance for the quality and functional safety of a distributed system. As shown in the article, by using real-time monitoring of the system performance index – you can get a tool to achieve higher quality of services or products. The aspect of electromagnetic compatibility, as a factor influencing the quality of organizational and technical solutions, should be taken into account by designers of distributed systems.

Nomenclature

CTC Centralized Traffic Control
EFF Electrical Fast Transients
EMC Electromagnetic Compatibility
ESD Electrostatic Discharge
OEE Overall Equipment Effectiveness
MES Manufacturing Execution System
SURGE high energy disturbance

Bibliography

[1] Tanenbaum A.S., van Steen M. Distributed Systems: Principles and Paradigms. *Prentice-Hall, Inc*. 2016. https://dl.acm.org/doi/10.5555/1202502

[2] BRIK – Badania i Rozwój w Infrastrukturze Kolejowej" – wspólne przedsięwzięcie podmiotów: Narodowe Centrum Badań i Rozwoju (NCBR), Polskie Koleje Państwowe (PKP); Program Operacyjny Inteligentny Rozwój 2014-2020; Oś priorytetowa – Zwiększenie potencjału naukowo-badawczego; Działanie – Badania naukowe i prace rozwojowe. https://archiwum.ncbr.gov.pl/fileadmin/gfx/ncbir/userfiles/_public/fundusze_europejskie/inteligentny_rozwoj/brik/4__zakres_tematyczny_brik.pdf

[3] Directive (EU) 2016/797 of the European Parliament and of the Council of 11 May 2016 on the interoperability of the rail system within the European Union. https://eur-lex.europa.eu/legal-content/EN/TXT/?uri=CELEX:32016L0797

[4] Mazurek W. Wskaźnik OEE – teoria i praktyka – wydanie II, Neuron 2014. http://www.neuron.com.pl/pliki/oee.pdf

[5] Overall Equipment Effectiveness. http://oee.com (accessed on 28.02.2022).

[6] Automatyczne wyliczanie: wskaźnik OEE – SPC – KPI. https://www.vix.com.pl/automatyczne-oee-spc-kpi (accessed on 28.02.2022).

[7] Six Big Losses. https://www.vorne.com/pdf/six-big-losses-executive-summary.pdf (accessed on 18.08.2022).

www.railvehicles.eu